

Seven new triply eclipsing triple star systems

S. A. Rappaport^{1,2}, T. Borkovits^{1,3,4,5,6}, T. Mitnyan¹, R. Gagliano⁷, N. Eisner^{8,9,*,**}, T. Jacobs¹⁰, A. Tokovinin¹¹, B. Powell¹², V. Kostov^{12,13}, M. Omohundro¹⁴, M. H. Kristiansen^{15,16}, R. Jayaraman², I. Terentev¹⁴, H.M. Schwengeler¹⁴, D. LaCourse¹⁷, Z. Garai^{5,6,18}, T. Pribulla¹⁸, P.F.L. Maxted¹⁹, I. B. Bíró^{1,3}, I. Csányi³, A. Pál⁴, and A. Vanderburg²

¹ HUN–REN–SZTE Stellar Astrophysics Research Group, H-6500 Baja, Szegedi út, Kt. 766, Hungary

² Department of Physics, Kavli Institute for Astrophysics and Space Research, M.I.T., Cambridge, MA 02139, USA
e-mail: sar@mit.edu

³ Baja Astronomical Observatory of University of Szeged, H-6500 Baja, Szegedi út, Kt. 766, Hungary.
e-mail: borko@electra.bajaobs.hu

⁴ Konkoly Observatory, Research Centre for Astronomy and Earth Sciences, H-1121 Budapest, Konkoly Thege Miklós út 15-17, Hungary

⁵ ELTE Eötvös Loránd University, Gothard Astrophysical Observatory, Szent Imre h. u. 112, 9700 Szombathely, Hungary

⁶ HUN–REN–ELTE Exoplanet Research Group, H-9700 Szombathely, Szent Imre h. u. 112, Hungary

⁷ Amateur Astronomer, Glendale, AZ 85308

⁸ Centre For Computation Astrophysics, NYC, USA

⁹ Princeton University, Princeton, USA

¹⁰ Amateur Astronomer, 12812 SE 69th Place Bellevue, WA 98006, USA

¹¹ Cerro Tololo Inter-American Observatory | NSF's NOIRLab, Casilla 603, La Serena, Chile

¹² NASA Goddard Space Flight Center, 8800 Greenbelt Road, Greenbelt, MD 20771, USA

¹³ SETI Institute, 189 Bernardo Avenue, Suite 200, Mountain View, CA 94043, USA

¹⁴ Citizen Scientist, c/o Zooniverse, Dept. of Physics, University of Oxford, Denys Wilkinson Building, Keble Road, Oxford, OX1 3RH, UK

¹⁵ Brorfelde Observatory, Observator Gyldenkeres Vej 7, DK-4340 Tølløse, Denmark

¹⁶ National Space Institute, Technical University of Denmark, Elektrovej 327, DK-2800 Lyngby, Denmark

¹⁷ Amateur Astronomer, 7507 52nd Place NE Marysville, WA 98270, USA

¹⁸ Astronomical Institute, Slovak Academy of Sciences, 05960 Tatranská Lomnica, Slovakia

¹⁹ Astrophysics Group, Keele University, Staffordshire, ST5 5BG, UK

Received January ..., 2024; accepted ... , ...

ABSTRACT

Aims. We have identified nearly a hundred close triply eclipsing hierarchical triple star systems from data taken with the space telescope TESS. These systems are noteworthy in that we can potentially determine their dynamical and astrophysical parameters with a high precision. In the present paper, we report the comprehensive study of seven new compact triply eclipsing triple star systems taken from this larger sample: TICs 133771812, 176713425, 185615681, 287756035, 321978218, 323486857, and 650024463.

Methods. Most of the data for this study come from TESS observations, but two of them have Gaia measurements of their outer orbits, and we obtained supplemental radial velocity (RV) measurements for three of the systems. The eclipse timing variation curves extracted from the TESS data, the photometric light curves, the RV points, and the spectral energy distribution (SED) are combined in a complex photodynamical analysis to yield the stellar and orbital parameters of all seven systems.

Results. Four of the systems are quite compact with outer periods in the range of 41–56 days. All of the systems are substantially flat, with mutual inclination angles of $\lesssim 2^\circ$. Including the systems reported in this work, we have now studied in considerable detail some 30 triply eclipsing triples with TESS, and are accumulating a meaningful census of these systems.

Key words. Stars: binaries (including multiple): close – (Stars:) binaries: eclipsing – (Stars:) binaries: general – Stars: fundamental parameters – Stars: individual: TICs 133771812, 176713425, 185615681, 287756035, 321978218, 323486857, 650024463

1. Introduction

Before the epoch of the *Kepler* (Borucki et al. 2010), and TESS (Ricker et al. 2015) missions there were very few well-studied compact hierarchical triple star systems. Here we define ‘compact triple’ as a triple star system with an outer period of $\lesssim 1000$ days, down to the currently shortest known outer period of 33.0 d (λ Tau; Ebbighausen & Struve 1956). Thanks to the precision space-based photometry of these missions, as well as Gaia as-

strometry and radial velocity measurements (Gaia Collaboration et al. 2016; Babusiaux et al. 2023), and the Optical Gravitational Lensing Experiment (OGLE) ground-based survey (Udalski et al. 1997), we now know of some thousand compact triple systems (see, e.g., Rappaport et al. 2013; Borkovits et al. 2015, 2016; Czavalinga et al. 2023a; Hajdu et al. 2019). Among the best studied of these are about 50 that have years-long eclipse timing variation (ETV) curves and/or third body eclipses where the tertiary star eclipses the inner binary or vice versa (Borkovits et al. 2015; Rappaport et al. 2022, 2023).

* Flatiron Research Fellow

** Henry Norris Russel Fellow

In general, the triple systems with third body eclipses end up providing the most detailed information about their respective triple systems, including a complete understanding of the stellar parameters (masses, radii, T_{eff} , and ages) as well as the orbital parameters, including the inclination angles of the two orbital planes, and the mutual inclination angle. This detailed information can often be obtained without the need for extensive radial velocity (RV) measurements. The reasons for this success stem from the fact that triply eclipsing triples tend to be quite compact, with orbital periods typically in the range of 40-300 days. In turn, the compactness of the triples can lead to interesting and important dynamical interactions, including so-called ‘dynamical’ delays, driven apsidal motion in the inner binary, possible precession of the orbital planes, as well as some new and fascinating anomalous dynamical interactions, (see, e.g., Rappaport et al. 2013; Borkovits et al. 2015; Borkovits & Mitnyan 2023).

The items that allow for robust system solutions involve the following five ingredients: (1) precision space-based photometry of the inner binary eclipses and the third-body eclipses; (2) eclipse timing variation curves (ETV) which are distinct from measuring the shapes and depths of the eclipses; (3) archival ground-based photometry that has the potential to determine the outer orbital period via the third-body eclipses; (4) archival spectral energy distributions (SED); and (5) a comprehensive complex photodynamical code which puts all this information together in a global analysis. Of course, supplemental RV data are always useful for further reducing the uncertainties and are much appreciated.

Knowing the system parameters is important in trying to understand the complex formation scenarios of triple and multiple star systems (see, e.g., Tokovinin & Moe 2020), as well as for investigating expected and unexpected dynamical interactions in the present-day systems. The latter category includes dynamical interactions on timescales intermediate between the binary and outer period (see, e.g., Appendix A1 of Rappaport et al. 2022), and between the outer period and the apse-node long term period (Pribulla et al. 2023).

In this work we report on seven new triply eclipsing triples. In Sect. 2 we discuss how these systems are found, and the basic properties of the seven systems presented in this work. Segments of the TESS light curves exhibiting third body eclipses are shown in Sect. 3 along with model fits. The folded outer orbital light curves obtained from archival ground-based data are presented in Sec. 4. In Sect. 5 we show ETV curves extracted from the TESS light curves, as well as RV curves for a few sources where we were able to acquire them. The photodynamical analysis code is described briefly in Sect. 6. The individual systems are discussed in Sect. 7. Finally, in Sect. 8 we summarize our work and draw some broader conclusions.

2. The seven triply eclipsing triples

2.1. Discovery of the triples

Most of the triply eclipsing triples reported by us over the past several years (see, e.g., Borkovits et al. 2020b, 2022a; Rappaport et al. 2022, 2023) were found by our ‘Visual Survey Group’ (VSG; Kristiansen et al. 2022). This involved visual inspection of millions of TESS light curves. The vast majority of the light curves were produced from TESS full-frame images (FFI) of anonymous stars down to TESS magnitude $T \lesssim 15$. However, most of the discovered triply eclipsing triples were actually found among a much smaller number (~1 million) of light curves of preselected eclipsing binaries (EBs). The latter were identified

in the TESS data via machine learning (ML) searches¹ (see Powell et al. 2021) of more than 100 million TESS FFI light curves from Sectors 1-48. We made our own light curves from the raw FFIs on the NASA Center for Climate Simulation (NCCS) Discover supercomputer using the *ELEANOR* (Feinstein et al. 2019) code. The search of these ML-selected binaries was therefore the more productive of the two approaches, but such searches are less likely to discover new classes of objects because we are specifically selecting binaries to look at.

The visual surveying of the light curves is done with Allan Schmitt’s *LcTools* and *LcViewer* software (Schmitt et al. 2019), which facilitates the inspection of a typical light curve in just a matter of a few seconds. Our searches for triply eclipsing triples involve looking for an eclipsing binary light curve with an additional extra eclipse that is typically strangely shaped and of longer duration than the regular EB eclipses, or a rapid succession of isolated eclipses. Once such ‘extra’ eclipses, or ‘third body’ events are found, there is usually very little doubt that they are due to a tertiary star eclipsing the EB or vice versa.

From searches through light curves obtained from the first three full years of TESS observations, we have found more than 70 of these triply eclipsing triples. Of these 70 triply eclipsing systems, we have been able to determine the outer orbital period for about half of them via a combination of TESS and archival ground-based photometry, and, occasionally, from Gaia-determined orbits. We have previously reported five of these 30 systems in Borkovits et al. (2020b), Mitnyan et al. (2020) and Borkovits et al. (2022a); six more in Rappaport et al. (2022); and an additional nine systems in Rappaport et al. (2023). Here we present a detailed analysis and study of seven of the remaining triply eclipsing triples from among this set. In particular, we have chosen those triples which are not scheduled for additional TESS observations, at least not until the end of the ongoing second extended mission. Hence, it is not surprising that six of our seven targets are located in the southern hemisphere.

2.2. Summary of available data

Fortunately, there exist excellent archival data for all of these sources, in addition to the TESS data. In particular, we made use of archival data from (1) Gaia Data Release 3 (Gaia Collaboration 2023); (2) the Mikulski Archive for Space Telescopes (MAST)², in particular the TESS Input Catalog v8.2 (Paegert et al. 2021); (3) the All-Sky Automated Survey for SuperNovae (ASAS-SN; Shappee et al. 2014; Kochanek et al. 2017); (4) Asteroid Terrestrial-impact Last Alert System (ATLAS³; Tonry et al. 2018; Smith et al. 2020); and (5) the online VizieR SED viewer (Ochsenbein et al. 2000)⁴. Last but not least, (6) for one target, TIC 321978218, we also used SuperWASP data (Pollacco et al. 2006). This relatively bright system was observed with SuperWASP cameras during five consecutive seasons between 2010 and 2014, and these observations partly cover 11 third-body eclipses, which we have included in our analysis (see below). We note that SWASP observations are also available for another target, TIC 176713425, but in this latter case, we did not find these data to be useful for our analysis and, hence, neglected them.

¹ We use a neural network binary classifier trained to find eclipses in light curves as an initial screening tool.

² <https://mast.stsci.edu/portal/Mashup/Clients/Mast/Portal.html>

³ <https://fallingstar-data.com/forcedphot/>

⁴ <http://vizier.cds.unistra.fr/vizier/sed/>

The Gaia and MAST data were used primarily to construct a table of the basic properties of the seven systems reported in this work (Table 1 with, e.g., coordinates, magnitudes, distances, proper motions, and so forth). Amongst the Gaia data we also found the outer orbits for two of our systems. We used the ASAS-SN and ATLAS data primarily to obtain an independent and accurate determination of the outer orbital period for 6 of the 7 systems via the third-body eclipses over a baseline of ~ 10 yr. The SED data were obtained from VizieR; these points were used in conjunction with other data to make some of the initial fits to the system parameters.

The sectors in which the sources were observed by TESS, and the sectors during which third-body events were actually seen, are summarized in Table 2. In Table 3 we point out the two sources whose outer orbits were found with Gaia⁵ and references to another source that had previous reports in the literature, and we list the outer orbital parameters of period, eccentricity, and argument of periastron we find from this work.

In addition to the above archival data, we were able to acquire new RV data for two of the sources with the CHIRON spectrometer mounted on the 1.5-m SMARTS telescope at CTIO in Chile (Tokovinin et al. 2013). Spectra with a resolution of 25,000 were taken in the service mode and processed by the standard pipeline (Paredes et al. 2021). We note that a set of archive RV data were also collected for a third target – TIC 185615681.

Finally, in Table 4 we summarize the information we have available for all of the seven sources. This includes eclipse timing variation (ETV) curves that exhibit non-linear behavior, RV data, and spectroscopic outer orbits from Gaia NSS catalog (in two cases).

3. Light curve and model Fits

In Figures 1–7 we show short segments of the TESS light curves that exhibit third body outer eclipses where the tertiary star eclipses the inner eclipsing binary or vice versa. The blue points are the TESS photometric measurements. For the light curve modeling we used 30-min cadence data even in those sectors where shorter cadence data were available. Hence, all these blue points are at a cadence of 30-min. The regular binary eclipses are either self-evident (or called out in the respective figure captions), while the ‘extra’ eclipses are, for the most part, all the dips in flux that cannot be ascribed to the regular EB eclipses. In some cases the third-body eclipses are quite irregular and anomalous looking, while in other cases, the eclipses look almost ‘normal’ but occur in rapid succession and/or are clearly out of place. Moreover, in the eleven panels of Fig. 8 we plot those third-body eclipses of TIC 321978218 which were observed, at least in part, during the SuperWASP survey, and were used in our analysis.

The smooth red curves are models taken from the full photodynamical analysis. These will be discussed in Sect. 6.

These third-body eclipses contain crucial information about both the orbits (in particular, the mutual inclination angle and outer orbital period) as well as the properties of the stars themselves (e.g., the relative sizes and effective temperatures).

4. Archival outer orbit folds

For each of the seven triply eclipsing triple systems, we looked up the archival ASAS-SN (Shappee et al. 2014; Kochanek et al. 2017) and ATLAS (Tonry et al. 2018; Smith et al. 2020) data sets

that were available. The goal here is to find additional third body eclipses in the archival record and thereby possibly determine the outer orbital period of these systems. In general the ASAS-SN data typically yield between 3000 and 6000 photometric points spanning the past decade (over the whole sky). The ATLAS data have only a somewhat smaller number of points than ASAS-SN in the northern hemisphere, but often $\lesssim 1000$ points in the south. The ATLAS photometry is superior for the fainter targets (e.g., $\gtrsim 15$ th magnitude).

We median normalize the V and g bands of ASAS-SN to each other, and likewise the o and c bands of ATLAS. Finally, we median normalize the ASAS-SN and ATLAS data to each other to form a data set typically consisting of between 4000 and 8000 archival points. Next, we remove the EB orbital light curve by subtracting out typically 100 harmonics of the EB period from the raw data (see, e.g., Powell et al. 2021). We then use a Box Least Squares (BLS) algorithm⁶ (Kovács et al. 2002) to do a blind search for the third-body eclipses of the outer orbit covering periods from 20-1000 days. These third body events usually occur over an interval of about a day. The outer periods in this sample of seven sources range from 41 days to a year. Therefore, the ‘duty cycle’ for the third body events ranges from ~ 0.02 to ~ 0.003 . For an archival sample of, for example, 5000 points, we can then expect somewhere between 15-100 points to land within the outer orbital phase range of the third body events, and thereby measure an average drop in flux at that phase. Thus, for systems with longer outer periods, the task of uniquely identifying the outer orbital period from the archival data becomes ever more challenging.

The results of our search for the outer orbital periods are shown in Fig. 9. For six of the seven sources (all except TIC 133771812) there is a clear BLS signal at the outer period. For TIC 133771812, with an outer period of 244 days, and third-body eclipse depths of only $\sim 6\%$, we were not able to detect the outer eclipses at a significant level. On the other hand, we were able to robustly detect the outer eclipses in TIC 287756035 with a year-long outer period. The only difficulty with that one is that due to the annual observing schedule of the ground-based observations, we cannot tell whether the outer period is 368 days or half that. However, other information that is available allows us to break this degeneracy and select the 368 day period.

We note that four of the seven triples studied in this work (TICs 185615681, 321978218, 323486857, and 650024463) exhibit both types of outer eclipses (i.e., secondary vs. primary) in the TESS data – thanks to our nearly edge-on view of their outer orbits. Additionally, in the cases of TICs 176713425 and 287756035, although TESS has observed only one type of outer eclipse, our photodynamical analyses (see later in Sect. 6) predict the existence of the other type of outer eclipse, as well. In contrast to these, only TIC 321978218 exhibits detectable third body primary and secondary eclipses in our archival folded light curves (Fig. 9).

In general, these outer eclipses we see in the archival folds are detected at the ~ 8 - 20σ confidence level. Therefore, if the secondary outer eclipses have several times less area under their normalized light curve, then they can become very difficult to detect. In fact, we do not detect the secondary eclipse in five of the six above-mentioned sources. In four of the six cases, it is obvious that the shallow secondary eclipses would be undetectable in the archival data. In the specific case of TIC 650024463, where the secondary outer eclipses have $\sim 2/3$ the depths of the primary

⁵ <https://vizier.cds.unistra.fr/viz-bin/VizieR-3?source=I/357&-out.max=50&-out.form=HTML>

⁶ <https://exoplanetarchive.ipac.caltech.edu/cgi-bin/Pgram/nph-pgram>

Table 1. Main properties of the seven triple systems from different catalogs

Parameter	133771812	176713425	185615681	287756035	321978218	323486857	650024463
RA J2000	08:05:16.560	23:35:35.42	08:41:08.26	13:14:51.86	00:04:12.35	11:45:48.28	02:41:20.17
Dec J2000	-41:49:57.97	42:22:17.57	-32:12:03.06	-46:44:29.21	-50:55:00.91	-65:02:48.99	-82:25:16.73
T^a	13.30 ± 0.01	13.75 ± 0.01	10.52 ± 0.01	12.86 ± 0.01	11.35 ± 0.01	11.61 ± 0.02	14.4 ± 0.6
G^b	13.76 ± 0.00	14.25 ± 0.00	10.65 ± 0.00	13.47 ± 0.01	11.73 ± 0.00	12.31 ± 0.00	14.85 ± 0.00
G_{BP}^b	14.12 ± 0.00	14.62 ± 0.00	10.75 ± 0.00	14.00 ± 0.01	12.00 ± 0.00	12.93 ± 0.01	15.20 ± 0.02
G_{RP}^b	13.19 ± 0.00	13.68 ± 0.00	10.46 ± 0.00	12.79 ± 0.00	11.28 ± 0.00	11.54 ± 0.01	14.17 ± 0.01
B^a	14.62 ± 0.01	15.40 ± 0.46	10.97 ± 0.16	14.77 ± 0.08	12.42 ± 0.06	13.68 ± 0.02	...
V^c	14.00 ± 0.12	14.60 ± 0.11	10.68 ± 0.03	13.75 ± 0.13	11.92 ± 0.05	12.68 ± 0.07	...
J^d	12.49 ± 0.03	13.06 ± 0.02	10.56 ± 0.03	11.92 ± 0.02	10.77 ± 0.03	10.53 ± 0.02	...
H^d	12.23 ± 0.02	12.73 ± 0.03	10.50 ± 0.02	11.35 ± 0.02	10.50 ± 0.02	9.97 ± 0.02	...
K^d	12.17 ± 0.02	12.66 ± 0.03	10.48 ± 0.02	11.28 ± 0.02	10.44 ± 0.03	9.83 ± 0.02	...
$W1^e$	12.09 ± 0.02	12.65 ± 0.02	10.16 ± 0.02	11.22 ± 0.02	10.40 ± 0.02	9.70 ± 0.02	...
$W2^e$	12.09 ± 0.02	12.67 ± 0.02	10.21 ± 0.02	11.27 ± 0.02	10.44 ± 0.02	9.75 ± 0.02	...
$W3^e$	12.08 ± 0.28	12.02 ± 0.22	10.17 ± 0.07	11.29 ± 0.11	10.41 ± 0.08	9.57 ± 0.04	...
$T_{\text{eff}} [\text{K}]^b$	5342 ± 300	5355 ± 115	8325 ± 950	4973 ± 230	6506 ± 800	4518 ± 150	4362 ± 125
$T_{\text{eff}} [\text{K}]^d$	8357 ± 123	5937 ± 125	8696 ± 155	5090 ± 122	5949 ± 130	7197 ± 130	...
Radius [R_{\odot}] ^b	3.41 ± 0.41	3.48 ± 0.11	...	5.07 ± 0.47	1.97 ± 0.50	11.28 ± 1.2	14.3 ± 0.8
Radius [R_{\odot}] ^a	2.82 ± NA	3.08 ± NA	3.11 ± 0.12	5.20 ± NA	2.35 ± 0.13	9.47 ± NA	...
Distance [pc] ^f	1803 ± 46	2144 ± 86	833 ± 13	2139 ± 83	570 ± 7	1818 ± 38	1126 ± 26
$E(B - V)^a$	0.59 ± 0.01	0.15 ± 0.01	0.13 ± 0.01	0.12 ± 0.00	0.01 ± 0.01	0.75 ± 0.02	0.09 ± 0.00
μ_{α} [mas/yr] ^b	-2.56 ± 0.01	-3.82 ± 0.01	-3.51 ± 0.01	-15.07 ± 0.02	24.38 ± 0.01	10.61 ± 0.01	-2.43 ± 0.02
μ_{δ} [mas/yr] ^b	+5.63 ± 0.01	-6.43 ± 0.01	-3.58 ± 0.02	4.73 ± 0.01	-0.83 ± 0.02	1.18 ± 0.01	-5.01 ± 0.02
RUWE ^{b,g}	0.975	1.00	1.11	1.15	1.79	0.957	1.07
astr_ex_noise [mas] ^{b,h}	0	0	0.13	0.066	0.23	0.043	0.065
astr_ex_noise_sig ^{b,h}	0	0	29	3.3	117	2.1	1.2
P_{binary}^i [d]	12.370	1.8987	2.3185	2.0814	0.5698	0.8840	7.1971
P_{triple}^j [d]	242.3	52.55	55.84	367.6	57.51	41.36	107.95

Notes. General: “NA” and ellipses in this table indicate that the value is not available. (a) TESS Input Catalog (TIC v8.2) (Paegert et al. 2021). (b) Gaia EDR3 (Gaia collaboration 2021); the uncertainty in T_{eff} and R listed here is 1.5 times the geometric mean of the upper and lower error bars cited in DR2. Magnitude uncertainties listed as 0.00 are ≤ 0.005 . (c) AAVSO Photometric All Sky Survey (APASS) DR9, (Henden et al. 2015), <http://vizier.u-strasbg.fr/viz-bin/VizieR?-source=II/336/apass9>. (d) 2MASS catalog (Skrutskie et al. 2006). (e) WISE point source catalog (Cutri et al. 2013). (f) Bailer-Jones et al. (2021), geometric distances. (g) The Gaia renormalized unit weight error (RUWE) is the square root of the normalized χ^2 of the astrometric fit to the along-scan observations. Values in excess of about unity are sometimes taken to be a sign of stellar multiplicity. (h) Abbreviations for “astrometric_excess_noise” and “astrometric_excess_noise_significance” (Lindgren et al. 2021; https://gea.esac.esa.int/archive/documentation/GDR2/Gaia_archive/chap_datamodel/sec_dm_main_tables/ssc_dm_gaia_source.html); these are a measure of “the disagreement, expressed as an angle, between the observations of a source and the best-fitting standard astrometric model.” Values of $\text{astr_ex_noise_sig} \geq 2$ are considered significant. (i) Binary and outer orbital periods from this work; given here for reference purposes.

Table 2. TESS observation sectors for the triples^a

Object	Sectors Observed	Third Body Events
TIC 133771812	S7,S8,S34,S35,S61,S62	S7,S34,S61
TIC 176713425	S16,S17,S57	S16
TIC 185615681	S8,S34,S35,S61,S62	S8,S34,S35,S61,S62
TIC 287756035	S11,S37,S38,S64	S37,S64
TIC 321978218	S2,S28,S29,S68,S69	S28,S29,S68,S69
TIC 323486857	S10,S11,S37,S38,S64,S65	S10 ^b ,S11,S37,S38 ^b ,S64 ^b ,S65
TIC 650024463	S1,S12,S13,S27,S28,S39,S66,S67,S68	S12,S27,S28,S39,S66,S67

Notes. (a) None of these sources will be observed in further TESS sectors until the end of Cycle 6 observations; (b) both primary and secondary third-body eclipses observed in these sectors.

eclipses, one might wonder whether these should have been detected in the archival fold for that source. However, when we take into account that the primary outer eclipses have a duration that is ~ 2 -3 times longer than the secondary outer eclipses, then the expected detection significance of the secondary eclipses will drop by about a factor of 3-4. This is a sufficient decrease so we cannot expect to detect it robustly—and we do not. Finally, in the case of TIC 287756035, the above mentioned seasonal gaps in the ground-based observations would explain the absence of the archival fold detection of the other type of third-body eclipse⁷.

⁷ We return to this question in Sect. 7.2.4.

5. ETV and RV curves

The eclipse timing variation curves form a crucial piece of input information for the comprehensive photodynamical analysis we discuss in Sect. 6. These are based on eclipse midtimes for both the primary and secondary eclipses of the inner EB of the system. We extract these mid-eclipse times in the manner discussed previously in Borkovits et al. (2015, 2016). The non-linear behavior we see in the ETV curves comes predominantly from three basic effects, as follows. First, there is the classical light-travel-time effect (LTTE; Roemer 1677) due to the changing distance to the EB as it is pulled around in its outer orbit

Table 3. Other detections of the triples^a

Object	This Work ^b (P_{out} , e_{out} , ω_{out})	Gaia DR3 Orbits ^{b,c} (P_{out} , e_{out} , ω_{out})	Other
TIC 133771812	243.87 d; 0.217; 195°
TIC 176713425	52.57 d; 0.412; 95.2°
TIC 185615681	55.86 d; 0.098; 309°	...	Rowan et al. (2023)
TIC 287756035	368 d; 0.235; 53.7°
TIC 321978218	57.51 d; 0.258; 123°	57.52 d; 0.28; 116°	...
TIC 323486857	41.36 d; 0.007; 241°	41.35 d; 0.045; 180°	...
TIC 650024463	107.88 d; 0.323; 351°

Notes. (a) Three of the seven triply eclipsing systems were spotted in prior broad surveys, but no quantitative analysis of the system parameters (especially of the constituent stars) was undertaken. Two of them have outer orbits reported by Gaia, but no third body eclipses were reported by Gaia. One of the systems, TIC 185615681, was included in the Rowan et al. (2023) list of multistellar systems tabulated from ASAS-SN data, and studied for the apsidal motion of its inner binary by Zasche (2012) and Kim et al. (2018), as well as for RVs by Duerbeck & Rucinski (2007). (b) Where available, we show for each source, the period, eccentricity, and argument of periastron of the outer orbit, separated by semicolons. (c) The Gaia orbital solutions are both spectroscopic; Babusiaux et al. (2023); Gaia Collaboration (2023).

Table 4. Input information for the system analysis

Object	TESS 3rd-Body Eclipse(s) ^a	TESS EB Light curve ^a	Archival Outer Eclipses ^b	SED Points ^c	ETV Curve ^d	RV Data ^e	Gaia Orbit ^f
TIC 133771812	✓	✓		✓	✓		
TIC 176713425	✓	✓	✓	✓	✓		
TIC 185615681	✓	✓	✓	✓	✓	✓	
TIC 287756035	✓	✓	✓	✓		✓	
TIC 321978218	✓	✓	✓	✓	✓	✓	✓
TIC 323486857	✓	✓	✓	✓	✓		✓
TIC 650024463	✓	✓	✓	✓	✓		

Notes. (a) See Figs. 1–7. (b) Fig. 9. (c) Obtained from <http://vizier.cds.unistra.fr/vizier/sed/>. (d) See Figs. 10–15. (e) See Figs. 16–18. (f) Babusiaux et al. (2023); Gaia Collaboration (2023)

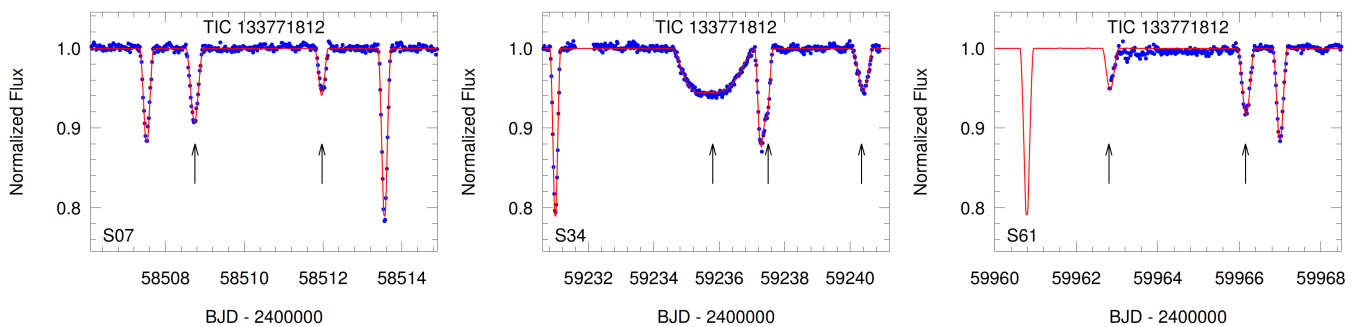


Fig. 1. Light curves (blue points) and model fits (smooth red curves) for the third-body eclipses of TIC 133771812. The third body eclipses are marked with vertical arrows. The sector numbers are indicated in the lower left corner of each panel. Calculation of the model curves will be discussed in Sect. 6.

by the tertiary star. Second is the ‘dynamical’ or ‘physical’ delays which, in nearly coplanar orbits, are caused largely by the lengthening of the EB orbit due to the presence of the tertiary star (see, e.g., Rappaport et al. 2013; Borkovits et al. 2015). This effect depends on the instantaneous separation between the EB and the tertiary star, and therefore varies with the phase of the outer orbit if that orbit is eccentric. (3) Finally, there is the well-known apsidal motion exhibited by eccentric binaries. This is a long timescale effect which has three different origins: (i) non-spherical mass distributions of the tidally distorted binary components; (ii) effects of general relativity and; (iii) perturbations forced by the tertiary star. The timescale of this latter effect, dynamically driven apsidal motion, is on the order of $P_{\text{out}}^2/P_{\text{in}}$ (Söderhjelm 1975), where P_{out} and P_{in} are the outer and inner binary periods, respectively. The two dominant drivers of apsidal motion in the systems reported here are due to the mutual tidal

deformations of the two EB stars and forced apsidal motion by the third body.

We see all three of these effects, namely, LTTE, dynamical delays, and apsidal motion, in the ETV curves of the seven triple systems reported in this work. The curves themselves are shown in Figures 10 – 15, while the mid-eclipse times used for the derivation of these ETV curves are tabulated in seven separate tables in Appendix A.

TIC 133771812: The ETV curve for TIC 133771812 with a 12-day EB and 244-day outer orbit (see Fig. 10) shows the sparse TESS sampling—essentially two sectors of data every two years. The smaller red and blue dots, connected with straight lines are the model fits (described in detail in Sect. 6) showing the periodic dynamical delays on the timescale of the outer orbit, and the convergence between the primary and secondary eclipse times, due to the apsidal motion, which in this case is being driven by

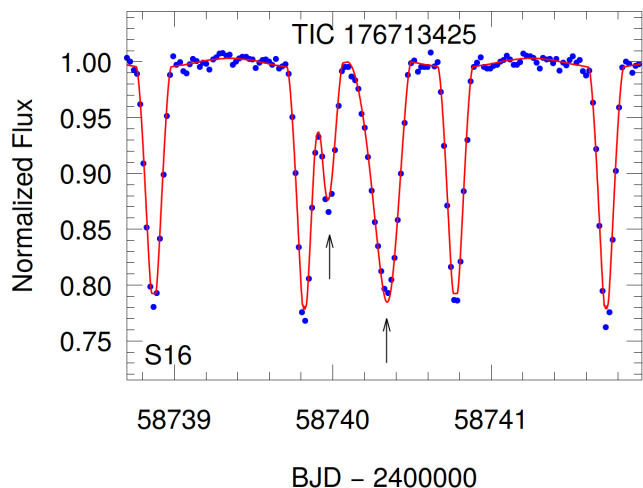


Fig. 2. Light curve (blue points) and model fit (smooth red curves) for the only third-body eclipse of TIC 176713425 observed with TESS. The third body eclipses are marked with vertical arrows. The other notation is the same as in Fig. 1.

the tertiary star. The variations in the ETV curve with the outer period of 244 d are $\sim 90\%$ dynamical delays and $\sim 10\%$ LTTE effects. As another way of illustrating the ratio of the LTTE contribution to the overall ETV curve, we superpose the pure LTTE contribution on the ETV curve for TIC 133771812. We then also show the LTTE contribution to the ETV curves for each of the other sources we investigate.

TIC 176713425: Figure 11 shows the ETV curve for TIC 176713425. Here there are 2+1 sectors of data separated by 3 years and, moreover, six ground-based eclipse times obtained within the framework of our photometric follow up campaigns. Fortunately we know the outer orbital period rather well from the archival data (see Fig. 9), namely 52.58 days. Thus, the Sector 16, 17, and 57 data are sufficient to determine satisfactorily the outer orbital parameters. The variations in the ETV curve with the outer orbital period of 52.58 d are $\sim 90\%$ dynamical delays and $\sim 10\%$ LTTE effects.

TIC 185615681: The ETV curve for TIC 185615681 shown in Fig. 12 has sparse points taken at roughly two-year intervals. Fortunately, the outer orbital period is also well measured both from the five sets of TESS-observed third-body eclipses and the archival data to be 55.9 d. The ETV variations with the period of the outer orbit are quite evident, as is the rapid apsidal motion forced by the third body. The former variations in the ETV curve are $\sim 65\%$ dynamical delays and $\sim 35\%$ LTTE effects. We also note that this is the only triple in our sample where ETV data prior to the TESS mission are also available in the literature (see Sect. 7.2.3).

This is the only system in our sample where the inner EB is a known double-lined spectroscopic binary (SB2) and, hence, RV data for the EB members are available (see Fig. 16) from the literature (Duerbeck & Rucinski 2007) and, we used these data for our analysis.

TIC 287756035: This is the only system in our sample where the ETV curve, derived from the TESS observations, is of no value. This is the case because the scatter of the measured mid-eclipse times exceeds the full amplitude of the model-ETV by more than an order of magnitude. On the other hand, however, we have obtained five RV points for the tertiary star which pro-

vides us with valuable information about the outer orbit in this system (see Fig. 17 and Table B.1 as well).

TIC 321978218: The left panel of Fig. 13 displays the ETV curve of TIC 321978218 as derived exclusively from the TESS observations. As one can see, the 57.5-day period outer orbit is completely covered both during the Year 3 (Sectors 28 and 29) and Year 5 (Sectors 68 and 69) TESS observations. This fact makes the determination of the outer orbital period and the other orbital elements quite robust without the use of the extra information carried by the third-body eclipses. Our analytic ETV fit also revealed the fact that the ETV is dominated by the LTTE effect ($\sim 73\%$) over the dynamical delays ($\sim 27\%$). Besides these data, we also obtained 17 RV points of the dominant tertiary star with the CHIRON instrument. These RV data also nicely cover the outer orbit (see Fig. 18 and Table B.2). A combination of the LTTE-dominated ETV curve, which describes the motion of the inner EB around the centre of mass of the triple system, and the RV curve, which reflects the tertiary’s motion, makes the outer pair a quasi-SB2 binary. In turn, one can determine both the outer mass ratio (q_{out}) and the total (projected) mass of the inner EB ($M_A \sin^3 i_{\text{out}} = M_{Aa} \sin^3 i_{\text{out}} + M_{Ab} \sin^3 i_{\text{out}}$) and the individual (projected) mass of the tertiary ($M_B \sin^3 i_{\text{out}}$) component purely from the amplitudes of the ETV and RV curves. However, the actual system turned out to be not so simple. The reason is that, after receiving the Sector 68 observations and then deriving ETV points from these data, we realized immediately that the ETV curve exhibits a further, longer timescale, non-linear variation. Sector 69 data confirmed these findings.

Then, we were able to extend our ETV study thanks to the archival SWASP observations. As was mentioned above, five seasons of SWASP observations are available for TIC 321978218. The lesser quality of these observations do not allow us to determine individual times of eclipses with the accuracies we achieve with TESS which would be necessary to study the low-amplitude ($\lesssim 10^{-3} d$) ETV variations. Hence, instead of using individual eclipse times, we formed seasonal folded, binned light curves from each of the five seasons of SWASP observations (using an EB period of $P_{\text{in}} = 0.5698127 d$). With the use of these seasonal average light curves, we determined five times of seasonal ‘eclipse points’ (both for the primary and secondary eclipses). Each of these results in a representative ETV value which we locate near to the mid-time of the observations used to make the average light curve. Moreover, since these seasonal folded EB light curves essentially average out the 57.5-day outer period ETV variations, we chose a location for the mean ETV point that is not only near the SWASP seasonal midtime, but one that is also near the time when the outer 57.5-day outer ETV value would be near zero. (In practice, this means that the tertiary’s orbital phase, measured from the middle of first TESS-observed third-body eclipse, was around $0^{\text{h}}17$ or $0^{\text{h}}73$.) These nominal seasonal ETV points extend the length of the available ETV data by almost 5 000 days and confirm that TIC 321978218 exhibits additional period variation(s) (see right panel of Fig. 13).

At this time we have insufficient information to say anything certain about the nature of these variations either qualitatively or quantitatively. In this study, however, we decided to model this extra ETV variation under the assumption that TIC 321978218 is a 2+1+1 type quadruple star system. We emphasize, however, that, though this assumption was necessary for a consistent modeling of the available datasets, there is no guarantee that the parameters of the outermost orbit and the fourth star mean much unless the outermost orbit is ultimately confirmed.

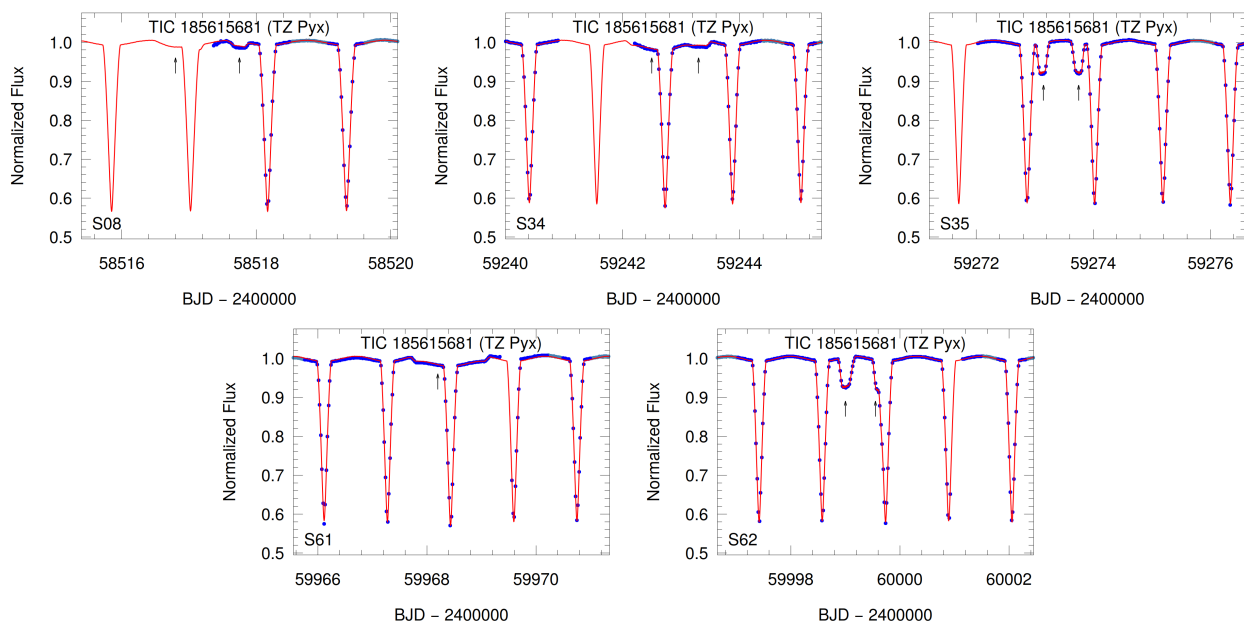


Fig. 3. Light curves (blue points) and model fits (smooth red curves) for the third-body eclipses of TIC 185615681 (marked with vertical arrows). The other notation is the same as in Fig. 1.

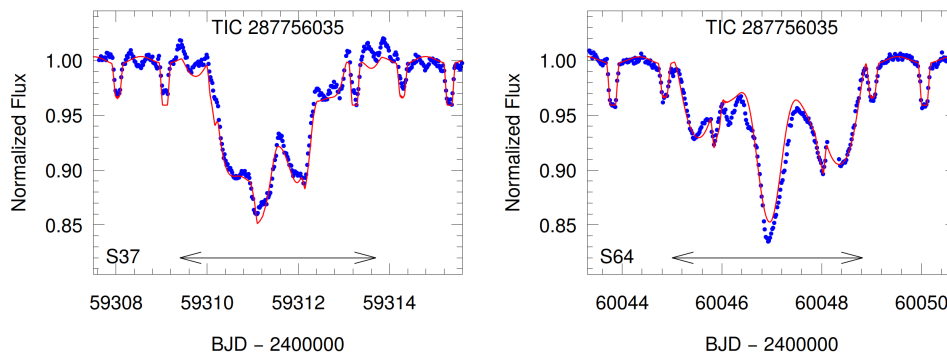


Fig. 4. Light curves (blue points) and model fits (smooth red curves) for the third-body eclipses of TIC 287756035 (marked by horizontal arrows). The other notation is the same as in Fig. 1.

TIC 323486857: The very noisy ETV curve of TIC 323486857 is shown in Fig. 14. The large uncertainties of the points, which make the ETV curve nearly unusable, are due to the highly distorted light curve. Fortunately, in addition to the Gaia spectroscopic solution for the outer orbit, nine individual third body eclipses were detected during the six TESS sectors and, hence, the outer period, which is the shortest among our sample, is well characterized. As can be seen in Fig. 14, the ETV curve is mainly dominated by the LTTE, which is expected for such a nearly flat, doubly circular triple star system.

TIC 650024463: Figure 15 shows an ETV curve for TIC 650024463 that is fairly well populated with data points from 9 sectors of data spanning more than four years of TESS observations. In addition to the well mapped out variations with the outer orbital period of 108 days, the better part of 2/3 of a complete apsidal motion cycle is observed. The ETV variations with the outer period of 108 d are $\sim 90\%$ dynamical delays and $\sim 10\%$ LTTE effects.

6. Photodynamical models

All seven of the triple systems in this work have been subjected to a detailed photodynamical analysis⁸ in order to extract all of the system parameters. For the photodynamical analysis we utilize the software package LIGHTCURVEFACTORY (see, e.g. Borkovits et al. 2019a, 2020a, and references therein). This code has been developed over the past decade and has been described in a number of previous papers. The code contains three basic features: (i) emulators for multi-passband light curve(s), the corresponding ETVs, and radial velocity curve (this feature is present whether or not we have actual RV data); (ii) a built-in numerical integrator (a seventh-order Runge-Kutta-Nyström algorithm) to calculate the perturbed three-, or multiple-body orbits, specifically, the coordinates and velocities of the three or more stars in the system; and (iii) a Markov Chain Monte Carlo (MCMC)-based search routine for determining the best-fit system parameters, and the statistical uncertainties, as well. The latter feature uses

⁸ To our knowledge, the first photodynamical analysis of a triply eclipsing triple system was carried out by Carter et al. (2011) for the system KOI-126.

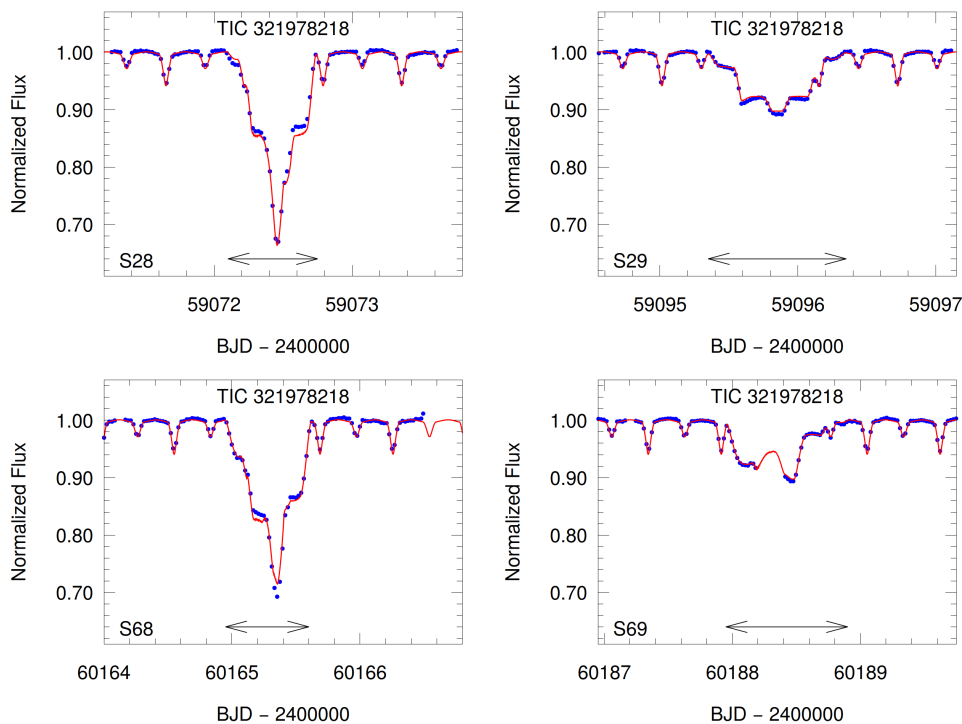


Fig. 5. Light curves (blue points) and model fits (smooth red curves) for the TESS-observed third-body eclipses of TIC 321978218 (marked by horizontal arrows). The other notation is the same as in Fig. 1.

our own implementation of the generic Metropolis-Hastings algorithm (see, e.g., Ford 2005).

LIGHTCURVEFACTORY was developed to analyze multiple star systems, including binaries, triples, and quadruple stars of both the 2+2 and 2+1+1 architecture. The workings of the code, the steps involved in the analysis procedure, and its application to a wide range of multi-stellar systems have been explained in detail (Borkovits et al. 2018, 2019a,b, 2020a,b, 2021; Mitnyan et al. 2020). Specifically LIGHTCURVEFACTORY has been used successfully to analyse compact and wider triple systems, both with and without outer eclipses.

Essentially all the details of how this code was used to analyze the compact triply eclipsing triple systems that were found with TESS, were described in Rappaport et al. (2022). Therefore, here we will provide only a high-level overview of the inputs to the code and the parameters that are either fitted or constrained by the MCMC fit. Altogether, in the case of a hierarchical triple configuration, there are 25 – 27 system parameters that result directly from the analysis. Specifically, these are all the stellar parameters (9 = 3 × mass, radius, T_{eff}), all 12 of the elements of the inner and outer orbits, to which, in the case of radial velocity data, one can add the systemic radial velocity as a thirteenth orbital parameter, as well as the 4 system parameters: distance to the source and the interstellar extinction, as well as the system metallicity and age. Finally, one may optionally adjust the amount of any passband-dependent contaminated (extra) light ℓ_4 if it is necessary.

The LIGHTCURVEFACTORY code obviously requires a substantial amount of ‘input’ information in order to allow for the extraction of 26 independent system parameters. This input information can be divided into two basic categories. First, there are the ‘data’. These include: the (i) EB eclipse profiles, (ii) third-body eclipse profile(s), (iii) times of the EB eclipses which are distinct from the shape and depths of eclipses, (iv) archival SED values, and (v) radial velocities (available only for three

Table 5. Definitions of triple system parameters in Tables 6– 9

Parameter ^a	Definition
t_0	Epoch time for osculating elements
P	Orbital period
a	Orbital semimajor axis
e	Orbital eccentricity
ω	Argument of periastron (of secondary)
i	Orbital inclination angle
$\mathcal{T}_0^{\text{inf/sup}}$	Time of conjunction of the secondary ^b
τ	Time of periastron passage
Ω	Longitude of the node relative to the node of the inner orbit
i_{mut}	Mutual inclination angle ^c
q	Mass ratio (secondary/primary)
K_{pri}	“K” velocity amplitude of primary
K_{sec}	“K” velocity amplitude of secondary
R/a	Stellar radius divided by semimajor axis
$T_{\text{eff}}/T_{\text{eff,Aa}}$	Temperature relative to EB primary
fractional flux	Stellar contribution in the given band
M	Stellar mass
R	Stellar radius
T_{eff}	Stellar effective temperature
L_{bol}	Stellar bolometric luminosity
M_{bol}	Stellar absolute bolometric magnitude
M_V	Stellar absolute visual magnitude
$\log g$	log surface gravity (cgs units)
$[M/H]$	log metallicity abundance to H, by mass
$E(B - V)$	Color excess in B-V bands
extra light, ℓ_4	Contaminating flux in the given band
$(M_V)_{\text{tot}}$	System absolute visual magnitude
distance	Distance to the source

Notes. (a) The units for the parameters are given in Tables 6– 9. (b) The superscript of “inf/sup” indicates inferior vs. superior conjunctions.

(By default we give inferior conjunctions. Superior conjunctions are indicated by asterisks.) (c) More explicitly, this is the angle between the orbital planes of the inner binary and the outer triple orbit.

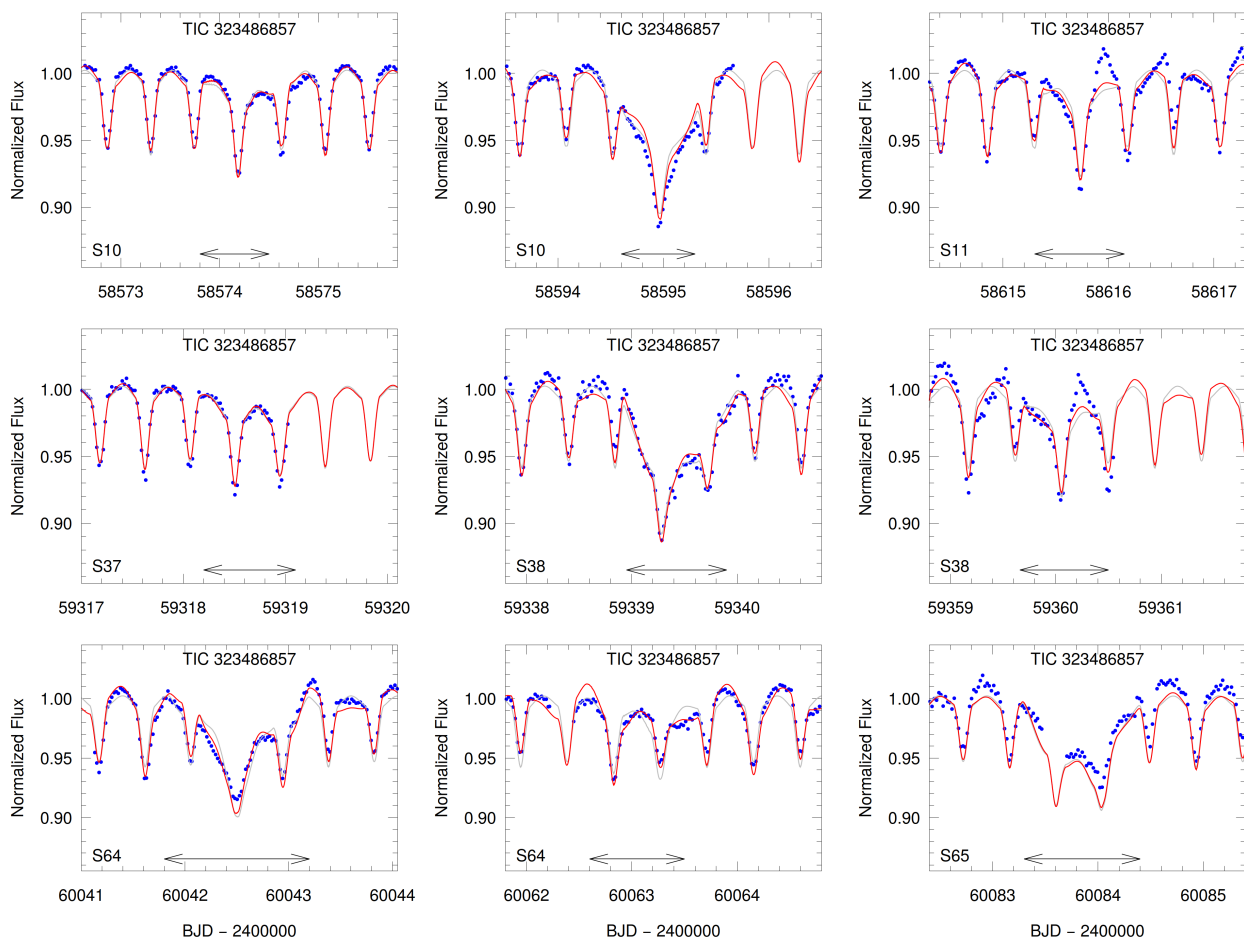


Fig. 6. Light curves (blue points) and two kinds of model fits for TIC 323486857. The light-gray fit represents the pure three-body model light curve, while the red fit is the net fit of the triple star model and a four-frequency Fourier model of the light curve distortions (see text for details). The region of the third-body eclipses is indicated with the horizontal arrows. The other notation is the same as in Fig. 1.

of our systems). Second, we utilize PARSEC model stellar evolution tracks and isochrones as well as model stellar atmospheres (Bressan et al. 2012). The evolution tracks enable us to find the stellar radius and T_{eff} for a given stellar mass, age and metallicity, while the isochrones allow us to compute stellar magnitudes in different passbands in order to fit the SED curve. The available input information for each of the seven triples is summarized in Table 4.

The EB and third-body eclipse profiles and the ETV curves used in the photodynamical analysis were taken from the TESS full-frame images (‘FFI’). The photometry on the FFIs was done with Andras Pal’s FITSH package (Pál 2012). In order to save on computational time we binned the 10-min cadence data to 30-min cadence⁹, and dropped the out-of-eclipse regions of these light curves, keeping only the ± 0.15 phase-domain regions around the EB eclipses themselves. However, whenever a data segment contains a third-body (i.e., ‘outer’) eclipse, we keep the data for an entire binary period before and after the first and last contacts of that particular third-body eclipse.

As noted in Table 3, we have RV data for only three of the seven sources. This may raise the question of how we are able

⁹ While LIGHTCURVEFACTORY is able to handle directly finite exposure times, we found that finite exposure (more, strictly speaking cadence-) time corrections were unnecessary to apply even for the 30-min cadence light curves, due to the relatively long durations of both the inner and outer eclipses compared to the cadence times.

to derive absolute stellar masses, temperatures, and radii. Here we provide a qualitative answer to this question. There are in fact several pieces of information that involve combinations of the masses. First, the ETV curve contains information about the light travel time effect and that, in turn, is equivalent to an SB1 RV measurement of the outer orbit. We have useable ETV data for six of the seven sources (see Table 3). And, for that one case where we have no ETV curve, there are RV data (for the tertiary). We note that the same information is also encoded into the light curves, as the light curves are fitted in the time-domain. Finally in this regard, the ETV curve (and the light curve, as well) also contain signatures of the dynamical delays which, in turn, carry information about primarily q_{out} and, in a less certain way (through the higher order perturbations), about q_{in} (see, e.g., Borkovits et al. 2015).

Additionally, the geometry and timing of the outer eclipses carry significant further information about the ratio of $q_{\text{out}}/q_{\text{in}}$, as was elaborated on, for example, in Appendix A of Borkovits et al. (2013). It is even intuitive that, while the inner eclipses provide information about $R_{Aa,Ab}/a_{\text{in}}$, the outer eclipses provide information about $R_{Aa,Ab,B}/a_{\text{out}}$ and, hence, their combination leads to the above mentioned ratio of mass ratios.

We did not use spectroscopically determined temperatures and metallicities for most of the systems (as they are unavailable) but, instead, we use SED fits to determine or constrain absolute temperatures. This information is also combined with the results

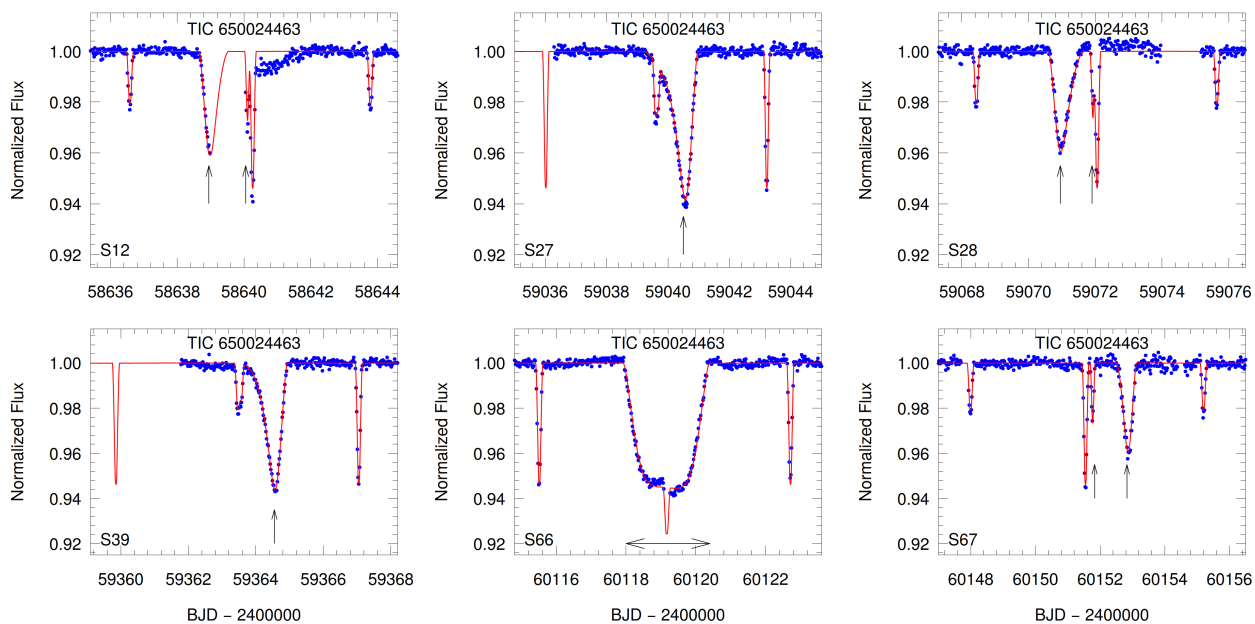


Fig. 7. Light curves (blue points) and model fits (smooth red curves) for TIC 650024463. The vertical and horizontal arrows mark the times of third body eclipses. The other notation is the same as in Fig. 1.

of the simultaneous light curve fits, the latter of which also give combinations of the ratios of the surface brightnesses and, hence, indirectly the absolute temperature of the three stars. Primarily these may be obtained from combinations of the eclipse depths of the inner and outer eclipses. Here one should keep in mind that the ratio of the surface brightnesses of the inner EB components can be obtained not only from the mutual eclipses of the inner components, but also from those events where the inner EB members eclipse (or are eclipsed by) the tertiary star separately. Hence from a light curve containing both inner and outer eclipses, the information which can be mined out is not simply the sum of the parameters that can be determined from two independent eclipsing light curves, but much more. The use of SED information to obtain temperatures is also employed in several other recent papers, for example in Miller et al. (2020) and Stassun & Torres (2016).

Finally, we combine this SED information with theoretical, coeval stellar isochrones which provide information not only on the radii and T_{eff} of the stars, but also the masses for a given age (but of course, such masses are no longer independent of the astrophysical assumptions and, hence, they may be somewhat inferior to those dynamical masses which can be directly inferred from high quality RV data). We discuss this question in detail in Borkovits et al. (2020a, 2022a). All the stars are typically tied together via a “coeval” assumption. And, of course, knowledge of the masses sets the size scales of the system, which then provides for absolute determinations of semi-major axes and stellar radii.

7. System parameters

7.1. Tables of fitted parameters

With the use of the 25–27 directly fitted system parameters, one can also determine a number of other astrophysically and/or dynamically relevant additional parameters for each star in the triple. Thus, we can include all the basic stellar parameters in our tabulated results, as well as the inner and outer orbital parameters discussed above, including the relative orientations of the two

orbits. We also give several relative values (e.g., R/a , T_B/T_{Aa}), some global system parameters such as distance, $[M/H]$, and $E(B - V)$, and a number of parameters that are derived from the fitted parameters. Each of the results tables contains a few dozen different parameters which are, for the most part, written as symbols only. These symbols were defined in Rappaport et al. (2023), but for the sake of completeness we repeat these definitions here in Table 5. Then, the system parameters that are derived from the photodynamical analyses are listed in Tables 6 through 9.

Before discussing the results individually for each system, we make one other important point. The orbital parameters (including also the inner and outer periods) tabulated below are instantaneous, osculating orbital elements, which are valid strictly only for the specific epoch t_0 which is given in the very first row of each table. Therefore, the given periods and conjunction times are not applicable for observational predictions (i.e. for determining times of future inner or outer eclipses). For these latter purposes we provide Table 10 which contains, among other things, the inner and outer eclipsing periods of the sources, and should be used for planning occasional future observations.

7.2. Results for the individual systems

7.2.1. TIC 133771812

This is the only target in our sample for which we were unable to obtain a reasonable third-body orbit fold from the archival data. Thus, in order to determine the outer period we had to restrict ourselves to just the three sets of third-body eclipses observed with TESS in years 1, 3 and 5, and to the high quality ETV data obtained from these observations. Our analytic ETV solutions preferred an outer period of $P_{\text{out}} \sim 244$ d, but allowed also for half that period, namely, $P_{\text{out}} \sim 122$ d. We produced preliminary photodynamical solutions for both outer periods, and we found that the true period should actually be about $P_{\text{out}} \sim 244$ days. In other words, we were unable to find both dynamically and astrophysically consistent and reliable solutions with the shorter outer

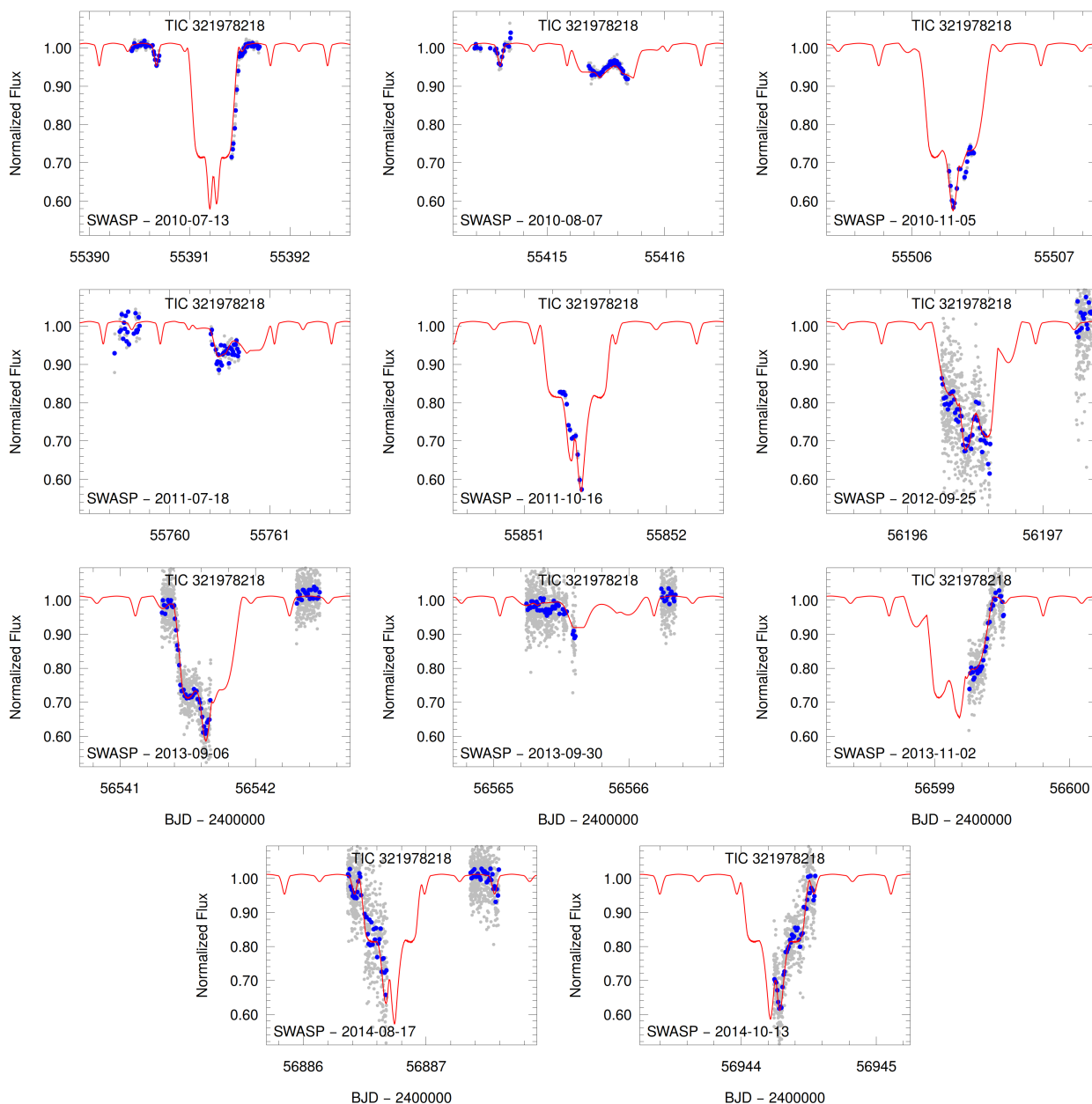


Fig. 8. Eleven partially observed third-body eclipses of TIC 321978218 from the five seasons of the SWASP project. Gray dots represent the individual observations, while larger blue circles denote their 10-min. averages which were used for the joint photodynamical analysis. Red curves stand for the best-fit model.

period. We have tabulated the median posteriors of the adjusted parameters and several further derived quantities of the complex photodynamical analysis in the first three columns of Table 6.

According to our results, all three components of TIC 133771812 are somewhat more massive than our Sun. The inner EB consists of the most and least massive ($M_{Aa} = 1.58 \pm 0.04 M_{\odot}$ and $M_{Ab} = 1.20 \pm 0.03 M_{\odot}$, respectively) and, correspondingly, the hottest and coolest ($T_{Aa} = 7700 \pm 160$ K and $T_{Ab} = 6410 \pm 100$ K) stars of the triple. The third component lies in between the two EB members both in its mass and temperature, but is closer to the secondary of the inner EB with $M_B = 1.25 \pm 0.03 M_{\odot}$ and $T_B = 6550 \pm 110$ K. The inferred masses, in the absence of RV data, have relatively large uncertainties of $\sim 3 - 4\%$. Relative quantities, such as the mass ratios, however, can be deduced with better accuracies. These are found to be $q_{in} = 0.763 \pm 0.006$ and $q_{out} = 0.449 \pm 0.010$.

Amongst all the triply eclipsing triple stars which were analyzed photodynamically in our present and former papers, TIC 133771812 has by far the longest inner EB period with $P_{in} = 12^d.33$. Thus, despite the fact that the inferred outer period ($P_{out} = 243^d.9$) is the second longest in the current set, this target is still the second tightest ($P_{out}/P_{in} \approx 19.8$) among these seven triply eclipsing triples. Due the relative large size of the inner EB and, hence, the small fractional radii ($r_{Aa} = R_{Aa}/a_{in} = 0.0491 \pm 0.0005$ and $r_{Ab} = 0.0368 \pm 0.0008$), tidal effects are certainly negligible. Hence, not surprisingly, this inner EB has the largest eccentricity with $e_{in} = 0.0337 \pm 0.0004$ among our present sample. The combination of inner and outer ($e_{out} = 0.217 \pm 0.006$) eccentricities, combined with the tightness of the system, still leaves it safely within the dynamically stable region according to the Mardling & Aarseth (2001) stability criterion.

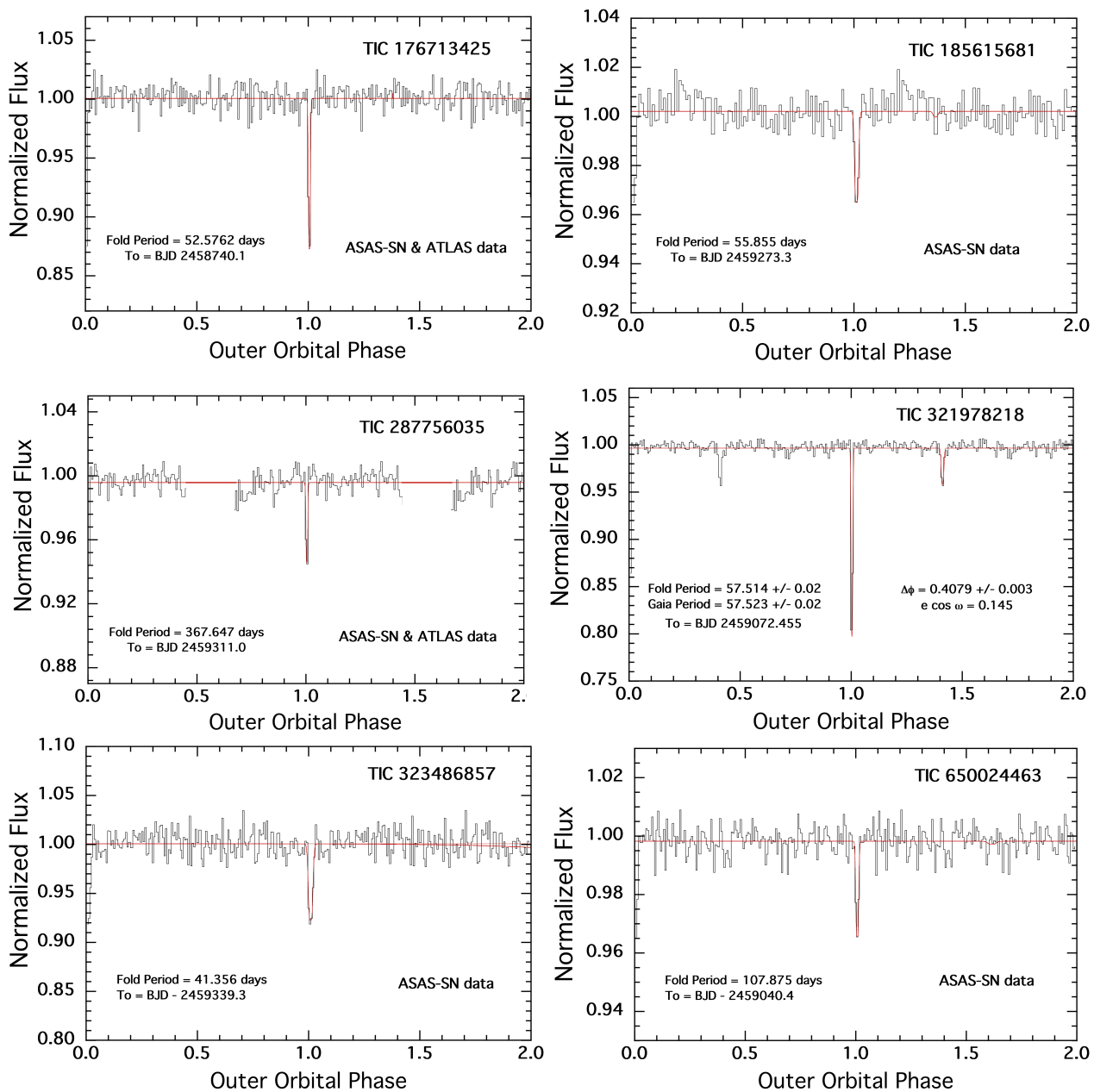


Fig. 9. Archival outer orbit folds. The ASAS-SN and ATLAS archival data were used to find the outer period of these triple systems independently of what we were able to learn from ETV or RV curves, or third-body eclipses observed with TESS. Typically, there are 3000-6000 archival photometric points spanning a decade. In the case of TIC 287756035, there is about 1/4 of the outer orbital phase which is missing due to the fact that the outer period nearly exactly matches that of the Earth year, and the consequential observing seasons. The light red curves are fits to a non-physical function consisting of a modified hyperbolic secant (e.g., Eqn. 1 of Rappaport et al. 2016). The fit covers only one of the two cycles for clarity in viewing the eclipses, and is used only to find the phases of the eclipses.

7.2.2. TIC 176713425

This is the only northern (ecliptic) hemisphere target amongst the currently investigated triples. Its original FITSH light curves were partially blended with the nearby overcontact binary ATO J353.9138+42.3630 (TIC 176713436). Hence, to eliminate the signal of the latter object from the light curve of our target, we applied a principal component analysis (PCA) method implemented in the `lightcurve` (Lightcurve Collaboration 2018) Python package and its dependencies: `astropy` (Astropy Collaboration 2018), `astroquery` (Ginsburg et al. 2019) and `TESScut` (Brasseur et al. 2019).

We achieved this by creating 60×60 pixel size cutouts around the target and choosing an aperture such that the contaminating star also has some contribution in the image region outside the aperture. After that, we created a design matrix containing regressors from all pixels surrounding the aperture and calculated the principal component vectors using `lightcurve`'s built-in PCA method. These principal components are a combination of signals from scattered light, spacecraft motion and the nearby contaminating star. As a final step, we used the built-in `RegressionCorrector` method of `lightcurve` that uses linear algebra to find a combination of these principal component vectors that will transform the input light curve closest to zero. As the mean flux level of the light curve is different from zero, an additional offset

Table 6. Orbital and astrophysical parameters of TICs 133771812 and 176713425 from the joint photodynamical light curve, ETV, SED and PARSEC isochrone solution.

	TIC 133771812			TIC 176713425		
	Orbital elements			Subsystem		
	Aa-Ab	A-B		Aa-Ab	A-B	
t_0 [BJD - 2400000]	58491.0			58738.5		
P [days]	12.33390 ^{+0.00045} _{-0.00051}	243.8900 ^{+0.0048} _{-0.0059}		1.895107 ^{+0.000101} _{-0.000090}	52.943 ^{+0.019} _{-0.017}	
a [R_\odot]	31.66 ^{+0.20} _{-0.30}	262.0 ^{+1.6} _{-2.2}		8.456 ^{+0.082} _{-0.069}	89.42 ^{+0.77} _{-0.74}	
e	0.03368 ^{+0.00043} _{-0.00044}	0.2174 ^{+0.0058} _{-0.0058}		0.00592 ^{+0.00058} _{-0.00056}	0.4118 ^{+0.0072} _{-0.0070}	
ω [deg]	230.39 ^{+0.55} _{-0.61}	194.91 ^{+0.78} _{-0.81}		105.1 ^{+2.5} _{-2.2}	95.22 ^{+0.87} _{-0.58}	
i [deg]	89.98 ^{+0.11} _{-0.13}	89.770 ^{+0.019} _{-0.020}		88.56 ^{+0.66} _{-0.73}	88.714 ^{+0.084} _{-0.089}	
$\mathcal{T}_0^{\text{inf/sup}}$ [BJD - 2400000]	58501.1638 ^{+0.0004} _{-0.0003}	58509.928 ^{+0.009*} _{-0.010}		58739.8183 ^{+0.0001} _{-0.0001}	58740.0972 ^{+0.0040*} _{-0.0041}	
τ [BJD - 2400000]	58499.8871 ^{+0.0185} _{-0.0209}	58320.200 ^{+0.383} _{-0.554}		58738.951 ^{+0.013} _{-0.012}	58687.448 ^{+0.054} _{-0.042}	
Ω [deg]	0.0	-0.22 ^{+0.13} _{-0.11}		0.0	0.62 ^{+0.96} _{-0.77}	
i_{mut} [deg]		0.31 ^{+0.14} _{-0.14}			1.00 ^{+0.83} _{-0.52}	
ϖ^{dyn} [deg]	50.39 ^{+0.55} _{-0.61}	14.91 ^{+0.78} _{-0.81}		285.1 ^{+2.5} _{-2.2}	275.22 ^{+0.87} _{-0.58}	
i^{dyn} [deg]	0.25 ^{+0.11} _{-0.12}	0.06 ^{+0.03} _{-0.03}		0.83 ^{+0.69} _{-0.43}	0.17 ^{+0.14} _{-0.09}	
Ω^{dyn} [deg]	228 ⁺¹⁵ ₋₁₄	48 ⁺¹⁵ ₋₁₄		72 ⁺¹⁰⁸ ₋₂₉	252 ⁺¹⁰⁸ ₋₂₉	
i_{inv} [deg]		89.81 ^{+0.03} _{-0.04}			88.68 ^{+0.14} _{-0.11}	
Ω_{inv} [deg]		-0.18 ^{+0.10} _{-0.09}			0.52 ^{+0.80} _{-0.64}	
mass ratio [$q = M_{\text{sec}}/M_{\text{pri}}$]	0.7627 ^{+0.0054} _{-0.0057}	0.4488 ^{+0.0099} _{-0.0092}		0.9334 ^{+0.0052} _{-0.0048}	0.5150 ^{+0.0042} _{-0.0041}	
K_{pri} [km s^{-1}]	56.23 ^{+0.30} _{-0.37}	17.26 ^{+0.32} _{-0.31}		109.01 ^{+0.87} _{-0.83}	31.92 ^{+0.24} _{-0.35}	
K_{sec} [km s^{-1}]	73.76 ^{+0.45} _{-0.61}	38.44 ^{+0.33} _{-0.34}		116.67 ^{+0.31} _{-0.98}	61.86 ^{+0.70} _{-0.53}	
Apsidal and nodal motion related parameters						
P_{apse} [year]	52.81 ^{+0.78} _{-0.81}	225.0 ^{+1.8} _{-1.6}		7.09 ^{+0.13} _{-0.12}	59.71 ^{+0.82} _{-0.85}	
$P_{\text{apse}}^{\text{dyn}}$ [year]	23.64 ^{+0.31} _{-0.32}	35.96 ^{+0.35} _{-0.34}		4.15 ^{+0.05} _{-0.05}	8.57 ^{+0.09} _{-0.10}	
$P_{\text{node}}^{\text{dyn}}$ [year]		42.81 ^{+0.51} _{-0.51}			10.01 ^{+0.11} _{-0.11}	
$\Delta\omega_{3b}$ [arcsec/cycle]	1850 ⁺²⁵ ₋₂₄	24064 ⁺²³¹ ₋₂₃₃		1231 ⁺¹⁴ ₋₁₃	21915 ⁺²⁵⁵ ₋₂₃₉	
$\Delta\omega_{\text{GR}}$ [arcsec/cycle]	0.731 ^{+0.009} _{-0.014}	0.134 ^{+0.002} _{-0.002}		2.207 ^{+0.043} _{-0.036}	0.381 ^{+0.007} _{-0.007}	
$\Delta\omega_{\text{tide}}$ [arcsec/cycle]	0.179 ^{+0.009} _{-0.009}	0.00051 ^{+0.00003} _{-0.00003}		387 ⁺¹⁵ ₋₁₇	0.638 ^{+0.0171} _{-0.028}	
Stellar parameters						
	Aa	Ab	B	Aa	Ab	B
Relative quantities						
fractional radius [R/a]	0.0491 ^{+0.0004} _{-0.0005}	0.0368 ^{+0.0008} _{-0.0008}	0.0047 ^{+0.0002} _{-0.0001}	0.2060 ^{+0.0018} _{-0.0018}	0.1525 ^{+0.0024} _{-0.0041}	0.0189 ^{+0.0011} _{-0.0008}
temperature relative to $(T_{\text{eff}})_{\text{Aa}}$	1	0.8345 ^{+0.0049} _{-0.0058}	0.8486 ^{+0.0139} _{-0.0095}	1	1.0039 ^{+0.0025} _{-0.0022}	1.0040 ^{+0.0032} _{-0.0095}
fractional flux [in TESS-band]	0.3476 ^{+0.0141} _{-0.0121}	0.1141 ^{+0.0016} _{-0.0015}	0.1341 ^{+0.0137} _{-0.0120}	0.3657 ^{+0.0110} _{-0.0107}	0.2037 ^{+0.0025} _{-0.0024}	0.3552 ^{+0.0260} _{-0.0256}
fractional flux [in Cousins R_C -band]	–	–	–	0.3808 ^{+0.0123} _{-0.0122}	0.2134 ^{+0.0063} _{-0.0052}	0.3770 ^{+0.0171} _{-0.0321}
Physical quantities						
M [M_\odot]	1.588 ^{+0.028} _{-0.044}	1.209 ^{+0.026} _{-0.033}	1.254 ^{+0.034} _{-0.035}	1.166 ^{+0.037} _{-0.029}	1.091 ^{+0.028} _{-0.029}	1.164 ^{+0.025} _{-0.031}
R [R_\odot]	1.554 ^{+0.017} _{-0.017}	1.165 ^{+0.031} _{-0.034}	1.225 ^{+0.046} _{-0.041}	1.743 ^{+0.024} _{-0.027}	1.290 ^{+0.027} _{-0.027}	1.692 ^{+0.105} _{-0.072}
T_{eff} [K]	7706 ⁺¹⁶⁸ ₋₁₄₄	6426 ⁺¹¹² ₋₈₉	6561 ⁺¹⁰³ ₋₁₁₄	6033 ⁺⁷⁸ ₋₁₉₂	6051 ⁺⁷⁷ ₋₁₅₃	6033 ⁺⁹⁷ ₋₁₆₀
L_{bol} [L_\odot]	7.66 ^{+0.67} _{-0.61}	2.08 ^{+0.23} _{-0.22}	2.49 ^{+0.35} _{-0.29}	3.63 ^{+0.20} _{-0.55}	2.01 ^{+0.13} _{-0.23}	3.43 ^{+0.42} _{-0.43}
M_{bol}	2.56 ^{+0.09} _{-0.09}	3.97 ^{+0.12} _{-0.11}	3.78 ^{+0.13} _{-0.14}	3.37 ^{+0.18} _{-0.06}	4.01 ^{+0.13} _{-0.07}	3.43 ^{+0.15} _{-0.12}
M_V	2.52 ^{+0.09} _{-0.09}	3.97 ^{+0.12} _{-0.12}	3.77 ^{+0.14} _{-0.15}	3.39 ^{+0.20} _{-0.06}	4.03 ^{+0.15} _{-0.07}	3.44 ^{+0.16} _{-0.12}
$\log g$ [dex]	4.253 ^{+0.009} _{-0.008}	4.388 ^{+0.016} _{-0.015}	4.358 ^{+0.019} _{-0.021}	4.022 ^{+0.007} _{-0.007}	4.254 ^{+0.012} _{-0.012}	4.043 ^{+0.040} _{-0.047}
Global system parameters						
$\log(\text{age})$ [dex]		8.760 ^{+0.142} _{-0.053}			9.720 ^{+0.097} _{-0.021}	
$[M/H]$ [dex]		-0.009 ^{+0.049} _{-0.094}			0.076 ^{+0.080} _{-0.126}	
$E(B - V)$ [mag]		0.425 ^{+0.024} _{-0.023}			0.158 ^{+0.022} _{-0.045}	
extra light ℓ_4 [in TESS-band]		0.407 ^{+0.016} _{-0.026}			0.075 ^{+0.023} _{-0.022}	
extra light ℓ_4 [in Cousins R_C -band]		–			0.026 ^{+0.031} _{-0.015}	
$(M_V)_{\text{tot}}$		2.03 ^{+0.08} _{-0.10}			2.39 ^{+0.18} _{-0.06}	
distance [pc]		1428 ⁺³² ₋₂₇			2097 ⁺⁵¹ ₋₅₁	

term has to be used by appending a constant term to the design matrix. In this way, all of the previously mentioned signals were modeled and eliminated from the light curve of the target.

Due to the northerly position of the target, we were able to obtain photometric follow up observations in Hungarian observatories, and thereby observed eight additional regular eclipses

(four primary and four secondary minima)¹⁰ with the two identical 80 cm RC telescopes of Baja Astronomical Observatory and Gothard Astrophysical Observatory, Szombathely (for short descriptions of the instruments used see Borkovits et al. 2022a).

¹⁰ We note, however, that the last four eclipse times were obtained only after the photodynamical analysis was finalized. Despite this, they are plotted in Fig. 11 and also tabulated in Table A.2. These additional measurements are in perfect accord with the photodynamical model.

Table 7. Orbital and astrophysical parameters of TICs 185615681 and 287756035 from the joint photodynamical light curve, ETV, SED and PARSEC isochrone solution.

	TIC 185615681			TIC 287756035		
	Orbital elements					
	Subsystem			Subsystem		
	Aa–Ab		A–B	Aa–Ab		A–B
t_0 [BJD - 2400000]	58516.0			58596.5		
P [days]	2.3180401 ^{+0.000064} _{-0.000066}		56.06661 ^{+0.00071} _{-0.00066}	2.082184 ^{+0.000102} _{-0.000082}		367.923 ^{+0.022} _{-0.023}
a [R_\odot]	11.718 ^{+0.073} _{-0.057}		104.78 ^{+0.57} _{-0.52}	8.725 ^{+0.049} _{-0.112}		318.1 ^{+2.1} _{-4.5}
e	0.010669 ^{+0.000087} _{-0.000071}		0.09817 ^{+0.00087} _{-0.00084}	0.0036 ^{+0.0012} _{-0.0012}		0.235 ^{+0.019} _{-0.025}
ω [deg]	207.87 ^{+0.58} _{-0.41}		308.74 ^{+0.54} _{-0.51}	175 ⁺²⁷ ₋₃₁		53.70 ^{+0.63} _{-0.66}
i [deg]	88.06 ^{+0.11} _{-0.12}		89.826 ^{+0.071} _{-0.097}	89.27 ^{+0.59} _{-0.83}		89.095 ^{+0.049} _{-0.028}
$\mathcal{T}^{\text{inf/sup}}$ [BJD - 2400000]	58518.17078 ^{+0.00004} _{-0.00004}		58517.269 ^{+0.015*} _{-0.015}	58599.3048 ^{+0.0009} _{-0.0008}		59311.672 ^{+0.039} _{-0.021}
τ [BJD - 2400000]	58517.777 ^{+0.004} _{-0.003}		58496.431 ^{+0.015} _{-0.079}	58598.76 ^{+0.16} _{-0.18}		59071.8 ^{+1.4} _{-1.1}
Ω [deg]	0.0		2.17 ^{+0.13} _{-0.14}	0.0		1.22 ^{+0.64} _{-0.54}
i_{mut} [deg]	2.79 ^{+0.17} _{-0.16}			1.39 ^{+0.60} _{-0.49}		
ϖ^{dyn} [deg]	27.83 ^{+0.57} _{-0.41}		128.74 ^{+0.54} _{-0.51}	355 ⁺²⁷ ₋₃₁		233.71 ^{+0.63} _{-0.66}
i^{dyn} [deg]	1.97 ^{+0.12} _{-0.12}		0.82 ^{+0.05} _{-0.05}	1.27 ^{+0.55} _{-0.44}		0.12 ^{+0.05} _{-0.04}
Ω^{dyn} [deg]	50.8 ^{+1.9} _{-1.8}		230.8 ^{+1.9} _{-1.8}	98 ⁺²⁷ ₋₃₇		278 ⁺²⁷ ₋₃₇
i_{inv} [deg]	89.30 ^{+0.08} _{-0.08}			89.12 ^{+0.04} _{-0.06}		
Ω_{inv} [deg]	1.53 ^{+0.10} _{-0.10}			1.12 ^{+0.59} _{-0.50}		
mass ratio [$q = M_{\text{sec}}/M_{\text{pri}}$]	0.998 ^{+0.002} _{-0.002}		0.221 ^{+0.002} _{-0.003}	1.193 ^{+0.019} _{-0.018}		0.552 ^{+0.004} _{-0.005}
K_{pri} [km s^{-1}]	127.76 ^{+0.77} _{-0.63}		17.21 ^{+0.15} _{-0.16}	115.44 ^{+1.30} _{-2.27}		16.01 ^{+0.19} _{-0.21}
K_{sec} [km s^{-1}]	127.99 ^{+0.80} _{-0.65}		77.81 ^{+0.57} _{-0.38}	96.58 ^{+0.49} _{-0.53}		28.95 ^{+0.24} _{-0.27}
V_γ [km s^{-1}]	-5.97 ^{+0.15} _{-0.16}			-3.90 ^{+0.27} _{-0.20}		
Apsidal and nodal motion related parameters						
P_{apse} [year]	18.17 ^{+0.15} _{-0.12}		64.38 ^{+0.09} _{-0.11}	6.56 ^{+0.68} _{-0.69}		6429 ⁺¹⁴² ₋₁₁₇
$P_{\text{apse}}^{\text{dyn}}$ [year]	9.28 ^{+0.07} _{-0.05}		14.67 ^{+0.07} _{-0.05}	6.49 ^{+0.66} _{-0.68}		515 ⁺¹⁰ ₋₉
$P_{\text{node}}^{\text{dyn}}$ [year]	18.99 ^{+0.09} _{-0.13}			560 ⁺¹⁰ ₋₁₁		
$\Delta\omega_{3b}$ [arcsec/cycle]	738.6 ^{+4.3} _{-5.9}		13564 ⁺⁴⁷ ₋₆₅	25.22 ^{+0.45} _{-0.42}		2535 ⁺⁴⁵ ₋₅₀
$\Delta\omega_{\text{GR}}$ [arcsec/cycle]	2.832 ^{+0.035} _{-0.028}		0.391 ^{+0.004} _{-0.004}	1.946 ^{+0.022} _{-0.050}		0.087 ^{+0.002} _{-0.014}
$\Delta\omega_{\text{tide}}$ [arcsec/cycle]	144.4 ^{+1.7} _{-1.6}		0.227 ^{+0.003} _{-0.003}	1112 ⁺¹³² ₋₁₀₆		0.131 ^{+0.014} _{-0.012}
Stellar parameters						
	Aa	Ab	B	Aa	Ab	B
Relative quantities						
fractional radius [R/a]	0.1749 ^{+0.0005} _{-0.0005}	0.1744 ^{+0.0005} _{-0.0005}	0.00749 ^{+0.00008} _{-0.00008}	0.1129 ^{+0.0018} _{-0.0017}	0.2707 ^{+0.0061} _{-0.0054}	0.0212 ^{+0.0006} _{-0.0008}
temperature relative to $(T_{\text{eff}})_{\text{Aa}}$	1	0.9986 ^{+0.0014} _{-0.0014}	0.5633 ^{+0.0042} _{-0.0057}	1	0.9126 ^{+0.0095} _{-0.0117}	0.8043 ^{+0.0115} _{-0.0053}
fractional flux [in TESS-band]	0.4840 ^{+0.0039} _{-0.0035}	0.4806 ^{+0.0039} _{-0.0036}	0.0126 ^{+0.0007} _{-0.0007}	0.0372 ^{+0.0016} _{-0.0015}	0.1537 ^{+0.0065} _{-0.0065}	0.7708 ^{+0.0170} _{-0.0174}
Physical quantities						
M [M_\odot]	2.009 ^{+0.038} _{-0.030}	2.005 ^{+0.037} _{-0.032}	0.888 ^{+0.014} _{-0.013}	0.935 ^{+0.013} _{-0.023}	1.116 ^{+0.027} _{-0.054}	1.133 ^{+0.029} _{-0.269}
R [R_\odot]	2.051 ^{+0.012} _{-0.013}	2.045 ^{+0.012} _{-0.012}	0.785 ^{+0.011} _{-0.011}	0.986 ^{+0.017} _{-0.020}	2.361 ^{+0.060} _{-0.055}	6.753 ^{+0.205} _{-0.318}
T_{eff} [K]	9122 ⁺¹⁴⁰ ₋₁₁₀	9108 ⁺¹³⁷ ₋₁₀₉	5136 ⁺⁶⁴ ₋₆₂	6025 ⁺³⁷ ₋₁₆₆	5501 ⁺⁵⁴ ₋₂₀₇	4833 ⁺⁵³ ₋₅₀
L_{bol} [L_\odot]	23.11 ^{+2.30} _{-2.45}	22.92 ^{+2.29} _{-2.49}	0.449 ^{+0.050} _{-0.045}	1.14 ^{+0.06} _{-0.11}	4.59 ^{+0.26} _{-0.80}	22.59 ^{+1.04} _{-2.87}
M_{bol}	1.36 ^{+0.12} _{-0.10}	1.37 ^{+0.12} _{-0.10}	5.64 ^{+0.11} _{-0.12}	4.63 ^{+0.11} _{-0.06}	3.12 ^{+0.21} _{-0.06}	1.39 ^{+0.15} _{-0.05}
M_V	1.39 ^{+0.08} _{-0.06}	1.40 ^{+0.08} _{-0.06}	5.79 ^{+0.16} _{-0.15}	4.67 ^{+0.12} _{-0.06}	3.25 ^{+0.26} _{-0.07}	1.72 ^{+0.17} _{-0.05}
$\log g$ [dex]	4.116 ^{+0.003} _{-0.003}	4.118 ^{+0.003} _{-0.003}	4.595 ^{+0.006} _{-0.006}	4.421 ^{+0.011} _{-0.012}	3.738 ^{+0.020} _{-0.021}	2.835 ^{+0.029} _{-0.025}
Global system parameters						
$\log(\text{age})$ [dex]	8.768 ^{+0.030} _{-0.059}			9.756 ^{+0.081} _{-0.041}		
$[M/H]$ [dex]	-0.021 ^{+0.175} _{-0.112}			-0.262 ^{+0.128} _{-0.122}		
$E(B - V)$ [mag]	0.093 ^{+0.027} _{-0.022}			0.110 ^{+0.032} _{-0.032}		
extra light ℓ_4 [in TESS-band]	0.023 ^{+0.006} _{-0.007}			0.038 ^{+0.017} _{-0.016}		
$(M_V)_{\text{tot}}$	0.63 ^{+0.08} _{-0.06}			1.42 ^{+0.20} _{-0.04}		
distance [pc]	942 ⁺¹² ₋₁₃			2561 ⁺⁷⁷ ₋₁₀₂		

Despite the fact that TESS observed only one set of third-body events, the parameters of the outer orbit can be determined robustly not only due to the archival observations which provide the outer orbital period (P_{out}), but also because of the very high quality ETV data (Fig. 11). In this regard, we note that the ground-based follow up eclipse times were found to be very helpful in excluding some possible alternative outer periods.

Turning to the astrophysical implications of the photodynamical results (see last columns of Table 6), we found that the

system consists of nearly identical triplet stars. The masses of the EB primary and the tertiary agree to within their 1- σ statistical uncertainties ($M_{\text{Aa}} = 1.17 \pm 0.03 M_\odot$ vs. $M_{\text{B}} = 1.16 \pm 0.03 M_\odot$), and the secondary of the inner EB has a lower mass by only 6 – 7% ($M_{\text{Ab}} = 1.09 \pm 0.03 M_\odot$). (Referring to the more precise relative quantities, we find: $q_{\text{in}} = 0.933 \pm 0.005$ and $q_{\text{out}} = 0.515 \pm 0.004$, respectively.) What makes this system more interesting from an astrophysical and, especially, evolutionary point of view is that the two more massive components (stars Aa and

Table 8. Orbital and astrophysical parameters of TIC 321978218 from the joint photodynamical light curve, ETV, SED and PARSEC isochrone solution.

TIC 321978218			
Orbital elements			
	Subsystem		
	Aa–Ab	A–B	AB–C
t_0 [BJD - 2400000]		58354.0	
P [days]	$0.570267^{+0.000041}_{-0.000025}$	$57.53549^{+0.00020}_{-0.00020}$	4395^{+52}_{-84}
a [R_\odot]	$3.473^{+0.009}_{-0.011}$	$92.46^{+0.36}_{-0.37}$	1691^{+18}_{-19}
e	$0.00100^{+0.00043}_{-0.00027}$	$0.2583^{+0.0016}_{-0.0016}$	$0.374^{+0.049}_{-0.033}$
ω [deg]	140^{+22}_{-53}	$122.56^{+0.28}_{-0.27}$	$68.9^{+3.1}_{-4.3}$
i [deg]	$87.96^{+0.37}_{-1.02}$	$90.000^{+0.089}_{-0.069}$	$95.5^{+9.2}_{-6.6}$
$\mathcal{T}_0^{\text{inf/sup}}$ [BJD - 2400000]	$58354.2542^{+0.0002}_{-0.0003}$	$59072.6568^{+0.0033*}_{-0.0031}$...
τ [BJD - 2400000]	$58354.061^{+0.003}_{-0.077}$	$59018.153^{+0.031}_{-0.071}$	56799^{+13}_{-24}
Ω [deg]	0.0	$0.06^{+0.79}_{-0.57}$	$-2.2^{+7.3}_{-7.2}$
$(i_{\text{mut}})_{\text{A-AB,A-C}}$ [deg]		$2.17^{+1.08}_{-0.40}$	$11.3^{+7.0}_{-5.4}$
$(i_{\text{mut}})_{\text{AB-C}}$ [deg]	...		$9.9^{+6.5}_{-4.9}$
ϖ^{dyn} [deg]	320^{+22}_{-53}	$302.53^{+0.29}_{-0.30}$	$249.2^{+3.1}_{-4.4}$
i^{dyn} [deg]	$5.7^{+3.3}_{-2.4}$	$4.2^{+2.8}_{-2.1}$	$5.7^{+3.7}_{-2.9}$
Ω^{dyn} [deg]	350^{+54}_{-33}	338^{+68}_{-62}	159^{+68}_{-57}
i_{inv} [deg]		$92.3^{+4.0}_{-2.8}$	
Ω_{inv} [deg]		$-0.9^{+3.3}_{-3.2}$	
mass ratio [$q = M_{\text{sec}}/M_{\text{pri}}$]	$0.782^{+0.018}_{-0.015}$	$0.853^{+0.008}_{-0.007}$	$0.052^{+0.006}_{-0.005}$
K_{pri} [km s^{-1}]	$135.10^{+1.54}_{-1.21}$	$38.76^{+0.34}_{-0.31}$	$1.02^{+0.11}_{-0.10}$
K_{sec} [km s^{-1}]	$172.85^{+1.79}_{-2.15}$	$45.42^{+0.09}_{-0.10}$	$19.80^{+0.49}_{-0.53}$
V_γ [km s^{-1}]		$1.707^{+0.044}_{-0.045}$	
Apsidal and nodal motion related parameters			
P_{apse} [year]	$0.88^{+0.05}_{-0.07}$	$526.9^{+2.4}_{-2.6}$	1004^{+1138}_{-84}
$P_{\text{apse}}^{\text{dyn}}$ [year]	$0.86^{+0.05}_{-0.07}$	$35.81^{+0.14}_{-0.15}$	$38.43^{+0.19}_{-0.18}$
$P_{\text{node}}^{\text{dyn}}$ [year]		$38.28^{+0.23}_{-0.22}$	
$\Delta\omega_{3b}$ [arcsec/cycle]	$101.25^{+0.49}_{-0.54}$	5700^{+25}_{-22}	405544^{+6085}_{-7670}
$\Delta\omega_{\text{GR}}$ [arcsec/cycle]	$4.111^{+0.022}_{-0.026}$	$0.307^{+0.002}_{-0.003}$	$0.0192^{+0.0008}_{-0.0006}$
$\Delta\omega_{\text{tide}}$ [arcsec/cycle]	2251^{+197}_{-119}	$0.450^{+0.038}_{-0.025}$	$0.0016^{+0.0001}_{-0.0001}$
Stellar parameters			
	Aa	Ab	B
Relative quantities			
fractional radius [R/a]	$0.2888^{+0.0041}_{-0.0035}$	$0.2370^{+0.0055}_{-0.0027}$	$0.0211^{+0.0003}_{-0.0003}$
temperature relative to $(T_{\text{eff}})_{\text{Aa}}$	1	$0.8522^{+0.0075}_{-0.0073}$	$1.2755^{+0.0095}_{-0.0093}$
fractional flux [in TESS-band]	$0.0764^{+0.0019}_{-0.0019}$	$0.0252^{+0.0012}_{-0.0011}$	$0.6998^{+0.0169}_{-0.0199}$
fractional flux [in SWASP-band]	$0.0672^{+0.0030}_{-0.0032}$	$0.0169^{+0.0013}_{-0.0013}$	$0.8795^{+0.0254}_{-0.0403}$
Physical quantities			
M [M_\odot]	$0.970^{+0.013}_{-0.018}$	$0.757^{+0.009}_{-0.006}$	$1.473^{+0.025}_{-0.023}$
R [R_\odot]	$1.003^{+0.014}_{-0.013}$	$0.824^{+0.017}_{-0.009}$	$1.949^{+0.027}_{-0.031}$
T_{eff} [K]	4969^{+83}_{-48}	4242^{+63}_{-53}	6326^{+147}_{-59}
L_{bol} [L_\odot]	$0.553^{+0.035}_{-0.025}$	$0.198^{+0.017}_{-0.014}$	$5.46^{+0.45}_{-0.24}$
M_{bol}	$5.41^{+0.05}_{-0.07}$	$6.53^{+0.08}_{-0.09}$	$2.93^{+0.05}_{-0.09}$
M_V	$5.71^{+0.07}_{-0.11}$	$7.36^{+0.15}_{-0.15}$	$2.92^{+0.05}_{-0.09}$
$\log g$ [dex]	$4.421^{+0.009}_{-0.013}$	$4.485^{+0.011}_{-0.019}$	$4.026^{+0.011}_{-0.011}$
Global system parameters			
$\log(\text{age})$ [dex]	$7.326^{+0.030}_{-0.049}$		$7.046^{+0.024}_{-0.033}$
$[M/H]$ [dex]			$-0.003^{+0.118}_{-0.102}$
$E(B - V)$ [mag]			$0.015^{+0.032}_{-0.011}$
extra light ℓ_4 [in TESS-band]			$0.197^{+0.021}_{-0.017}$
extra light ℓ_4 [in SWASP-band]			$0.035^{+0.045}_{-0.028}$
$(M_V)_{\text{tot}}$			$2.82^{+0.05}_{-0.09}$
distance [pc]			636^{+10}_{-9}

B) are very likely at the end of their TAMS or, just at the beginning of their evolution from the MS toward the giant branch. This means that, although these stars are more massive, the slightly less massive secondary actually looks a bit hotter, though, the small difference is well within the $1\text{-}\sigma$ posterior uncertainties and, thus, looks statistically insignificant ($T_{\text{Aa}} = 6033^{+78}_{-192}$ K and

$T_{\text{B}} = 6033^{+97}_{-160}$ K vs. $T_{\text{Ab}} = 6051^{+77}_{-153}$ K). At the same time, despite the quite similar masses of the inner EB members, the radii of the EB components differ substantially, being $R_{\text{Aa}} = 1.555 \pm 0.015 R_\odot$ vs. $R_{\text{Ab}} = 1.137 \pm 0.045 R_\odot$ (or, again citing the precise fractional radii, we find $r_{\text{Aa}} = R_{\text{Aa}}/a_{\text{in}} = 0.2060 \pm 0.0018$ vs. $r_{\text{Ab}} = 0.1525 \pm 0.0025$).

Table 9. Orbital and astrophysical parameters of TICs 323486857 and 650024463 from the joint photodynamical light curve, ETV, SED and PARSEC isochrone solution.

	TIC 323486857			TIC 650024463		
	Orbital elements					
	Subsystem			Subsystem		
	Aa–Ab	A–B		Aa–Ab	A–B	
t_0 [BJD - 2400000]	58569.0			58320.0		
P [days]	$0.88502^{+0.00015}_{-0.00036}$	$41.4268^{+0.0016}_{-0.0021}$		$7.197817^{+0.000026}_{-0.000028}$	$108.7251^{+0.0013}_{-0.0013}$	
a [R_\odot]	$5.362^{+0.035}_{-0.053}$	$81.51^{+0.61}_{-0.60}$		$18.21^{+0.07}_{-0.12}$	$127.09^{+0.47}_{-0.87}$	
e	$0.0021^{+0.0012}_{-0.0009}$	$0.0066^{+0.0042}_{-0.0037}$		$0.02570^{+0.00024}_{-0.00026}$	$0.32317^{+0.00011}_{-0.00011}$	
ω [deg]	151^{+77}_{-66}	241^{+48}_{-139}		$28.83^{+0.53}_{-0.49}$	$351.28^{+0.09}_{-0.10}$	
i [deg]	$84.9^{+2.3}_{-0.4}$	$84.59^{+0.28}_{-0.45}$		$90.233^{+0.059}_{-0.055}$	$90.099^{+0.069}_{-0.090}$	
$\mathcal{T}_0^{\text{inf/sup}}$ [BJD - 2400000]	$58569.7694^{+0.0003}_{-0.0003}$	$58595.020^{+0.044}_{-0.028}$		$58330.8185^{+0.0002}_{-0.0002}$	$58642.2864^{+0.0085*}_{-0.0086}$	
τ [BJD - 2400000]	$58569.47^{+0.20}_{-0.16}$	58577^{+17}_{-20}		$58325.9422^{+0.0100}_{-0.0096}$	$58623.745^{+0.025}_{-0.024}$	
Ω [deg]	0.0	$1.9^{+1.2}_{-2.5}$		0.0	$0.33^{+0.30}_{-0.26}$	
i_{mut} [deg]		$2.3^{+1.2}_{-0.7}$			$0.37^{+0.31}_{-0.22}$	
ϖ^{dyn} [deg]	339^{+73}_{-70}	76^{+47}_{-142}		$208.83^{+0.53}_{-0.49}$	$171.28^{+0.09}_{-0.10}$	
i^{dyn} [deg]	$2.05^{+1.07}_{-0.60}$	$0.28^{+0.14}_{-0.08}$		$0.30^{+0.24}_{-0.18}$	$0.07^{+0.06}_{-0.04}$	
Ω^{dyn} [deg]	98^{+27}_{-37}	285^{+90}_{-20}		112^{+23}_{-12}	292^{+23}_{-12}	
i_{inv} [deg]		$84.68^{+0.41}_{-0.47}$			$90.125^{+0.057}_{-0.068}$	
Ω_{inv} [deg]		$1.7^{+1.0}_{-2.2}$			$0.27^{+0.24}_{-0.21}$	
mass ratio [$q = M_{\text{sec}}/M_{\text{pri}}$]	$0.877^{+0.028}_{-0.021}$	$0.606^{+0.008}_{-0.014}$		$0.780^{+0.004}_{-0.003}$	$0.490^{+0.004}_{-0.004}$	
K_{pri} [km s^{-1}]	$142.41^{+3.21}_{-2.07}$	$37.44^{+0.29}_{-0.39}$		$56.12^{+0.26}_{-0.30}$	$20.55^{+0.14}_{-0.16}$	
K_{sec} [km s^{-1}]	$162.74^{+1.82}_{-2.52}$	$61.80^{+0.39}_{-0.75}$		$71.93^{+0.30}_{-0.50}$	$41.94^{+0.16}_{-0.28}$	
Apsidal and nodal motion related parameters						
P_{apse} [year]	$0.58^{+0.15}_{-0.05}$	$139.0^{+1.5}_{-1.0}$		$15.45^{+0.08}_{-0.08}$	$62.93^{+0.08}_{-0.09}$	
$P_{\text{apse}}^{\text{dyn}}$ [year]	$0.56^{+0.14}_{-0.04}$	$14.80^{+0.14}_{-0.07}$		$6.87^{+0.03}_{-0.03}$	$10.34^{+0.03}_{-0.03}$	
$P_{\text{node}}^{\text{dyn}}$ [year]		$16.56^{+0.10}_{-0.19}$			$12.38^{+0.04}_{-0.05}$	
$\Delta\omega_{3b}$ [arcsec/cycle]	$356.5^{+2.2}_{-4.2}$	9917^{+50}_{-94}		3716^{+15}_{-17}	37300^{+102}_{-109}	
$\Delta\omega_{\text{GR}}$ [arcsec/cycle]	$4.068^{+0.053}_{-0.077}$	$0.429^{+0.007}_{-0.006}$		$0.710^{+0.006}_{-0.009}$	$0.169^{+0.001}_{-0.002}$	
$\Delta\omega_{\text{tide}}$ [arcsec/cycle]	5243^{+481}_{-1121}	$12.6^{+5.0}_{-3.2}$		$0.378^{+0.025}_{-0.024}$	$0.0014^{+0.0001}_{-0.0001}$	
Stellar parameters						
	Aa	Ab	B	Aa	Ab	B
Relative quantities						
fractional radius [R/a]	$0.3479^{+0.0092}_{-0.0155}$	$0.2514^{+0.0181}_{-0.0098}$	$0.0925^{+0.0083}_{-0.0049}$	$0.0531^{+0.0009}_{-0.0008}$	$0.0369^{+0.0002}_{-0.0003}$	$0.00593^{+0.00006}_{-0.00006}$
temperature relative to (T_{eff}) _{Aa}	1	$0.9816^{+0.0109}_{-0.0066}$	$0.7741^{+0.0145}_{-0.0128}$	1	$0.8104^{+0.0041}_{-0.0038}$	$0.8998^{+0.0063}_{-0.0067}$
fractional flux [in TESS-band]	$0.0972^{+0.0071}_{-0.0080}$	$0.0496^{+0.0050}_{-0.0035}$	$0.6820^{+0.0569}_{-0.0609}$	$0.1013^{+0.0029}_{-0.0028}$	$0.0207^{+0.0008}_{-0.0007}$	$0.0411^{+0.0021}_{-0.0020}$
Physical quantities						
M [M_\odot]	$1.408^{+0.021}_{-0.043}$	$1.223^{+0.052}_{-0.028}$	$1.588^{+0.050}_{-0.038}$	$0.877^{+0.012}_{-0.018}$	$0.684^{+0.008}_{-0.014}$	$0.765^{+0.010}_{-0.017}$
R [R_\odot]	$1.873^{+0.046}_{-0.105}$	$1.344^{+0.0110}_{-0.057}$	$7.541^{+0.758}_{-0.455}$	$0.967^{+0.015}_{-0.015}$	$0.673^{+0.009}_{-0.009}$	$0.754^{+0.008}_{-0.011}$
T_{eff} [K]	6550^{+61}_{-44}	6434^{+85}_{-60}	5068^{+76}_{-71}	5682^{+28}_{-21}	4608^{+31}_{-31}	5114^{+43}_{-39}
L_{bol} [L_\odot]	$5.80^{+0.34}_{-0.69}$	$2.78^{+0.64}_{-0.32}$	$33.51^{+5.16}_{-2.44}$	$0.877^{+0.021}_{-0.020}$	$0.182^{+0.006}_{-0.005}$	$0.349^{+0.015}_{-0.015}$
M_{bol}	$2.86^{+0.14}_{-0.06}$	$3.66^{+0.13}_{-0.23}$	$0.96^{+0.08}_{-0.16}$	$4.91^{+0.03}_{-0.03}$	$6.62^{+0.03}_{-0.03}$	$5.91^{+0.05}_{-0.04}$
M_V	$2.84^{+0.14}_{-0.06}$	$3.65^{+0.13}_{-0.23}$	$1.22^{+0.10}_{-0.15}$	$4.99^{+0.03}_{-0.03}$	$7.14^{+0.05}_{-0.05}$	$6.15^{+0.06}_{-0.06}$
$\log g$ [dex]	$4.043^{+0.036}_{-0.019}$	$4.267^{+0.028}_{-0.050}$	$2.882^{+0.049}_{-0.067}$	$4.409^{+0.014}_{-0.015}$	$4.617^{+0.004}_{-0.003}$	$4.566^{+0.006}_{-0.006}$
Global system parameters						
$\log(\text{age})$ [dex]		$9.374^{+0.013}_{-0.038}$			$10.001^{+0.039}_{-0.033}$	
$[M/H]$ [dex]		$0.015^{+0.018}_{-0.058}$			$-0.107^{+0.036}_{-0.055}$	
$E(B - V)$ [mag]		$0.340^{+0.020}_{-0.020}$			0.088	
extra light ℓ_4 [in TESS-band]		$0.172^{+0.064}_{-0.063}$			$0.837^{+0.003}_{-0.003}$	
$(M_V)_{\text{tot}}$		$0.93^{+0.07}_{-0.15}$			$4.56^{+0.01}_{-0.01}$	
distance [pc]		1434^{+123}_{-74}			1126	

These results emphasize that a more robust and precise determination of the stellar masses with the addition of RV observations would be very important, since the inner EB of this triple may be used to strongly constrain stellar evolutionary models. Moreover, another aspect that should be considered is that, because of the nearly equal surface brightnesses of the primary and secondary components of the inner circular EB, one can assume that due to the total eclipses, the secondary-to-primary eclipse depth ratio is dominated by the limb darkening law of the binary components. Therefore, in order to obtain a better characteriza-

tion of limb darkening law(s) – a recently intensively investigated area, having crucial importance in the precision analysis of transiting exoplanets, or even of eclipsing binaries (see e.g. Csizmadia et al. 2013; Maxted 2023) – high-precision photometric observations with good time resolution of future regular (binary) eclipses would also be very useful.

Turning to the dynamical properties of the triple, the period ratio $P_{\text{out}}/P_{\text{in}} = 27.9$ indicates that TIC 176713425 is a moderately tight system, where one can expect the effects of significant third-body perturbations. This can be seen nicely in

Table 10. Derived ephemerides for the seven triple systems to be used for planning future observations.

TIC ID	133771812	176713425	185615681	287756035	321978218	323486857	650024463
	Inner binary						
P	12.36949	1.898728	2.3185738	2.0814225	0.5698104	0.883992	7.1971
	12.36844		2.3185448				7.1969
\mathcal{T}_0	60 035.027	60 317.664	60 055.382	60 127.070	60 434.640	60 150.345	60 252.278
	60 020.719		60 056.539				60 248.733
\mathcal{A}_{ETV}	0.030	0.006	0.0007	0.0025	0.0013	0.0008	0.028
D	0.322	0.228	0.269	0.283	0.085	0.168	0.307
	Wide binary (third body eclipses)						
P	242.3	52.55	55.84	367.64	57.52	41.356	107.95
$\mathcal{T}_0^{\text{inf}}$	58 600.1:	(58762.2:)	58 547.5	59 311.55	59 095.85	58 595.02	59 579.5
D^{inf}	6.5	6.3:	1.45	4.21	1.01	1.29	2.70
$\mathcal{T}_0^{\text{sup}}$	58 510.4	58 740.1	(58 572.9)	59 470.28:	59 072.45	(58 615.71)	59 503.8
D^{sup}	6.3	0.89	1.90	3.90:	0.68	1.27	3.18

Notes. (a) For the inner binaries: P , \mathcal{T}_0 , \mathcal{A}_{ETV} , D are the period, reference time of a primary minimum, half-amplitude of the ETV curve, and the full duration of an eclipse, respectively. \mathcal{T}_0 is given in BJD $- 2\,400\,000$, while the other quantities are in days. For all those triples where the inner eccentricities are very small and, hence, the shifts of the secondary eclipses relative to phase 0.5 are negligible (quantitatively, they are much smaller than the full durations of the individual eclipses), the same reference times and periods can be used to predict the times of the secondary eclipses. In the case of the three eccentric EBs we give a separate period and reference time for the secondary eclipses, listing them below the primary ephemerides. (b) For the outer orbits we give separate reference times for the third body eclipses around the inferior and superior conjunctions of the tertiary component. The eclipse durations, D , of the third-body eclipses do not give the extent of any specific third body events. Rather D represents the time difference corresponding to the very first and last moments around a given third-body conjunction when the first/last contact of a third-body event may occur. Double dots (:) call attention to the less certain superior/inferior conjunction times at those types of third-body events (i.e., primary vs. secondary outer eclipses) because they were not observed by TESS. Conjunction data, in parentheses, indicate that only very shallow third-body eclipses may occur which can hardly be observed with ground-based instruments.

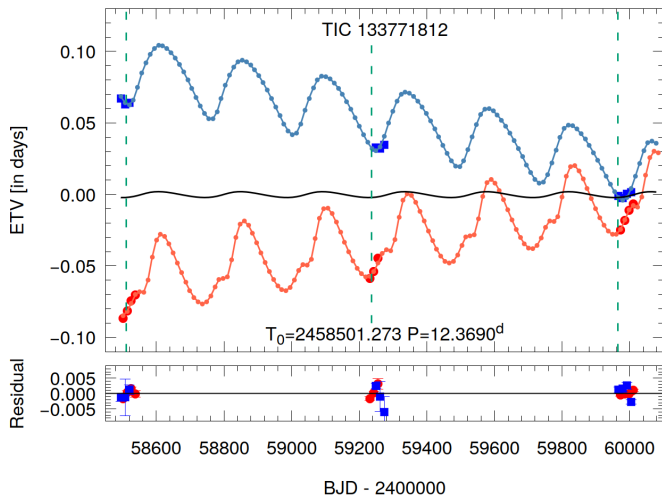


Fig. 10. TESS primary and secondary ETV curves (red and blue circles, respectively), with the best-fit photodynamical solution for TIC 133771812 (see Sect. 6). The horizontally centered black curve represents the pure LTTE contribution. Vertical lines mark the times of the observed outer eclipses (dashed green—the binary occulting the tertiary star).

the ETV curve, where the dynamical delays strongly dominate over the pure, geometric LTTE. On the other hand, however, due to the small physical size of the inner binary (and, hence, the significant fractional radii of stars Aa, Ab) the tidal effects are non-negligible and the tidally forced nominal¹¹ apsidal ad-

¹¹ We say 'nominal' because, due to the nearly circular shape of the inner orbit, one cannot really expect observable apsidal motion.

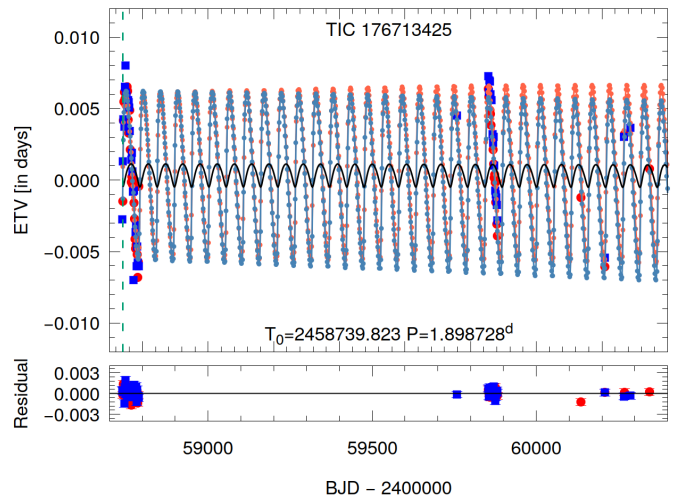


Fig. 11. ETV curves formed from the TESS and ground-based follow up observations with the best-fit photodynamical solution for TIC 176713425. The horizontally centered black curve represents the pure LTTE contribution. Dashed vertical green line marks the position of the only (two-dipped) third-body eclipse event which was observed with TESS.

vance rate in the inner EB is of the same order as the dynamically forced one ($\Delta\omega_{\text{in}}^{\text{tide}} = 387'' \pm 15'' \text{ cycle}^{-1}$ vs. $\Delta\omega_{\text{in}}^{\text{3b}} = 1230'' \pm 15'' \text{ cycle}^{-1}$).

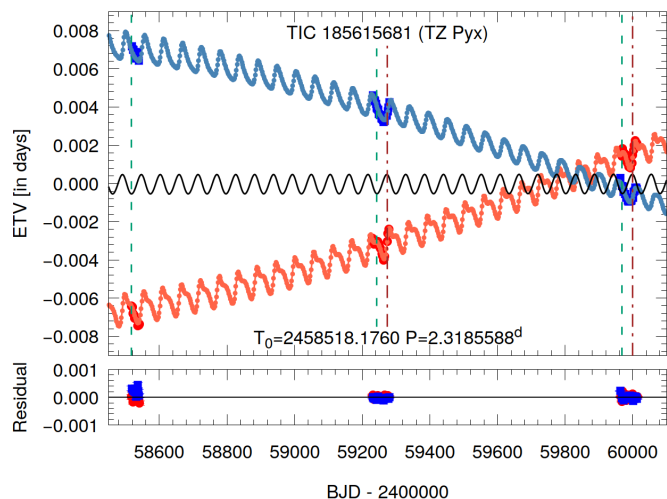


Fig. 12. TESS ETV curves with the best-fitted photodynamical solution for TIC 185615681 (TZ Pyx). The horizontally centered black curve represents the pure LTTE contribution. Vertical dashed green lines represent the times of the observed outer eclipses when the binary occults the tertiary star, and vice versa for the dot-dashed red lines.

7.2.3. TIC 185615681 = TZ Pyx

This is the only system in our current sample of triples where the inner EB has been known already for a long time. The variability of the system was discovered by Strohmeier (1966). Duerbeck & Rucinski (2007) obtained and analyzed 8 RV points for each of the two stellar components of the EB. They found that the inner EB consists of two very similar stars (quantitatively, they found a spectroscopic mass ratio of $q^{\text{spec}} = 0.996 \pm 0.020$) that are hot and likely of late A spectral type. These authors, however, did not take note of the slight eccentricity of the binary’s orbit. It was Otero (2007) who reported for the first time not only the binary eccentricity, but also evidence for the apsidal motion in the EB. This effect was then studied first by Zasche (2012) who, with the use of 16 badly scattered ground-based eclipse times (spanning an interval of ~ 7000 days), determined an apsidal motion period of $P_{\text{apse}} = 157 \pm 37$ yr. But, as they note: “The apsidal motion fit is still not very convincing and would have even shorter period [...], but only further observations would confirm this hypothesis.” From this apsidal motion period they inferred that the (mean) apsidal motion or, internal structure constant, k_2 , is in accord with the theoretically expected value. Naturally, they were not aware of the presence of the third stellar component in the system, whose perturbations, as our analysis clearly reveals, completely dominates over the tidal effects. Hence, even if their apsidal motion period had been correct, it would not be conclusive in regard to the internal structure constants of the stars. Most recently Kim et al. (2018) repeated the ETV analysis, using the then available 20 data points, and got a much shorter apsidal motion period of $P_{\text{apse}} = 22.89 \pm 0.30$ yr, which is much closer to our findings.

Turning to our analysis of the available former ground-based observational material, we used only the RV data of Duerbeck & Rucinski (2007). Neither ground-based light curves, nor ETV data were used for our photodynamical runs. While neglecting the ground-based light curve data is well justifiable given the availability of the far superior TESS light curves, the ETV points, in theory, might be usable to obtain a more precise detection of the apsidal motion period. Unfortunately, however, the

historical ETV data have such bad scatter that, from our perspective, these are unusable to mine out any additional information.

The twin components of TZ Pyx ($M_{\text{Aa}} = 2.013 \pm 0.034 M_{\odot}$; $M_{\text{Ab}} = 2.008 \pm 0.033 M_{\odot}$) are the hottest, fully radiative stars in our sample. Moreover, this is the only triple in our sample, where the third, outer component is substantially less massive ($M_{\text{B}} = 0.888 \pm 0.014 M_{\odot}$) than either of the binary members. (Referring again to the more precise relative quantities, we find: $q_{\text{in}} = 0.998 \pm 0.002$ and $q_{\text{out}} = 0.221 \pm 0.003$, respectively.) In such a way, the contribution of the third component to the total system flux is negligibly small, only $\sim 1\%$. On the other hand, the depths of the primary third-body eclipses may reach $\sim 6 - 8\%$, where, for such a relatively bright ($V = 10.7$) variable star, such extra dips would be serendipitously detectable even with sub-metre size ground-based telescopes. Despite this fact, no indications of the triple nature of this system have been previously reported. This fact emphasizes that one should not be surprised to occasionally find a triply eclipsing tertiary hidden even amongst the best observed and brightest EBs.

Regarding the orbital properties, we found a small, but significant, eccentricity for the inner orbit, being $e_{\text{in}} = 0.01067 \pm 0.00009$. This value agrees well with the results of Kim et al. (2018) who obtained $e_{\text{in}} = 0.01068 \pm 0.00008$.¹² The outer orbit was also found to be slightly eccentric with $e_{\text{out}} = 0.0982 \pm 0.0008$. This is the second lowest outer eccentricity in our current sample.

Despite the moderately tight nature of the triple system ($P_{\text{out}}/P_{\text{in}} = 24.2$) the full-amplitudes of the primary and secondary ETVs, on the P_{out} -timescale, remain under 1.5 min (~ 0.001 d). This effect is hardly detectable with incidental, highly inhomogeneous eclipse times measured with ground-based photometry. The ETVs, determined from the precise TESS photometry, however, clearly show the presence of typical, third-body induced dynamical ETVs (see Fig. 12). Our solution reveals that the ETVs on this timescale are nearly equally contributed by the third-body perturbations and the geometric LTTE.

On a longer timescale, however, the main effect seen in the ETV curves is due to apsidal motion. In turn, the third-body-driven apsidal motion dominates over the classic tidal component, but the latter contribution is non-negligible ($\Delta\omega_{\text{in}}^{\text{3b}} = 738'' \pm 5'' \text{ cycle}^{-1}$ vs. $\Delta\omega_{\text{in}}^{\text{tide}} = 144'' \pm 2'' \text{ cycle}^{-1}$). In this regard, we note that even though three inner eccentric EBs of the current sample of seven systems exhibit well observed apsidal motion, TZ Pyx is the only one where the classic tidal effects are important. Hence, this is the only system in our sample where the proper settings of the internal structure constants have real significance. Therefore, we set the first two apsidal motion constants to $k_2 = 0.005$ and $k_3 = 0.001$ for both members of the inner EB, in accord with the recent tables of Claret (2023). Taking into account all three different contributions of the apsidal motion (though the relativistic contribution was found to be much smaller than the other two, with $\Delta\omega_{\text{in}}^{\text{GR}} = 2''83 \pm 0''04 \text{ cycle}^{-1}$) our solution gives a theoretical apsidal motion period of $P_{\text{apse}}^{\text{theo}} = 18.2 \pm 0.2$ yr.

7.2.4. TIC 287756035

This system has, by far, the longest of the outer periods among this current set of seven triply eclipsing triples at 368 days. In fact, this outer period is so close to that of an Earth year, that we

¹² One should keep in mind, however, that the two values cannot be perfectly compared, as our orbital elements are instantaneous osculating elements, while the ones listed in the Kim et al. (2018) paper are some kind of average elements, deduced from the observations.

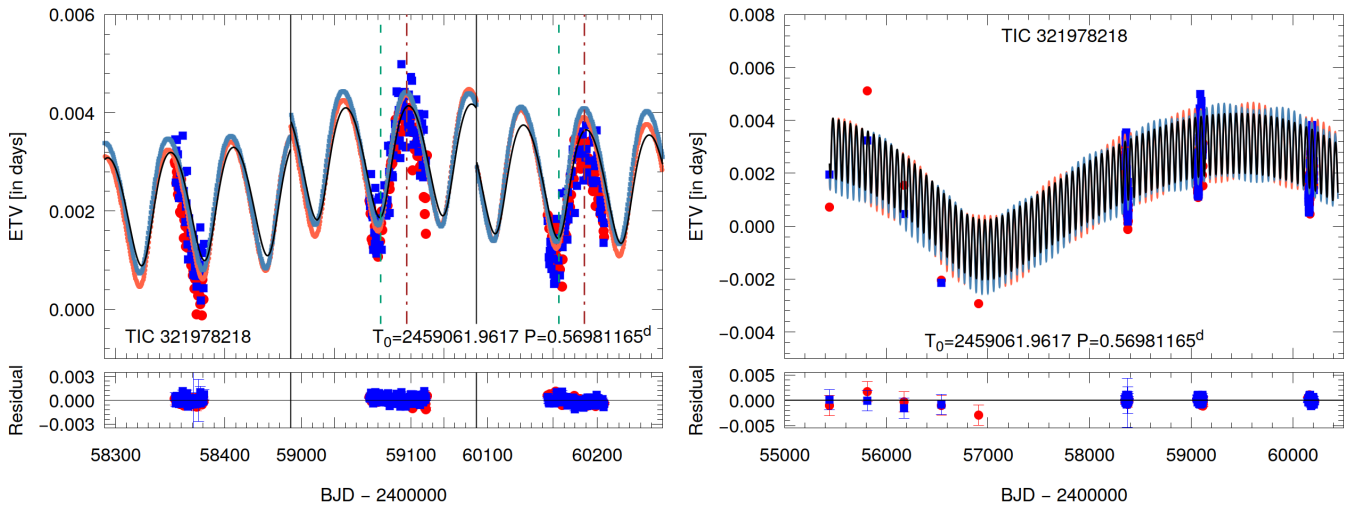


Fig. 13. ETV curves for TIC 321978218 with the best-fit photodynamical solution superposed. *Left panel:* ETV curve derived from TESS data only. We note that only those sections of the ETV curves, where TESS data are available, are shown. Vertical black lines denote the different sector boundaries; dashed green lines represent the times of the observed outer eclipses when the binary occults the tertiary star, and vice versa for the dot-dashed red lines. *Right panel:* Overall ETV curve after adding average ‘seasonal’ ETV points (see text for explanation) calculated from SWASP observations. The longer-term ETV curve also nicely shows an additional variation. We model it with a fourth stellar component, making the system a 2+1+1 quadruple. See text for details.

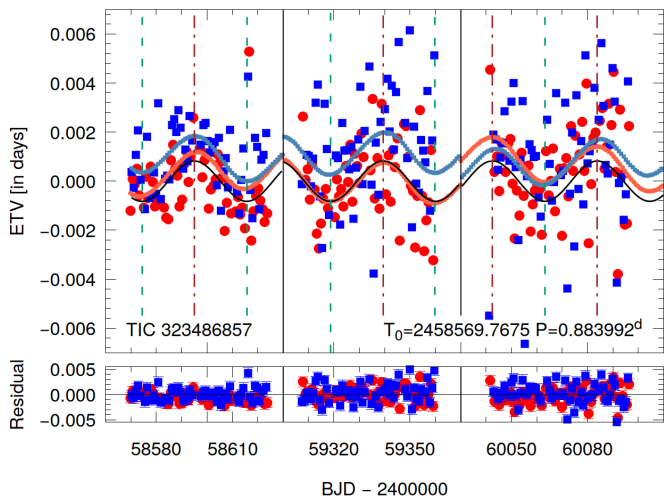


Fig. 14. TESS ETV curves with the best-fit photodynamical solution for TIC 323486857. We note that only those sections of the ETV curves, where TESS ETV data are available, are shown. Vertical lines have the same meaning as in Fig. 13.

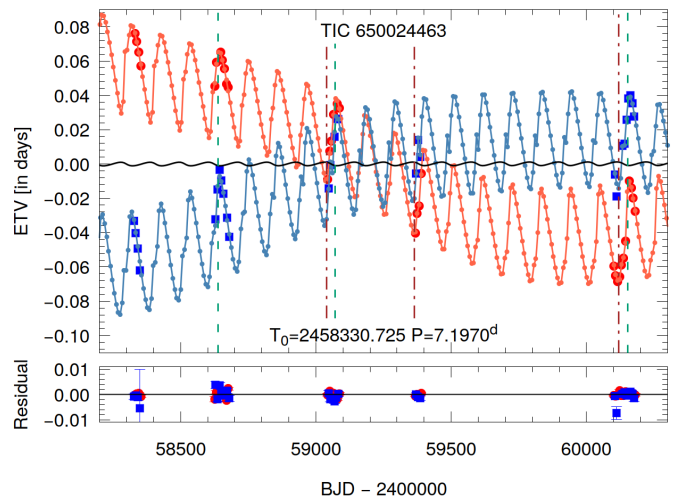


Fig. 15. TESS ETV curves with the best-fitted photodynamical solution for TIC 650024463. The horizontally centered black curve represents the pure LTTE contribution. Vertical lines have the same meaning as in Fig. 13.

were able to see only $\sim 3/4$ of the phases in the outer orbital fold of the archival data (see left panel, middle row of Fig. 9). The system is quite flat with the inner and outer orbital inclinations near 89° and a mutual inclination angle of $i_{\text{mut}} = 1.4^\circ$.

The outer orbit has a quite typical eccentricity for these systems of $e_{\text{out}} = 0.23 \pm 0.02$, while the observable argument of the outer periastron was found to be $\omega_{\text{out}} = 53.7 \pm 0.7$. One should keep in mind, however, that both TESS and the formerly mentioned ground-based surveys observed only one type of third-body eclipse, namely, those where the tertiary star occulted the inner binary. Therefore we are not able to constrain the quantity $e_{\text{out}} \cos \omega_{\text{out}}$ through the offset of the other type of third-body eclipse from an orbital phase of 0.5 . In addition to this fact, due to the lack of any usable ETV curve (which would offer additional constraints on e_{out} and ω_{out}), our primary source for information

about e_{out} and ω_{out} is only the poorly covered RV curve of the tertiary (see Fig. 17). Thus, the obtained e_{out} and ω_{out} values are less robust than in the case of the other systems studied in this work.

One can, however, make, an indirect, inverse check on the reliability of the obtained outer eccentricity and argument of periastron values. Our photodynamical solution (of which $e_{\text{out}} \cos \omega_{\text{out}}$ was a direct, adjustable parameter) resulted in a median posterior of $e_{\text{out}} \cos \omega_{\text{out}} = 0.14 \pm 0.01$. Taking into account that the phase of the superior conjunction relative to the inferior conjunction can be approximated as $\phi_{\text{sup}} \simeq \frac{1}{2} - \frac{2}{\pi} e \cos \omega$ (see, e.g., Sterne 1939), one can calculate that the other type of third-body eclipse should occur around phase 0.411 ± 0.007 . Taking a look at the archival folded light curve of TIC 287756035 (Fig. 9),

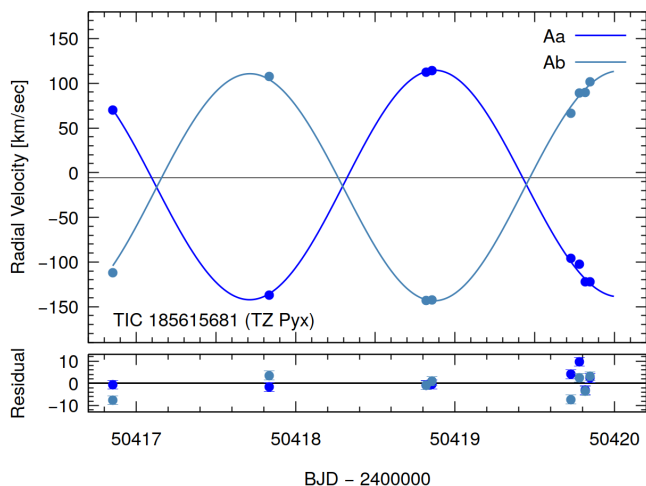


Fig. 16. RV curves and model fits for TIC 185615681. The thin, horizontal line at $V = -5.95 \text{ km s}^{-1}$ represents the systemic radial velocity of the triple star system. If TIC 185615681 were a single binary, the RVs of the two components would intersect each other exactly on that line. The different offsets of consecutive intersections of the RV curves from this line is due to the revolution of the inner pair around the center of mass of the whole triple system. The RV points were taken from Duerbeck & Rucinski (2007).

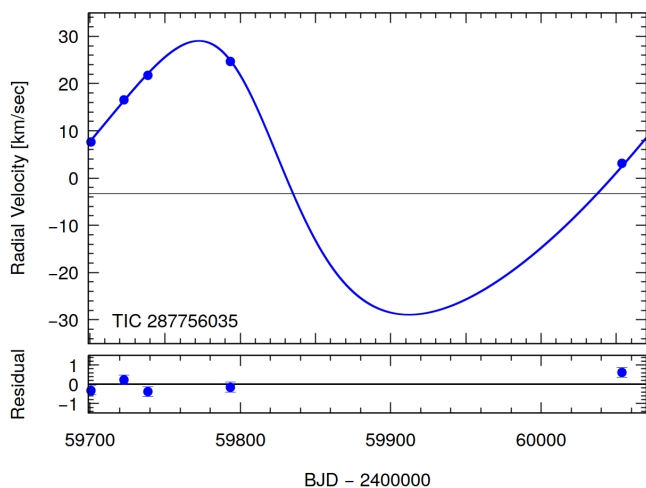


Fig. 17. RV curve and model fit for the third component of TIC 287756035. The thin, horizontal line at $V = -3.9 \text{ km s}^{-1}$ represents the systemic radial velocity of the triple star system.

one can see that this phase value is very close to the left edge of the seasonal gap of the observations, but the target was definitely observable during this orbital phase. Despite this, no dip can be noticed in the fold around that phase. One should keep in mind, however, that this phase is very close to the beginning of the seasonal gaps, and one may expect that the target was observable only for a short time just after sunset and hence, only observations reduced in number and quality are available during these intervals. Another possibility might be that, due to the weaker constraints on $e_{\text{out}} \cos \omega_{\text{out}}$, the obtained posteriors might have larger statistical uncertainties than we found. Thus, further RV observations would be very important to clarify this question.

Apart from this issue discussed above, what makes this system very interesting from an astrophysical point of view is that the two more massive stellar components, with very similar

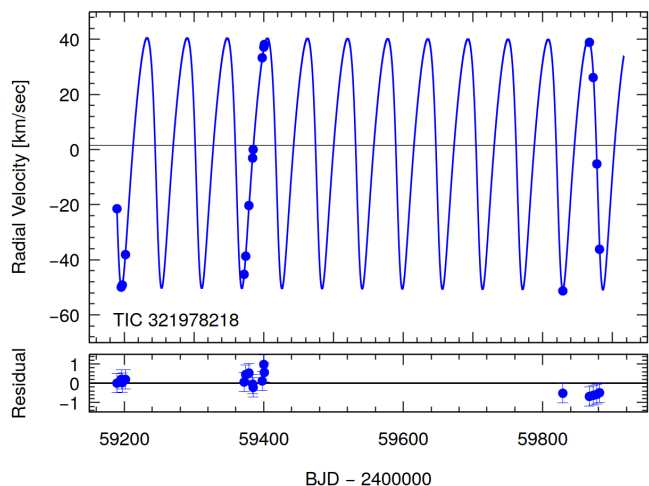


Fig. 18. RV curve and model fit for the third component of TIC 321978218. The thin, horizontal line at $V = 1.6 \text{ km s}^{-1}$ represents the systemic radial velocity of the quadruple star system.

masses of $M_B = 1.133 \pm 0.04 M_{\odot}$ and $M_{Ab} = 1.116 \pm 0.04 M_{\odot}$, are evolved to very different levels¹³. The slightly more massive tertiary is quite evolved at $R_B = 6.7 \pm 0.3 R_{\odot}$, and dominates the light of the system. On the other hand, the secondary component of the inner EB is just at the very beginning of its evolution toward the giant branch with $R_B = 2.36 \pm 0.06 R_{\odot}$. For such near solar mass stars, they must be fairly old at 5.7 Gyr in order to be ascending the giant branch. Interestingly, this shows what will become of our Sun within a short (astronomical) time. We also note that even the third, less massive star with $M_{Aa} = 0.93 \pm 0.02 M_{\odot}$ and $R_{Aa} = 0.98 \pm 0.02 R_{\odot}$ is currently located on the TAMS just before its evolution toward the giant branch. Thus, at the current epoch, this star is the hotter one and, hence, it is occulted by its more massive companion in the inner binary during the primary eclipses. Thus, we call star *Aa* the primary of the inner EB, even though it has the lower mass of the pair. It is somewhat surprising that Gaia has not yet measured the spectroscopic orbit of the tertiary given that it dominates the system light, is reasonably bright at $G = 13.5$, and has relatively narrow lines with $T_{\text{eff}} \approx 4830 \text{ K}$. Only the tertiary in TIC 323486857 is somewhat more evolved ($R \approx 7.5 R_{\odot}$) among our current set of triples.

The system is the opposite of ‘tight’ with $P_{\text{out}}/P_{\text{in}} \approx 368/2.1 \approx 175$, and therefore, given the flatness of the system and small-to-modest eccentricities for the inner and outer orbits, respectively, no large dynamical effects are expected.

Finally, we note that star *Ab*, at $R = 2.36 R_{\odot}$, is only modest underfilling its Roche lobe which is currently about $3.45 R_{\odot}$. Thus, since *Ab* is already well evolved off the main sequence it will overflow its Roche lobe relatively soon. By contrast, the tertiary star, at $R = 6.75 R_{\odot}$, underfills its Roche of $104 R_{\odot}$ by a large margin. However, since the tertiary is more evolved than star *Ab*, and therefore has a big evolutionary lead over *Ab*, it is an interesting question as to which star will first overflow its Roche lobe. It appears that the tertiary will actually grow to $104 R_{\odot}$ within 100 Myr and overflow its Roche lobe, while star *Ab* will

¹³ M_B is only $0.017 M_{\odot}$ greater than M_{Ab} , but is within $1\text{-}\sigma$ of being equal. However, M_B could be as much as $0.14 M_{\odot}$ more massive at the $1.5\text{-}\sigma$ level. Also, using the more accurate mass ratios, we find that $M_{Ab}/M_B = 0.986 \pm 0.009$, which is less than unity at the $1.5\text{-}\sigma$ level.

require about 40% more time to overflow its Roche lobe in the EB.

7.2.5. TIC 321978218

TIC 321978218 has the largest archival observational material among our current sample of triples. Besides the above mentioned four seasons of SWASP observations, this target was also spectroscopically surveyed by the Radial Velocity Experiment (RAVE), and detailed spectroscopic parameters (T_{eff} , $\log g$, different abundances, etc.) were published in their data release 5 (Kunder et al. 2017). Our own spectroscopic follow up has also resulted in 17 high-quality RV points. The system was found to be single lined in the RAVE analysis, and we also found that only the lines of the tertiary component are observable. These are in nice accord with the findings of the photodynamical analysis, which shows that the system's light is largely dominated by the tertiary component. Hence, we can conclude that the quantitative spectroscopic results of RAVE basically describe the tertiary component. Consequently, the effective temperature of $T_{\text{eff}} = 5974 \pm 150$ K given in RAVE DR5 yields the effective temperature of the dominant tertiary. This result becomes especially interesting when we combine the preliminary analytic RV and ETV solutions to find an estimate for the mass of this tertiary star. A first analytic solution for the high-quality RV curve (see Fig. 18) yields a spectroscopic mass function of $f_{\text{sp}}(M_A) = 0.506 \pm 0.003 M_{\odot}$. On the other hand, the preliminary analytic LTTE ETV solution provides a mass function of $f_{\text{ETV}}(M_B) = 0.290 \pm 0.030 M_{\odot}$. Writing these out explicitly

$$f_{\text{ETV}}(M_B) = M_B \sin^3 i_{\text{out}} \left(\frac{q_{\text{out}}}{1 + q_{\text{out}}} \right)^2 \quad (1)$$

and,

$$f_{\text{sp}}(M_A) = M_A \sin^3 i_{\text{out}} \left(\frac{q_{\text{out}}^{-1}}{1 + q_{\text{out}}^{-1}} \right)^2 = M_A \sin^3 i_{\text{out}} \left(\frac{1}{1 + q_{\text{out}}} \right)^2, \quad (2)$$

one can readily see that

$$M_B \sin^3 i_{\text{out}} = f_{\text{ETV}}^{1/3} (f_{\text{ETV}}^{1/3} + f_{\text{sp}}^{1/3})^2 = 1.41 \pm 0.10 M_{\odot}. \quad (3)$$

Thus, one may immediately realize that a star with an effective temperature of $T_{\text{eff}} \approx 5900$ K and stellar mass of $m_B \approx 1.4 M_{\odot}$ cannot be a main sequence object (we would expect a range of $T_{\text{eff}} \approx 6500 - 7000$ K for this mass). This suspicion became even stronger when we made efforts to model the light curve without taking into account any astrophysical constraints, that is, by directly adjusting the fractional radii of the stars and their temperature ratios. In such a way we found a quite good fit, but the resultant $\log g$'s for the inner EB stars were found to be ~ 4.4 together temperatures of less than 5000 K. In other words, the fractional radii of the EB members¹⁴ (this latter quantity is mainly dictated by the phase-durations of the regular eclipses) were found to be too large.

After an initial consideration, these findings call to mind three plausible explanations; however, two of them can be readily refuted. First, for a main-sequence tertiary with a mass of $M_B \approx 1.8 M_{\odot}$ and corresponding effective temperature of $T_{\text{eff}} \approx 8000$ K, a consistent model can be obtained with three coeval

¹⁴ For the connection between the fractional radii and the surface gravity see, e.g., Southworth 2004; Hajdu et al. 2017.

MS stellar components, where the total mass of the inner EB is well constrained by the spectroscopic mass function. In this case, however, (i) the ETV fit becomes considerably weaker, (ii) the model cumulative SED clearly lies far above the measured catalogued SED points and, (iii) the observed spectrum is clearly inconsistent with such a hot source. Second, one can assume that the EB members are, again, main sequence stars, but they have radii that are inflated by 10-15% due to tidal interactions with each other (see, e.g., Spada et al. 2013). The problem in this case, however, is that if one assumes the tertiary is a quite evolved¹⁵ $\sim 1.4 M_{\odot}$ star, the EB components with the proper masses would be far too bright for the observed eclipse depths. This means that for relatively brighter EB components, the deeper third-body eclipses, which occur when the EB stars transit in front of the tertiary would be too shallow, while the other third-body eclipses, when the EB stars are occulted by the third tertiary star, would be too deep. Moreover, the regular EB eclipses would also be deeper than are observed.

After the above arguments, we found only one really plausible explanation for the system properties. According to our interpretation TIC 321978218 is a very young, pre-main sequence system. This assumption would explain both the low temperature of the third star relative to its mass and the large fractional radii of the less massive EB members. An additional problem, however, arises even in this pre-MS scenario. We were unable to find strictly coeval stars which would satisfy all the observational constraints. Instead we allowed a different age for the tertiary component than that of the EB members, the latter two of which were considered to be strictly coeval. As one can see in Table 8, we found satisfactory solutions with a slightly younger tertiary $t_B \approx 11$ Myr vs. $t_{Aa,Ab,C} \approx 21$ Myr. Such a small difference of ≈ 10 Myr might be comparable with even the life time of a circumbinary disk, and also may imply the operation of a sequential disk instability mechanism as a possible explanation of multiple stellar system formation (see, e.g. Tokovinin 2021, and further references therein). It may also amount to only some minor inconsistencies in the pre-main sequence stellar evolution tracks.

Having established that TIC 321978218 is a young system, we return to the interesting system structure initially introduced in Sect. 5. The securely understood part of the orbital architecture is that of a flat edge-on triple with a 0.57-day inner EB and a tertiary in a 57.5 day outer period. The mutual inclination angle is only $\sim 2^\circ$. The tertiary contains some 90% of the system bolometric luminosity.

In addition, as we found from the ETV curves in Fig. 18 there is a fairly clear additional long-term structure superposed on the ETV of the triple system itself. If we assume that this additional perturbation to the light curve is due to another body orbiting the triple farther out, we find evidence for a quadruple system with a 2+1+1 hierarchy. If this is the correct interpretation, the outer orbital period is ≈ 4400 d, the outer eccentricity is ~ 0.37 , and the mutual inclination with the inner triple is $\sim 10^\circ$.

The only astrophysical parameter associated with the fourth star that is actually constrained by the available observational material is its (very low) mass of $M_C = 0.16 M_{\odot}$. Because of its negligibly small contribution to the system's total flux, as well as the absence of any other effects on the light curve, all other parameters such as stellar radius and effective temperature remain basically undetermined. Due the consistency of the model, however, LIGHTCURVEFACTORY calculates all the astro-

¹⁵ This qualifier is necessary for $T_{\text{eff}} \approx 6000$ K in the case of such a massive star.

physical parameters of this fourth star in the same manner as for the other three components, namely, via the use of PARSEC isochrones. During all the runs, for technical reasons, the age of this fourth star was considered to be equal to the age of the inner EB system (21 Myr). The resultant effective temperature ($T_C = 2790 \pm 100$ K) follows from its mass and age. The highly bloated radius ($R_C = 0.49 \pm 0.02 R_\odot$) can be understood in the long time it takes for a star this low in mass to contract onto the main sequence. However, none of these parameters for the fourth star should be taken too seriously until the existence of the fourth star is confirmed by further observations.

7.2.6. TIC 323486857

This is another target where the TESS light curve was strongly contaminated by nearby, and likely variable, stars. Thus, we had to apply our PCA analysis again in order to separate the signal of the triply eclipsing triple system from other stars. Due to the strongly variable nature of the contaminating light, this was not a simple task and, during the process, we probably lost a significant fraction of the flux coming from our target system. Moreover, even after the PCA process, we obtained a substantially distorted light curve. We assume that this remaining signal is real, and comes from our system, revealing strong chromospheric activity in the late type stars. We made some further efforts to remove, or at least reduce, the effects of these extra distortions to the geometric triple star signal (the latter of which we are investigating), but these efforts met with only partial success. Finally, we carried out our usual complex photodynamical analysis, but simultaneous to the triple-star light-curve fitting, we also fit the extra distortions together with harmonic functions with four frequencies, as we have done previously in some other cases (see Borkovits et al. 2018, for a detailed description of this process). In such a way we were able to obtain a quite reliable solution, but the parameter uncertainties are somewhat larger than in the case of the other triple systems.

TIC 323486857 is comprised of three comparable-mass stars in highly circular inner and outer orbits that are nearly coplanar. The mutual inclination angle between these two orbits is only $2^\circ 5' \pm 1^\circ$. The tertiary star has a mass of $1.6 M_\odot$ compared to $1.4 M_\odot$ for the primary star of the inner binary. Just this small difference in mass, however, is sufficient for the tertiary star to be substantially evolved ($R_B = 7.5 R_\odot$), while the primary EB star has not evolved much.

This system has three related properties that make it rather interesting. It has a combination of (i) a very short outer orbital period (41 d), (ii) a quite low outer eccentricity (0.0066 ± 0.0040), and (iii) a fairly large tertiary fractional radius $r_B = R_B/a_{\text{out}} = 0.093 \pm 0.007$. In Fig. 19 we plot the essence of this information in the plane of $e_{\text{out}}-r_B$ for all 33 triply eclipsing triples that we have studied recently (see Sect. 8 for more information), including TIC 323486857. With the exception of the two sources at the bottom left of the plot (marked with a faint green ellipse) there is a strong inverse correlation between the outer eccentricity and the tertiary's fractional radius. We believe this is caused by dissipation in the tides raised in the evolving giants by the companion EB. The most circularized systems (with the two aforementioned exceptions) have outer orbital separations of only ~ 7 -13 times the radius of the tertiary, while the tidally induced decay of the eccentricity goes as a high power of R_B/a_{out} (Zahn 1977). This is completely analogous to the circularization process that operates in ordinary binary stars. The other two systems with low eccentricity, but relatively small values of r_B , seem other-

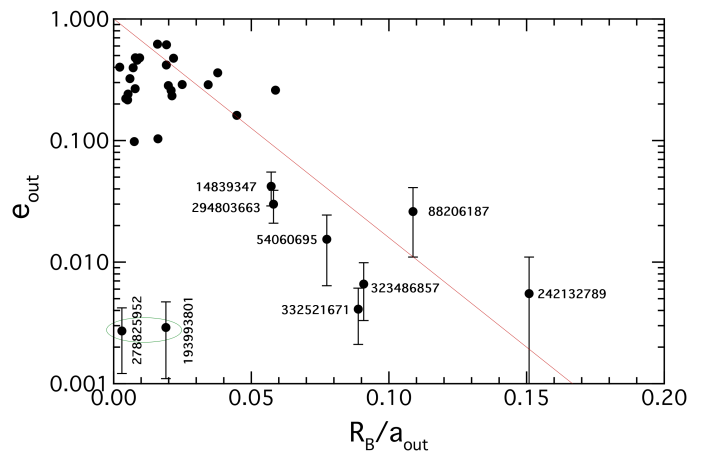


Fig. 19. Parameter e_{out} plotted against the fractional radius of the tertiary component $r_B = R_B/a_{\text{out}}$ for 33 triply eclipsing triple systems that we have studied recently (see Sect. 8 for details). The red line sketches out the inverse correlation between these two parameters, with a functional form of $e_{\text{out}} \approx \exp(-42r_B)$. Exceptions are the two systems marked with a faint green ellipse with very low eccentricities, but not large values of r_B . Numbers next to individual sources are the TIC numbers. We omit error bars on the systems with $e_{\text{out}} \geq 0.1$ for increased clarity.

wise perfectly normal systems with well measured parameters—we presume these were born circular.

7.2.7. TIC 650024463 = Gaia DR3 4618836249918572544

The stellar identification of this system is somewhat problematic. This is because, according to Gaia DR3, there are three potential candidate stars within $10''$ of each other (see Fig. 20). These are Gaia DR3 4618836249918572928 = TIC 302965294 with $G=13.28$ mag; 4618836249918572544 = TIC 650024463 with $G=14.84$ mag at $2''$ from the former target; and 4618836249918735488 = TIC 302965293 with $G=15.13$ mag, a bit farther at $9''$. The three targets have completely different DR3 parallaxes and proper motions, hence, there are no physical relations amongst them, at least not with any certainty. On the other hand, it is also clear that the images of the three stars cannot be disentangled due to the large pixel size of TESS and, naturally, the blended light curve of the three stars is totally dominated by the brightest target star.

Thus, our first assumption was that the triply eclipsing triple stellar system is hosted by the brightest stellar image, namely that it belongs to TIC 302965294. The very first light curve fitting trials, however, revealed that a consistent EB and triply eclipsing model can be obtained only with the assumption of 80 – 85% contaminated light. However, for the brightest star, TIC 302965294, it is clearly not possible that this much contaminated light comes from one of the fainter neighboring stars. On the other hand, if the triple resides in one of the fainter stars (i.e., TICs 650024463 or 302965293), then the extra light is nicely accounted for by the brightest star which does not host the triple. These two fainter stars have G_{RP} band fluxes of ≈ 0.26 and ≈ 0.19 , respectively, relative to the brightest star.

Because TIC 302965293 is $9''$ from the brightest star TIC 302965294, we carried out a photo-center analysis using the eclipses observed in the source (see, e.g., Kostov et al. 2024). The top panel of Fig. 20 shows the layout of the neighboring stars at the TESS pixel level. The bottom panel indicates the relative location of TIC 302965293 ($G=15.13$), while the red

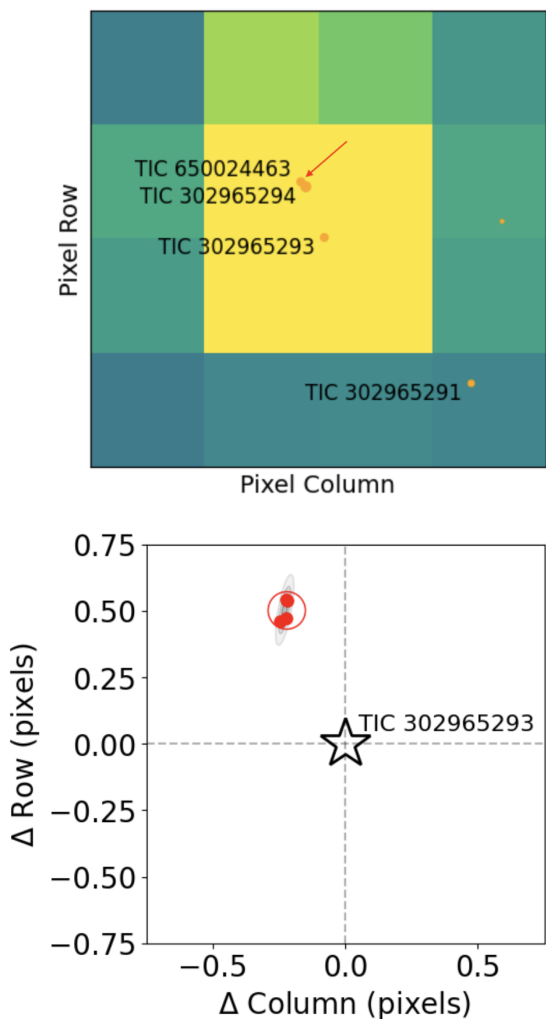


Fig. 20. Positional information for TIC 650024463 and its two neighbors. *Upper panel:* A 4×4 pixels TESS image near the position of TIC 650024463 (marked by the red arrow) from Sector 1, highlighting nearby field stars (orange dots). *Lower panel:* Photocenter measurements for the primary eclipses detected in Sector 1 compared to the relative pixel position of TIC 302965293. The small red dots represent the measurements for each eclipse (four in Sector 1); the large red circle represents the average photocenter; and the grey contours represent the corresponding 1-, 2- and 3- σ confidence intervals. As seen from the panel, the measurements clearly rule out TIC 302965293 as a potential source of the detected eclipses.

points are the photocenter locations of the primary EB eclipses in comparison. The grey contours are the confidence levels for the eclipse locations. Thus we see that TIC 302965293 is robustly ruled out as the source of the eclipses. This photo-center analysis is not quite sufficient to distinguish TIC 302965294 from TIC 650024463 because they are only $2''$ apart. However, TIC 302965294 has already been ruled out via the shallow depth of the eclipses (see above).

Thus, even though we now know that TIC 650024463 is the correct host of the triple system, due its extreme proximity to the brighter star TIC 302965294, there are no available cataloged passband magnitudes for this target – with the exception of the three Gaia DR3 magnitudes. Hence, in this case, we departed from our usual SED + PARSEC fitting procedure and simply fixed the Gaia DR3 parallax (and, hence, distance). We also set the

interstellar reddening $E(B - V)$ parameter to the value given in TIC v8.2, and kept it fixed.

Apart from the light contamination issue, the complex photodynamical analysis resulted in quite robust results for the system parameters. In particular, the orbital dynamics and 3D configuration of the entire stellar system were well determined and, moreover, the relative (dimensionless) stellar quantities (i.e. the mass, temperature and radius ratios of the stars) are also determined with high accuracies. This success is due to the fact that TESS observed the target during nine sectors (the most amongst the currently investigated seven systems). These observations recorded not only six third-body eclipses (Fig. 7), but the derived ETV curves (see in Fig. 15) show marked, large amplitude, dynamically dominated P_{out} -period cycles, and cover more than half of a full apsidal revolution cycle (the latter of which is also clearly dominated by third-body effects).

These ETV properties are consequences of the fact that this system is by far the tightest triple in our sample with $P_{\text{in}} = 7^{\text{d}}20$, $P_{\text{out}} = 108^{\text{d}}73$ and, hence, $P_{\text{out}}/P_{\text{in}} \approx 15.1$. From a dynamical perspective, this triple star system is very similar to the three triples (KIC 9714358 – $P_{\text{in}} = 6^{\text{d}}47$, $P_{\text{out}} = 104^{\text{d}}08$; KIC 5771589 – $10^{\text{d}}68$, $113^{\text{d}}87$; TIC 219885468 – $7^{\text{d}}51$, $111^{\text{d}}51$) which were recently analyzed in detail by Borkovits & Mitnyan (2023). Besides the very similar inner and outer periods, further similarities are that all of the four systems are (i) quite flat (well within $i_{\text{mut}} = 0^{\circ}5$), and have (ii) small, but significantly non-zero inner eccentricities ($0.0036 \lesssim e_{\text{in}} \lesssim 0.042$), and (iii) moderate outer ($0.16 \lesssim e_{\text{out}} \lesssim 0.39$) eccentricities.

As it was pointed out by Borkovits & Mitnyan (2023), such tight, eccentric and flat systems are ideal for observational detections of higher order third-body perturbations on timescales as short as a few years. The different apsidal motion amplitudes of the ETV curves in the first and the second half of the TESS observations of TIC 650024463 (Fig. 15) suggest the additional presence of observable effects of higher, octupole order third-body perturbations in the current system.

To further study this effect, we numerically integrated the motion of the triple system for the forthcoming few centuries. From these integrations we show and discuss some representative results for the current century. In the upper panel of Fig. 21 we plot the numerically generated ETV curve for the entire 21st century. The $P_{\text{apse}}^{\text{obs}} = 10.9$ yr-period, dynamically forced apsidal motion is readily visible from the anticorrelated nature of the primary (red) and secondary (blue) ETV curves. These variations correspond nicely to the period of revolution of the inner orbital ellipse in the observational frame of reference, that is, to the variation of the observational argument of periastron (ω_{in}) plotted with red dots in the lower left panel of Fig. 21. This period of 10.9 yr, however, is substantially shorter than the theoretical value of $P_{\text{apse}}^{\text{theo}} = 15.45 \pm 0.08$ yr (see in Table 9) which was calculated from the simple, quadrupole-order theory. This discrepancy indicates that the quadrupole-order perturbation theory may well be insufficient in the present situation.

Besides this weak, indirect indication for the presence of the higher-order perturbation effects, however, the very same ETV curve carries more clear and well observable evidence about the presence of higher order effects. As one can see in the upper panel of Fig. 21, the amplitudes of the consecutive half-apsidal motion cycles in the ETV curve are really highly variable during the entire 21st century. These amplitude variations do not correspond strictly to the apsidal motion cycles, (and hence, the amplitude varies cycle-by-cycle), but instead, correspond to the ~ 12.9 yr-period (inner) eccentricity cycles. The lower right panel of Fig. 21 illustrates that the inner eccentricity (again,

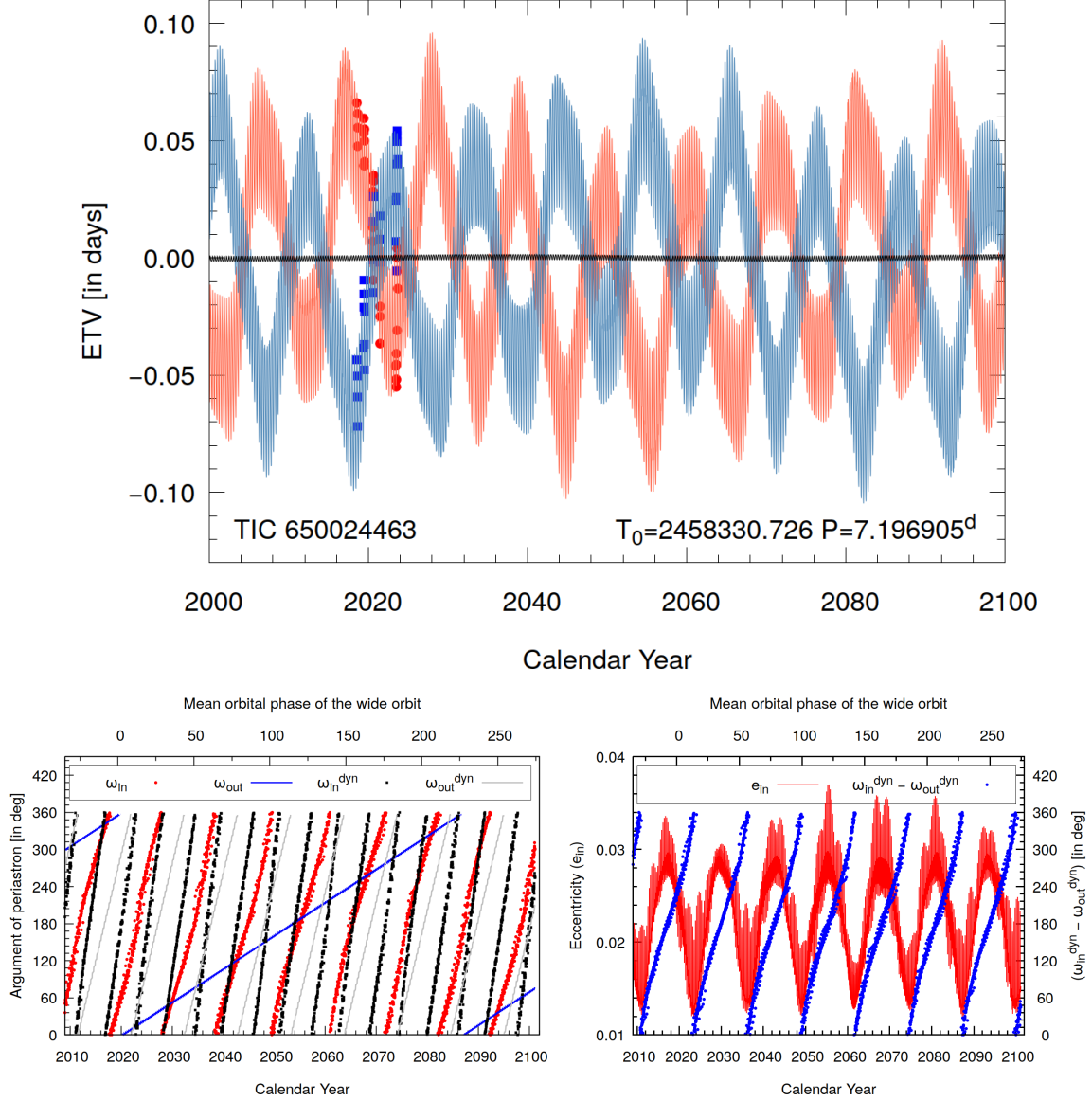


Fig. 21. Numerically integrated models for TIC 650024463 for the entire 21st century. *Upper panel:* Model ETV curve: red and blue lines represent the primary and secondary curves, respectively, while red circles and blue squares stand for the TESS-observed ETV points. Besides the rapidly oscillating vertical ‘spikes’, which come from the P_{out} period of 108 d, namely, the so-called medium term third-body perturbations, the 10.9 year third-body forced apsidal motion is also clearly visible. The amplitudes of consecutive half-cycles vary substantially which is the consequence of the octupole-order eccentricity perturbations. *Lower left panel:* Variations of the observable and dynamical arguments of periastron (i.e., the apsidal motion of the triple) until year 2100. *Lower right panel:* Cyclic variations of the inner eccentricity (e_{in} – red) and the corresponding, similar-period variations of the differences of the dynamical inner and outer arguments of periastrons ($\omega_{\text{in}}^{\text{dyn}} - \omega_{\text{out}}^{\text{dyn}}$ – blue) during the present century. See text for further details.

apart from the P_{out} -period mid-timescale variations) oscillates between $(e_{\text{in}})_{\text{min}} \sim 0.015$ and $(e_{\text{in}})_{\text{max}} \sim 0.028$ with the period mentioned above. As is known from the theory of the secular hierarchical three-body problem, for such an almost perfectly flat ($i_{\text{in}} = 0^{\circ}41 \pm 0^{\circ}27$) triple, the lowest order (quadrupole) perturbations in the inner eccentricity vanish (see, e.g. Naoz 2016) and, consequently, these e -cycles cannot be explained with the usual, quadrupole-order perturbations. On the other hand, these oscillations are in phase with the variations of the differences of the inner and outer dynamical arguments of periastron ($\Delta \equiv \omega_{\text{in}}^{\text{dyn}} - \omega_{\text{out}}^{\text{dyn}}$) and reach their extrema (i.e., minima and

maxima of e_{in} ’s) when $\Delta = 0^{\circ}$ or 180° and, hence, the octupole-order dominant perturbation term in e_{in} , which is proportional to $\sin \Delta$ (see, e.g., Borkovits & Mitnyan 2023, Eq. (12)), disappears. Thus, one can readily conclude that these e -cycles, and the concomitant variations in the shape of the apsidal ETV curves are direct, observable manifestations of the higher, octupole-order third-body perturbation effects.

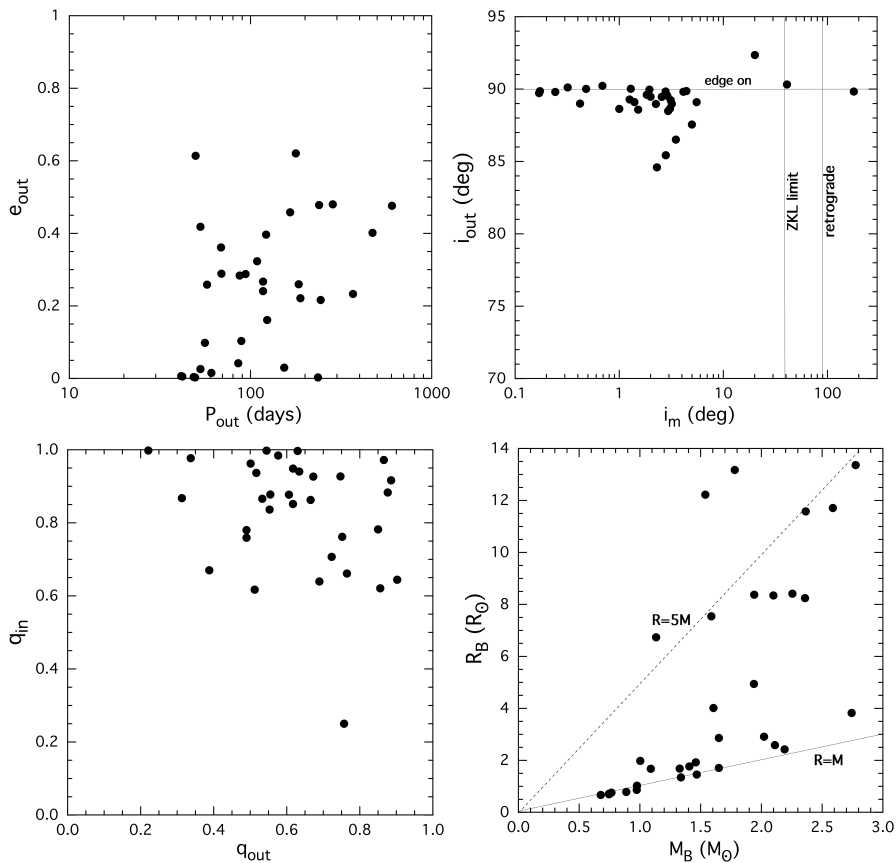


Fig. 22. Statistical plots for properties of 33 triply eclipsing triples uniformly analyzed (see text for references). *Top-row panels:* e_{out} vs. P_{out} and i_{out} vs. i_{mut} . In the upper right panel the vertical lines denote the transition to the ZLK cycles, and to retrograde orbits, respectively. *Bottom-row panels:* q_{in} vs. q_{out} and R_{B} vs. M_{B} . The sloped dashed lines in the latter plot are for $R_{\text{B}} = 1 M_{\text{B}}$ and $= 5 M_{\text{B}}$ (both expressed in solar units), as rough guides of unevolved and quite evolved stars, respectively.

8. Summary, discussion, and conclusions

In this work we have presented seven new compact triply eclipsing triples with a full solution to their stellar and orbital parameters. All of these systems were found by searching through millions of TESS photometric light curves looking for third body eclipses in binary systems (see e.g., Kristiansen et al. 2022; Rappaport et al. 2022).

We utilized the TESS photometric light curves, the ETV points derived from the light curves, archival SED data, archival photometry from ASAS-SN and ATLAS, and in some cases, ground-based follow up RV observations as well as eclipse photometry. These were combined in a complex photodynamical analysis where we solve for all the system parameters, as well as the distance to the source. Typical uncertainties on the masses and radii are in the range of a couple of per cent to not much more than ~ 5 per cent. Uncertainties on the angles associated with the orbital planes (e.g., i_{out} and i_{mut}) range from a fraction of a degree to about a degree. See Tables 6 through 9.

In Fig. 22 we present a set of four correlation plots among some of the physically interesting parameters associated with our collection of 33 recently analyzed triply eclipsing triples. To the seven sources presented in this work, we have added the 15 triples from our previous closely related papers (Rappaport et al. 2022) and (Rappaport et al. 2023), as well as eleven triples studied in Borkovits et al. (2019a, 2020b, 2022a,b), Czavalinga et al. (2023b), and Mitnyan et al. (2020) using largely the same selection criteria and methods of analysis.

The top left panel in Fig. 22 shows how e_{out} varies with P_{out} . In general, there is little correlation, except for the fact that the most circular outer orbits tend to have the relatively shorter outer periods, where the circularization may be brought about by tidal damping with an evolved tertiary. See also Fig. 19 and the associated discussion.

The top right panel of Fig. 22 shows the inclination angle of the outer orbit vs. the mutual inclination angle of the inner binary with respect to the outer orbit. The fact that most of the values of i_{out} lie near 90° is a selection effect since these triples were, in fact, discovered from the presence of third-body eclipses. To a lesser extent, the same selection also holds for the small values of i_{mut} , otherwise third body eclipses would be somewhat more difficult to detect. Two of the systems have large enough i_{mut} (20° and 40°) to undergo substantial precession of their orbital planes. Finally, there is one triple (TIC 276162169) in a nearly flat system, but where the outer orbit is retrograde with respect to the inner EB. These are rare systems.

The q_{in} vs. q_{out} plot (lower left panel in Fig. 22) shows an interesting feature, namely that the ratio of $q_{\text{out}} \equiv M_{\text{B}}/M_{\text{EB}}$ never exceeds unity (and not just by definition) and has a median value of 0.62. This result is not obviously caused by any selection effects. For purposes of this plot only we define q_{in} as the ratio of the lower mass to the higher mass star in the EB.

This result for \bar{q}_{out} having a mean of ~ 0.62 and never exceeding unity, favors a formation scenario for tight triples involving sequential disk fragmentation and subsequent accretion proposed by Tokovinin & Moe (2020) (see also Tokovinin 2021;

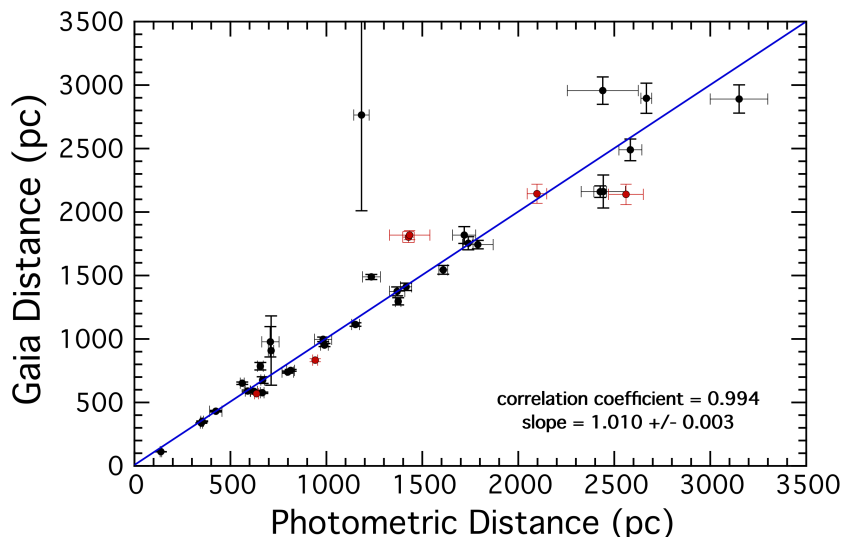


Fig. 23. Comparison of Gaia distances (Bailer-Jones et al. 2021) to 40 triple systems with distances found from our photodynamical fits to the system parameters. The systems marked in red are 6 from the current work with fitted distances. The blue curve is the line where the Gaia and our photometric distances would match. The formal correlation coefficient between the two sets of data is 0.994, and the fitted slope is 1.010 ± 0.003 . There is one system, TIC 52041148, at a Gaia distance of 5931 ± 400 pc and photometric distance of 1375 ± 30 , that is off the plot.

Offner et al. 2023, for recent reviews), In this scenario, the accretion rate onto the protostellar cores has an inverse relation with their mass-ratio. Hence, the less massive core of the progenitor EB secondary accretes faster while it has lower mass. Similarly, the tertiary, with the youngest core, will accrete faster while it has lower mass than the sum of the elder, inner cores. Consequently, under the assumption that there is enough matter, the triple tends toward a ‘double twin’ scenario, which means that both q_{in} and q_{out} would be about unity. Naturally, the accretion may stop earlier, resulting in $q_{out} < 1$, but it does not allow for $q_{out} > 1$.

The bottom right panel of Fig. 22 shows the relation between the tertiary radius and its mass. About a dozen of the stars lie fairly near the main sequence, roughly represented by the $R = M$ line in the figure. However, the other ~ 20 of the tertiary stars have evolved distinctly away from the main sequence. That is due both to an observational selection effect involving the detectability of third-body eclipses, and the fact that the EB stars cannot grow as large as the tertiaries without overflowing their Roche lobes.

A couple of the statistical plots rely on the following assumption made in our photodynamical analyses. Here we have generally adopted the assumption that the inner EB stars are coeval with the tertiary stars and, specifically, that no mass has been transferred among the stars or lost from the system. In turn, this includes the assumption that the tertiary star itself was always a single star, and not the merger product of another binary star.

Another item worthy of a brief discussion is the photometric distance we derive vs. the parallactic distance found by Gaia. Our distances are plotted in Fig. 23 where they are compared to Gaia’s distances. These are the same 33 triply eclipsing systems discussed above (of which we have photometric distances for 31), and augmented by 9 other triple systems analyzed in the same manner, but which are not triply eclipsing. These latter sources are taken from Borkovits et al. (2020a, 2022b), Gaulme et al. (2022), and Borkovits & Mitnyan (2023).

The overall general agreement between the Gaia distances and our photometric distances is quite striking, and with generally comparable error bars. The formal correlation coefficient

between the two sets of distances is 0.993 and the fitted slope between them is 1.028 ± 0.004 . Aside from this general agreement, there are a fair number of points where the two distances differ by more than a few statistical error bars. In these cases, it is not obvious from an inspection of this figure which distance is the more accurate one. This may be a case where one or both sets have underestimated uncertainties. In the case of Gaia, the outer orbit, which can be of the order of a 1/2-1 year, may be slightly distorting the parallax measurement¹⁶. For our photometric distances, there may be issues with inhomogeneous SED data, some of which may be taken during eclipses, the PARSEC isochrones are based on isolated and non-rotating stars, and there are uncertainties in the wavelength-dependent interstellar extinction that we use.

Now that the 33 triply eclipsing triples discussed above (see Fig. 22) have their basic parameters determined, and all but three have outer periods shorter than a year, this would make for an interesting follow-up ground-based eclipse timing project. Most of these systems are accessible with modest-size amateur telescopes since the majority of the 33 objects have G magnitudes of ≤ 13 . The ETV data from TESS itself was typically quite fundamental in the determination of the systems parameters via the photodynamical analyses. Therefore, future timing observations of the regular EB eclipses in these systems could significantly improve the parameter determinations. The ETV delays are typically in the minute range, so readily within the reach of amateur observations. Since there are a large number of these triply eclipsing triples, there should be a system to observe nearly every night.

Acknowledgements. This project has received funding from the HUN-REN Hungarian Research Network. T. B., T. M., I. B. B. and A. P. acknowledge the financial support of the Hungarian National Research, Development and Innovation Office – NKFIH Grants K-147131 and K-138962. This paper makes extensive use of data collected by the TESS mission. Funding for the TESS mission is provided by the NASA Science Mission Directorate. Some of the data presented

¹⁶ In this context we note that it was pointed out in Sect. 5.3 of Borkovits et al. (2022a) that, in the case of TIC 52041148, the extreme outlier Gaia EDR3 parallax-derived distance of Bailer-Jones et al. (2021) cannot be physically realistic.

in this paper were obtained from the Mikulski Archive for Space Telescopes (MAST). STScI is operated by the Association of Universities for Research in Astronomy, Inc., under NASA contract NAS5-26555. Support for MAST for non-HST data is provided by the NASA Office of Space Science via grant NNX09AF08G and by other grants and contracts. Distances and other astrometric properties for all targets, and outer orbits for two of our sources, were taken from the archives of European Space Agency (ESA) mission *Gaia*¹⁷, processed by the *Gaia* Data Processing and Analysis Consortium (DPAC)¹⁸. Funding for the DPAC has been provided by national institutions, in particular the institutions participating in the *Gaia* Multilateral Agreement. Some of the SED fluxes and magnitudes were obtained with the Wide-field Infrared Survey Explorer, which is a joint project of the University of California, Los Angeles, and the Jet Propulsion Laboratory/California Institute of Technology, funded by the National Aeronautics and Space Administration. Additionally, some of the SED fluxes and magnitudes were obtained with the Two Micron All Sky Survey, which is a joint project of the University of Massachusetts and the Infrared Processing and Analysis Center/California Institute of Technology, funded by the National Aeronautics and Space Administration and the National Science Foundation. We used the Simbad service operated by the Centre des Données Stellaires (Strasbourg, France) and the ESO Science Archive Facility services (data obtained under request number 396301). This research has also made use of the VizieR catalogue access tool, CDS, Strasbourg, France (DOI : 10.26093/cds/vizieR). The original description of the VizieR service was published in Ochslein et al. (2000). Our searches for outer orbital periods from photometry utilized archival data from the Asteroid Terrestrial-impact Last Alert System (ATLAS) project. The Asteroid Terrestrial-impact Last Alert System (ATLAS) project is primarily funded to search for near earth asteroids through NASA grants NN12AR55G, 80NSSC18K0284, and 80NSSC18K1575; byproducts of the NEO search include images and catalogs from the survey area. This work was partially funded by Kepler/K2 grant J1944/80NSSC19K0112 and HST GO-15889, and STFC grants ST/T000198/1 and ST/S006109/1. The ATLAS science products have been made possible through the contributions of the University of Hawaii Institute for Astronomy, the Queen's University Belfast, the Space Telescope Science Institute, the South African Astronomical Observatory, and The Millennium Institute of Astrophysics (MAS), Chile. Our searches for outer orbital periods also made use of archival data from ASAS-SN data for this work. The ASAS-SN Sky Patrol (All-Sky Automated Survey for Supernovae) is an automated program to search for supernovae and other astronomical transients, headed by astronomers from Ohio State University (US). It has 20 robotic telescopes in both the northern and southern hemispheres and surveys the entire sky approximately once every day.

References

- Astropy Collaboration, Price-Whelan, A.M., Sipőcz, B.M., Günther, H.M., et al. 2018, *AJ*, 156, 123
- Babusiaux, C., Fabricius, C., Khanna, S., et al. 2023, *A&A*, 674, A32
- Bailer-Jones, C. A. L., Rybizki, J., Fousneau, M., Demleitner, M., Andrae, R., 2021, *AJ*, 161, 147
- Borkovits, T., & Mitnyan, T. 2023, *Universe*, 9, 485
- Borkovits, T., Derekas, A., Kiss, L.L., et al. 2013, *MNRAS*, 428, 1656
- Borkovits T., Rappaport S., Hajdu T., Sztakovics J., 2015, *MNRAS*, 448, 946
- Borkovits, T., Hajdu, T., Sztakovics, J., Rappaport, S., Levine, A., Bíró, I. B., Klagyivik, P., 2016, *MNRAS*, 455, 4136
- Borkovits, T., Albrecht, S., Rappaport, S., et al. 2018, *MNRAS*, 478, 513
- Borkovits, T., Rappaport, S., Kaye, T., et al. 2019a, *MNRAS*, 483, 1934
- Borkovits, T., Sperauskas, J., Tokovinin, A., Latham, D. W., Csányi, I., Hajdu, T., Molnár, L., 2019b, *MNRAS*, 487, 4631
- Borkovits, T., Rappaport, S., Hajdu, T., et al. 2020a, *MNRAS*, 493, 5005
- Borkovits, T., Rappaport, S., Tan, T.G., et al. 2020b, *MNRAS*, 496, 4624
- Borkovits, T., Rappaport, S., Maxted, P. F. L., et al. 2021, *MNRAS*, 503, 3759
- Borkovits, T., Mitnyan, T., Rappaport, S., et al. 2022a, *MNRAS*, 510, 1352
- Borkovits, T., Rappaport, S. A., Toonen, S., Moe, M., Mitnyan, T., Csányi, I., 2022b, *MNRAS*, 515, 3773
- Borucki W. J. et al., 2010, *Science*, 327, 977
- Brasseur, C.E., Phillip, C., Fleming, S.W., Mullally, S.E., & White, R.L. 2019, *Astrophysics Source Code Library*, record ascl:1905.007
- Bressan, A., Marigo, P., Girardi, L. et al. 2012, *MNRAS*, 427, 127
- Carter, J.A., Fabrycky, D.C., Ragozzine, D., et al. 2011, *Sci*, 331, 562
- Claret, A. 2023, *A&A*, 674, A67
- Csizmadia, Sz., Pasternacki, Th., Dreyer, C., Cabrera, J., Erikson, A., Rauer, H. 2013, *A&A*, 549, A9
- Cutri, R.M., Wright, E.L., Conrow, T., et al. 2013, *wise.rept*, 1C.
- Czavalinga, D.R., Mitnyan, T., Rappaport, S., Borkovits, T., Gagliano, R., Omohundro, M., Kristiansen, M.H.K., and Pál, A. 2023, *A&A*, 670, 75
- Czavalinga, D. R., Borkovits, T., Mitnyan, T., Rappaport, S. A. & Pál, A. 2023, *MNRAS*, 526, 2830
- Duerbeck, H. W., Rucinski, S. M. 2007, *AJ*, 133, 169
- Ebbighausen, E. G., Struve, O. 1956, *ApJ*, 124, 507
- Feinstein, A.D., Montet, B.T., Foreman-Mackey, D., et al. 2019, *PASP*, 131, 94502
- Ford, E. B., 2005, *AJ*, 129, 1706
- Gaia Collaboration, Prusti, T., de Bruijn, J. H. J., et al. 2016, *A&A*, 595, A1
- Gaia Collaboration, Brown, A. G. A., Vallenari, A., Prusti, T. et al. 2021, *A&A*, 649, A1
- Gaia Collaboration, Vallenari, A., Brown, A. G. A., et al. 2023, *A&A*, 674, A1
- Gaulme, P., Borkovits, T., Appourchaux, T., et al. 2022, *A&A*, 668, 173
- Ginsburg, A., Sipőcz, B.M., Brasseur, C.E., et al. 2019, *AJ*, 157, 98
- Hajdu, T., Borkovits, T., Forgács-Dajka, E., Sztakovics, J., Marschalkó, G., Benkő, J. M., Klagyivik, P., Sallai, M. J. 2017, *MNRAS*, 471, 1230
- Hajdu, T., Borkovits, T., Forgács-Dajka, E., et al. 2019, *MNRAS*, 485, 2562
- Henden, A. A., Levine, S., Terrell, D., Welch, D. 2015, *American Astronomical Society, AAS Meeting #225*, id.336.16
- Kim, C. -H., Kreiner, J. M., Zakrzewski, B., Ogłóża, W., Kim, H. -W., Jeong, M. -J. 2018, *ApJS*, 235, id. 41
- Kovács G., Zucker S., Mazeh T., 2002, *A&A*, 391, 369
- Kostov et al., 2021, *ApJ*, 917, 93
- Kostov, V.B., Powell, B.P., Rappaport, S.A., et al., 2022, *ApJS*, 259, 66
- Kostov, V.B., Powell, B.P., Rappaport, S.A., et al., 2024, *MNRAS*, 527, 3995
- Kochanek C. S. et al., 2017, *PASP*, 129, 104502
- Kristiansen, M.H., Rappaport, S., Vanderburg, A., et al. 2022, *PASP*, 134, 074401
- Kunder, A. et al., 2017, *AJ*, 153, 75
- Lightkurve Collaboration, Cardoso, José Vinícius de Miranda, Hedges, C., Gully-Santiago, M., et al. 2018, *Astrophysics Source Code Library*, record ascl:1812.013, arXiv:1812.013
- Lindgren, L., Bastian, U., Biermann, M., et al. 2021, *A&A*, 649, 4L
- Mardling R. A., & Aarseth S. J., 2001, *MNRAS*, 321, 398
- Maxted, P. F. L., 2023, *MNRAS*, 519, 3723
- Miller, N. J., Maxted, P. F. L., & Smalley, B. 2020, *MNRAS*, 497, 2899
- Mitnyan, T., Borkovits, T., Rappaport, S., Pál, A., Maxted, P. F. L., 2020, *MNRAS*, 498, 6034
- Naos, S. 2016, *ARA&A*, 54, 441
- Ochslein F., Bauer P., Marcout J., 2000, *A&AS*, 143, 23
- Offner, S. S. R., Moe, M., Kratter, K. M., Sadavoy, S. I., Jensen, E. L. N., Tobin, J. J., 2023 *ASP Conf. Ser.* 534, 275
- Otero, S. A. 2007, *Open European Journal on Variable Stars*, 0072, 1
- Paegert, M. et al. 2021, arXiv:2108.04778
- Paredes, L. A., Henry, T. J., Quinn, S. N., et al. 2021, *AJ*, 162, 176, doi: 10.3847/1538-3881/ac082a
- Pál, A., 2012, *MNRAS*, 421, 1825
- Pollacco, D. L.; Skillen, I.; Collier Cameron, A., et al. 2006, *PASP*, 118, 1407
- Powell, B.P., Kostov, V.B., Rappaport, S., et al. 2021, *AJ*, 161, 162
- Pribulla, T., Borkovits, T., Jayaraman, R., et al. 2023, *MNRAS*, 524, 4220
- Rappaport S., Deck K., Levine A., Borkovits T., Carter J., El Mellah I., Sanchis-Ojeda R., & Kalomeni B., 2013, *ApJ*, 768, 33
- Rappaport, S., Gary, B.L., Kaye, T., Vanderburg, A., Croll, B., & Benni, P. 2016, *MNRAS*, 458, 3904
- Rappaport, S., Borkovits, T., Gagliano, R., et al. 2022, *MNRAS*, 513, 4341
- Rappaport, S., Borkovits, T., Gagliano, R., et al. 2023, *MNRAS*, 521, 558
- Ricker, G.R., Winn, J.N., Vanderspek, R., et al. 2015, *JATIS*, 1, 014003
- Roemer, O. 1677, *Philosophical Transactions (1665-1678)*, Volume 12, 893
- Rowan, D.M. et al., 2023, *MNRAS*, 520, 2386
- Schmitt, A.R., Hartman, J.D., & Kipping, D.M. 2019, arXiv:1910.08034
- Shappee B. J. et al., 2014, *ApJ*, 788, 48
- Söderhjelm, S. 1975, *A&A*, 42, 229.
- Southworth, J., Zucker, S., Maxted, P. F. L., Smalley, B. 2004, *MNRAS*, 355, 986
- Spada, F., Demarque, P., Kim, Y.-C., & Sills, A. 2013, *ApJ*, 776, 87
- Skrutskie, M.F., Cutri, R.M., Stiening, R., et al. 2006, *AJ*, 131, 1163
- Smith, K.W., Smart, S.J., Young, D.R., Tony, J.L., et al. 2020, *PASP*, 132, 5002
- Stassun, K.G., & Torres, G. 2016, *AJ*, 152, 180
- Sterne T. E., 1939, *MNRAS*, 99, 451
- Strohmeier, W. 1966, *IBVS*, 158, 1
- Tokovinin, A., 2021, *Universe*, 7, 352
- Tokovinin, A., Fischer, D.A., Bonati, M., et al. 2013, *PASP*, 125, 1336
- Tokovinin, A., & Moe, M. 2020, *MNRAS*, 491, 5158
- Tony, J.L., Denneau, L., Heinze, A.N., et al. 2018, *PASP*, 130, 4505
- Udalski, A.; Kubiak, M.; Szymanski, M. 1997, *Acta Astron.*, 47, 319
- Zasche, P. 2012, *Acta Astron.*, 62, 97
- Zahn, J. P. 1977, *A&A*, 57, 383

¹⁷ <https://www.cosmos.esa.int/gaia>

¹⁸ <https://www.cosmos.esa.int/web/gaia/dpac/consortium>

Appendix A: Eclipse times of the inner EBs of the seven triples

In this appendix we tabulate the times of the individual primary and secondary eclipses of the inner EBs of the triples considered in this study. These naturally include mostly eclipses from TESS, plus a few that were observed from the ground (Tables A.1–A.7).

Table A.1. Eclipse times for TIC 133771812

BJD –2 400 000	Cycle no.	std. dev. (<i>d</i>)	BJD –2 400 000	Cycle no.	std. dev. (<i>d</i>)	BJD –2 400 000	Cycle no.	std. dev. (<i>d</i>)	BJD –2 400 000	Cycle no.	std. dev. (<i>d</i>)
58495.15572	–0.5	0.00129	58538.30974	3.0	0.00107	59261.99860	61.5	0.00484	59985.53480	120.0	0.00044
58501.18645	0.0	0.00051	59230.98511	59.0	0.00059	59274.37006	62.5	0.00490	59991.73798	120.5	0.00114
58507.52038	0.5	0.00597	59243.35923	60.0	0.00052	59966.99857	118.5	0.00099	59997.91101	121.0	0.00029
58513.56058	1.0	0.00052	59249.63045	60.5	0.00090	59973.15918	119.0	0.00038	60004.10785	121.5	0.00073
58519.89039	1.5	0.00158	59255.73720	61.0	0.00181	59979.36605	119.5	0.00101	60010.28418	122.0	0.00041
58525.93650	2.0	0.00051									

Notes. Integer and half-integer cycle numbers (here and the following tables) denote primary and secondary eclipses, respectively.

Table A.2. Eclipse times for TIC 176713425

BJD –2 400 000	Cycle no.	std. dev. (<i>d</i>)	BJD –2 400 000	Cycle no.	std. dev. (<i>d</i>)	BJD –2 400 000	Cycle no.	std. dev. (<i>d</i>)	BJD –2 400 000	Cycle no.	std. dev. (<i>d</i>)
58738.87091	–0.5	0.00016	58760.71389	11.0	0.00015	58784.43845	23.5	0.00015	59869.56727	595.0	0.00007
58739.82153	0.0	0.00026	58761.66181	11.5	0.00020	58785.38567	24.0	0.00015	59870.51853	595.5	0.00010
58740.77369	0.5	0.00023	58762.60987	12.0	0.00014	58786.33606	24.5	0.00015	59871.46504	596.0	0.00007
58741.72591	1.0	0.00018	58765.45725	13.5	0.00024	58787.28548	25.0	0.00016	59872.41525	596.5	0.00009
58742.67534	1.5	0.00014	58766.40505	14.0	0.00019	58788.23455	25.5	0.00038	59873.36401	597.0	0.00008
58743.62592	2.0	0.00024	58767.35647	14.5	0.00011	58789.18950	26.0	0.00086	59874.31226	597.5	0.00009
58744.57356	2.5	0.00019	58768.30415	15.0	0.00013	59758.49509 ^a	536.5	0.00004	59875.26216	598.0	0.00010
58745.52534	3.0	0.00010	58769.25387	15.5	0.00022	59853.43423	586.5	0.00009	59876.21071	598.5	0.00009
58746.47509	3.5	0.00019	58770.20236	16.0	0.00013	59854.38270	587.0	0.00009	59877.15953	599.0	0.00009
58747.42357	4.0	0.00014	58771.15121	16.5	0.00020	59855.33184	587.5	0.00009	59878.10921	599.5	0.00010
58748.37530	4.5	0.00022	58772.10136	17.0	0.00011	59856.28088	588.0	0.00011	59879.05671	600.0	0.00009
58749.32190	5.0	0.00015	58773.04374	17.5	0.00196	59857.23138	588.5	0.00008	59880.00742	600.5	0.00011
58750.27213	5.5	0.00024	58773.99852	18.0	0.00022	59858.17868	589.0	0.00010	59880.95465	601.0	0.00008
58752.17061	6.5	0.00019	58774.94872	18.5	0.00023	59859.13005	589.5	0.00011	59881.90507	601.5	0.00010
58753.12064	7.0	0.00015	58775.89613	19.0	0.00031	59860.07715	590.0	0.00009	60135.38686 ^b	735.0	0.00010
58754.06873	7.5	0.00016	58777.79345	20.0	0.00017	59861.02787	590.5	0.00013	60208.48369 ^b	773.5	0.00003
58755.01904	8.0	0.00012	58778.74329	20.5	0.00025	59861.97509	591.0	0.00008	60209.43240 ^b	774.0	0.00004
58755.96778	8.5	0.00016	58779.69151	21.0	0.00018	59862.92622	591.5	0.00009	60267.35271 ^b	804.5	0.00003
58756.91576	9.0	0.00027	58780.64248	21.5	0.00015	59866.72126	593.5	0.00009	60268.30225 ^b	805.0	0.00007
58757.86637	9.5	0.00019	58781.59047	22.0	0.00013	59867.66957	594.0	0.00008	60286.34061 ^b	814.5	0.00003
58758.81356	10.0	0.00014	58782.53835	22.5	0.00020	59868.61941	594.5	0.00010	60344.24895 ^b	845.0	0.00004
58759.76472	10.5	0.00019	58783.48854	23.0	0.00010						

Notes. ^a: Observed at BAO; ^b: Observed at GAO; the other eclipses observed with TESS.

Table A.3. Eclipse times for TZ Pyx (TIC 185615681)

BJD -2 400 000	Cycle no.	std. dev. (<i>d</i>)	BJD -2 400 000	Cycle no.	std. dev. (<i>d</i>)	BJD -2 400 000	Cycle no.	std. dev. (<i>d</i>)	BJD -2 400 000	Cycle no.	std. dev. (<i>d</i>)
58518.16959	0.0	0.00009	59238.09281	310.5	0.00003	59274.02312	326.0	0.00003	59986.98206	633.5	0.00002
58519.34246	0.5	0.00009	59239.24465	311.0	0.00004	59275.18922	326.5	0.00004	59988.14316	634.0	0.00002
58520.48810	1.0	0.00013	59240.41124	311.5	0.00003	59276.34210	327.0	0.00003	59989.30061	634.5	0.00002
58521.66086	1.5	0.00007	59242.72960	312.5	0.00003	59277.50798	327.5	0.00003	59990.46173	635.0	0.00002
58522.80632	2.0	0.00009	59243.88184	313.0	0.00003	59278.66089	328.0	0.00003	59991.61920	635.5	0.00002
58523.97938	2.5	0.00008	59245.04810	313.5	0.00003	59279.82680	328.5	0.00004	59992.78021	636.0	0.00002
58525.12478	3.0	0.00006	59246.20042	314.0	0.00005	59963.79769	623.5	0.00002	59993.93777	636.5	0.00002
58526.29777	3.5	0.00010	59247.36660	314.5	0.00004	59964.95824	624.0	0.00003	59996.25634	637.5	0.00002
58527.44319	4.0	0.00011	59248.51888	315.0	0.00004	59967.27669	625.0	0.00002	59997.41758	638.0	0.00002
58528.61638	4.5	0.00008	59249.68494	315.5	0.00004	59968.43440	625.5	0.00002	59998.57505	638.5	0.00002
58530.93462	5.5	0.00009	59250.83729	316.0	0.00004	59969.59564	626.0	0.00004	59999.73656	639.0	0.00005
58535.57206	7.5	0.00009	59252.00343	316.5	0.00004	59970.75292	626.5	0.00002	60000.89359	639.5	0.00005
58536.71703	8.0	0.00010	59253.15574	317.0	0.00004	59971.91399	627.0	0.00002	60002.05537	640.0	0.00002
58537.89034	8.5	0.00010	59256.64039	318.5	0.00003	59973.07121	627.5	0.00002	60003.21247	640.5	0.00002
58539.03562	9.0	0.00011	59257.79257	319.0	0.00005	59974.23254	628.0	0.00002	60004.37418	641.0	0.00002
58540.20874	9.5	0.00008	59258.95891	319.5	0.00004	59976.55100	629.0	0.00002	60005.53109	641.5	0.00002
58541.35423	10.0	0.00008	59260.11101	320.0	0.00004	59977.70821	629.5	0.00002	60006.69298	642.0	0.00002
59229.97068	307.0	0.00004	59261.27743	320.5	0.00004	59978.86955	630.0	0.00002	60007.84981	642.5	0.00002
59231.13745	307.5	0.00004	59262.42937	321.0	0.00004	59980.02659	630.5	0.00002	60009.01147	643.0	0.00002
59232.28914	308.0	0.00004	59263.59588	321.5	0.00004	59981.18779	631.0	0.00002	60010.16837	643.5	0.00002
59233.45587	308.5	0.00004	59264.74799	322.0	0.00004	59983.50631	632.0	0.00002	60011.32996	644.0	0.00002
59234.60749	309.0	0.00004	59265.91448	322.5	0.00004	59984.66356	632.5	0.00002	60012.48686	644.5	0.00002
59235.77432	309.5	0.00003	59267.06667	323.0	0.00004	59985.82477	633.0	0.00002	60013.64839	645.0	0.00002
59236.92609	310.0	0.00004	59272.87044	325.5	0.00003						

Table A.4. Eclipse times for TIC 287756035

BJD -2 400 000	Cycle no.	std. dev. (<i>d</i>)	BJD -2 400 000	Cycle no.	std. dev. (<i>d</i>)	BJD -2 400 000	Cycle no.	std. dev. (<i>d</i>)	BJD -2 400 000	Cycle no.	std. dev. (<i>d</i>)
58597.24221	-1.0	0.09984	58623.26018	11.5	0.00368	59336.13166	354.0	0.00281	60041.73549	693.0	0.00109
58598.27373	-0.5	0.00665	59308.03345	340.5	0.00214	59337.16701	354.5	0.00323	60042.78350	693.5	0.00173
58599.31567	0.0	0.00452	59309.07420	341.0	0.00187	59338.20811	355.0	0.00230	60043.81491	694.0	0.00149
58600.35967	0.5	0.00178	59313.29341	343.0	0.00326	59339.24448	355.5	0.00283	60044.85216	694.5	0.00216
58601.40239	1.0	0.00181	59314.28649	343.5	0.00230	59340.30039	356.0	0.00243	60049.01666	696.5	0.00268
58602.43427	1.5	0.00197	59315.31438	344.0	0.00171	59341.33582	356.5	0.00191	60050.05709	697.0	0.00119
58603.47656	2.0	0.00287	59316.35173	344.5	0.00173	59342.37244	357.0	0.00175	60051.09339	697.5	0.00169
58604.52050	2.5	0.00177	59317.39805	345.0	0.00126	59343.41287	357.5	0.00139	60052.13384	698.0	0.00146
58605.55465	3.0	0.00206	59318.45364	345.5	0.00198	59344.46241	358.0	0.00121	60053.17517	698.5	0.00140
58606.59093	3.5	0.00339	59320.52522	346.5	0.00240	59345.50382	358.5	0.00176	60054.22572	699.0	0.00123
58607.63434	4.0	0.00276	59321.56601	347.0	0.00180	59347.57886	359.5	0.00250	60056.29312	700.0	0.00144
58608.67791	4.5	0.00162	59322.59519	347.5	0.00209	59348.61854	360.0	0.00194	60057.33468	700.5	0.00128
58611.79733	6.0	0.14594	59323.64770	348.0	0.00162	59349.65894	360.5	0.00157	60058.38237	701.0	0.00136
58612.82854	6.5	0.01613	59324.69195	348.5	0.00193	59350.70147	361.0	0.00163	60059.42664	701.5	0.00177
58613.88105	7.0	0.02453	59325.71101	349.0	0.00163	59351.74403	361.5	0.00250	60060.45615	702.0	0.00129
58614.92035	7.5	0.00293	59326.74897	349.5	0.00241	59352.78385	362.0	0.00221	60061.50146	702.5	0.00194
58615.96147	8.0	0.00275	59327.80051	350.0	0.00170	59353.81992	362.5	0.00290	60062.55115	703.0	0.00127
58617.00661	8.5	0.00457	59328.83824	350.5	0.00197	59354.86158	363.0	0.00164	60063.59200	703.5	0.00167
58618.04633	9.0	0.00338	59329.88489	351.0	0.00171	59355.90671	363.5	0.00237	60064.63478	704.0	0.00149
58619.08382	9.5	0.00349	59330.92391	351.5	0.00194	59356.94344	364.0	0.00228	60065.67316	704.5	0.00227
58620.12676	10.0	0.18136	59331.95671	352.0	0.00185	59357.98665	364.5	0.00497	60066.70700	705.0	0.00271
58621.16943	10.5	0.00432	59334.05750	353.0	0.00395	59359.02178	365.0	0.00192	60067.74751	705.5	0.00188
58622.21359	11.0	0.00359	59335.09428	353.5	0.00328	59360.06104	365.5	0.00397			

Table A.5. Eclipse times for TIC 321978218

BJD -2 400 000	Cycle no.	std. dev. (<i>d</i>)	BJD -2 400 000	Cycle no.	std. dev. (<i>d</i>)	BJD -2 400 000	Cycle no.	std. dev. (<i>d</i>)	BJD -2 400 000	Cycle no.	std. dev. (<i>d</i>)
55432.54833	-6369.5	0.00031	59064.81212	5.0	0.00006	59097.29401	62.0	0.00005	60170.53185	1945.5	0.00009
55432.83201	-6369.0	0.00015	59065.09753	5.5	0.00013	59097.57864	62.5	0.00009	60170.81671	1946.0	0.00004
55803.49700	-5718.5	0.00034	59065.38192	6.0	0.00005	59097.86390	63.0	0.00007	60171.10179	1946.5	0.00010
56180.70955	-5056.5	0.00033	59065.66669	6.5	0.00012	59098.14911	63.5	0.00011	60171.38676	1947.0	0.00007
56180.99554	-5056.0	0.00029	59065.95165	7.0	0.00006	59098.43374	64.0	0.00006	60171.67182	1947.5	0.00007
56533.99015	-4436.5	0.00044	59066.23684	7.5	0.00012	59098.71815	64.5	0.00015	60171.95628	1948.0	0.00005
56534.27516	-4436.0	0.00017	59066.52152	8.0	0.00006	59099.00333	65.0	0.00012	60172.24210	1948.5	0.00007
56896.10467	-3801.0	0.00031	59066.80643	8.5	0.00010	59099.28814	65.5	0.00010	60172.52667	1949.0	0.00005
58354.25863	-1242.0	0.00005	59067.09170	9.0	0.00012	59099.57334	66.0	0.00007	60172.81093	1949.5	0.00008
58354.54400	-1241.5	0.00053	59067.37738	9.5	0.00006	59099.85891	66.5	0.00014	60173.09665	1950.0	0.00005
58354.82840	-1241.0	0.00077	59067.66102	10.0	0.00005	59100.14269	67.0	0.00017	60173.38171	1950.5	0.00009
58355.11293	-1240.5	0.00041	59067.94616	10.5	0.00010	59100.99845	68.5	0.00045	60173.66615	1951.0	0.00005
58355.39782	-1240.0	0.00005	59068.23123	11.0	0.00006	59101.28153	69.0	0.00013	60173.95097	1951.5	0.00008
58355.68338	-1239.5	0.00037	59068.51567	11.5	0.00006	59102.42163	71.0	0.00010	60174.23623	1952.0	0.00005
58355.96786	-1239.0	0.00006	59068.80059	12.0	0.00007	59102.70658	71.5	0.00010	60174.52103	1952.5	0.00011
58356.25342	-1238.5	0.00029	59069.08609	12.5	0.00014	59102.99178	72.0	0.00007	60174.80594	1953.0	0.00006
58356.53756	-1238.0	0.00023	59069.37046	13.0	0.00005	59103.27701	72.5	0.00008	60175.37574	1954.0	0.00005
58356.82293	-1237.5	0.00009	59069.65543	13.5	0.00009	59103.56120	73.0	0.00007	60175.66128	1954.5	0.00006
58357.10703	-1237.0	0.00026	59069.94014	14.0	0.00007	59103.84650	73.5	0.00010	60175.94620	1955.0	0.00006
58357.39208	-1236.5	0.00008	59070.22620	14.5	0.00014	59104.13146	74.0	0.00003	60176.23119	1955.5	0.00009
58357.67696	-1236.0	0.00004	59070.51025	15.0	0.00010	59104.41625	74.5	0.00012	60176.51561	1956.0	0.00004
58357.96167	-1235.5	0.00007	59070.79605	15.5	0.00007	59104.70096	75.0	0.00004	60176.80099	1956.5	0.00009
58358.24659	-1235.0	0.00039	59071.08036	16.0	0.00009	59104.98676	75.5	0.00013	60177.08567	1957.0	0.00005
58358.53170	-1234.5	0.00053	59071.36490	16.5	0.00014	59105.27098	76.0	0.00004	60177.37105	1957.5	0.00010
58358.81611	-1234.0	0.00005	59071.64989	17.0	0.00008	59105.55572	76.5	0.00012	60177.65572	1958.0	0.00006
58359.10180	-1233.5	0.00008	59071.93526	17.5	0.00024	59105.84032	77.0	0.00006	60177.94107	1958.5	0.00012
58359.38589	-1233.0	0.00012	59072.78988	19.0	0.00012	59106.12549	77.5	0.00013	60178.22531	1959.0	0.00005
58359.67124	-1232.5	0.00033	59073.07423	19.5	0.00016	59106.41026	78.0	0.00009	60178.51088	1959.5	0.00010
58359.95639	-1232.0	0.00016	59073.35993	20.0	0.00008	59106.69512	78.5	0.00011	60178.79519	1960.0	0.00006
58360.24095	-1231.5	0.00013	59073.64513	20.5	0.00013	59106.98023	79.0	0.00006	60179.08063	1960.5	0.00012
58360.52551	-1231.0	0.00017	59073.92936	21.0	0.00013	59107.26571	79.5	0.00011	60179.36579	1961.0	0.00006
58360.81125	-1230.5	0.00048	59075.35427	23.5	0.00014	59107.54988	80.0	0.00005	60179.64921	1961.5	0.00017
58361.09545	-1230.0	0.00011	59075.63916	24.0	0.00007	59107.83547	80.5	0.00010	60179.93525	1962.0	0.00011
58361.95049	-1228.5	0.00009	59075.92461	24.5	0.00006	59108.11935	81.0	0.00008	60181.92901	1965.5	0.00018
58362.23444	-1228.0	0.00007	59076.20896	25.0	0.00007	59108.40407	81.5	0.00012	60184.49411	1970.0	0.00006
58362.52030	-1227.5	0.00006	59076.49390	25.5	0.00010	59108.68935	82.0	0.00006	60184.77872	1970.5	0.00009
58362.80462	-1227.0	0.00043	59076.77904	26.0	0.00006	59108.97479	82.5	0.00011	60185.06332	1971.0	0.00004

Note. The first eight eclipse times are SWASP seasonal normal minima.

Table A.5. Eclipse times for TIC 321978218 (continued)

BJD -2 400 000	Cycle no.	std. dev. (d)	BJD -2 400 000	Cycle no.	std. dev. (d)	BJD -2 400 000	Cycle no.	std. dev. (d)	BJD -2 400 000	Cycle no.	std. dev. (d)
58363.09051	-1226.5	0.00044	59077.06362	26.5	0.00012	59109.25888	83.0	0.00004	60185.34860	1971.5	0.00009
58363.37465	-1226.0	0.00018	59077.34871	27.0	0.00004	59109.54467	83.5	0.00012	60185.63322	1972.0	0.00003
58363.65930	-1225.5	0.00036	59077.63344	27.5	0.00010	59109.82896	84.0	0.00006	60185.91880	1972.5	0.00008
58363.94412	-1225.0	0.00011	59077.91895	28.0	0.00007	59110.11457	84.5	0.00012	60186.20319	1973.0	0.00006
58364.22942	-1224.5	0.00073	59078.20347	28.5	0.00008	59110.39867	85.0	0.00005	60186.48824	1973.5	0.00008
58364.51351	-1224.0	0.00022	59078.48835	29.0	0.00004	59110.68353	85.5	0.00010	60186.77318	1974.0	0.00005
58364.79930	-1223.5	0.00028	59078.77336	29.5	0.00010	59110.96839	86.0	0.00007	60187.05835	1974.5	0.00009
58365.08375	-1223.0	0.00072	59079.05850	30.0	0.00006	59111.25309	86.5	0.00016	60187.34295	1975.0	0.00004
58365.65311	-1222.0	0.00008	59079.34428	30.5	0.00011	59111.53759	87.0	0.00005	60187.62724	1975.5	0.00010
58365.93808	-1221.5	0.00027	59079.62838	31.0	0.00007	59111.82388	87.5	0.00011	60189.33714	1978.5	0.00010
58366.22315	-1221.0	0.00005	59079.91356	31.5	0.00010	59112.10796	88.0	0.00005	60189.62196	1979.0	0.00004
58366.50759	-1220.5	0.00026	59080.19822	32.0	0.00007	59112.39400	88.5	0.00011	60189.90762	1979.5	0.00009
58366.79308	-1220.0	0.00006	59080.48254	32.5	0.00010	59112.67687	89.0	0.00006	60190.19141	1980.0	0.00004
58367.07824	-1219.5	0.00025	59080.76794	33.0	0.00007	59112.96266	89.5	0.00013	60190.47693	1980.5	0.00007
58368.78739	-1216.5	0.00014	59081.05359	33.5	0.00011	59113.24702	90.0	0.00008	60190.76149	1981.0	0.00005
58369.07163	-1216.0	0.00020	59081.33822	34.0	0.00006	59113.53268	90.5	0.00017	60191.04627	1981.5	0.00008
58369.35674	-1215.5	0.00014	59081.62342	34.5	0.00013	59113.81609	91.0	0.00017	60191.33106	1982.0	0.00006
58369.64203	-1215.0	0.00012	59081.90811	35.0	0.00008	59114.38750	92.0	0.00016	60191.61713	1982.5	0.00011
58369.92672	-1214.5	0.00012	59082.19335	35.5	0.00009	60154.86236	1918.0	0.00005	60191.90127	1983.0	0.00006
58370.21158	-1214.0	0.00004	59082.47818	36.0	0.00006	60155.14715	1918.5	0.00010	60192.47097	1984.0	0.00005
58370.49678	-1213.5	0.00073	59082.76255	36.5	0.00010	60155.43215	1919.0	0.00004	60192.75595	1984.5	0.00011
58370.78086	-1213.0	0.00010	59083.04770	37.0	0.00006	60155.71622	1919.5	0.00011	60193.04077	1985.0	0.00008
58371.06578	-1212.5	0.00485	59083.33232	37.5	0.00010	60156.00186	1920.0	0.00006	60193.32650	1985.5	0.00008
58371.35077	-1212.0	0.00021	59083.61766	38.0	0.00008	60156.28589	1920.5	0.00012	60193.61105	1986.0	0.00009
58371.63632	-1211.5	0.00038	59083.90258	38.5	0.00015	60156.57152	1921.0	0.00006	60195.31965	1989.0	0.00007
58371.92021	-1211.0	0.00017	59084.18769	39.0	0.00005	60156.85597	1921.5	0.00007	60195.60460	1989.5	0.00009
58372.20573	-1210.5	0.00022	59084.47272	39.5	0.00010	60157.14150	1922.0	0.00005	60195.88963	1990.0	0.00004
58372.49022	-1210.0	0.00012	59084.75741	40.0	0.00006	60157.42597	1922.5	0.00009	60196.17532	1990.5	0.00008
58372.77538	-1209.5	0.00015	59085.04258	40.5	0.00013	60157.71122	1923.0	0.00005	60196.45910	1991.0	0.00005
58373.06046	-1209.0	0.00006	59085.32708	41.0	0.00005	60157.99562	1923.5	0.00012	60196.74417	1991.5	0.00009
58373.34500	-1208.5	0.00020	59085.61266	41.5	0.00016	60158.28095	1924.0	0.00008	60197.02894	1992.0	0.00005
58373.91459	-1207.5	0.00045	59085.89765	42.0	0.00009	60158.56504	1924.5	0.00009	60197.31481	1992.5	0.00006
58374.19894	-1207.0	0.00056	59086.18239	42.5	0.00021	60158.85060	1925.0	0.00006	60197.59918	1993.0	0.00005
58374.48490	-1206.5	0.00020	59086.46679	43.0	0.00005	60159.13523	1925.5	0.00009	60197.88383	1993.5	0.00009
58374.76950	-1206.0	0.00017	59086.75295	43.5	0.00014	60159.42018	1926.0	0.00005	60198.16890	1994.0	0.00005
58375.05473	-1205.5	0.00054	59087.03672	44.0	0.00025	60159.70487	1926.5	0.00009	60198.45395	1994.5	0.00012
58375.33894	-1205.0	0.00015	59088.46235	46.5	0.00013	60159.99034	1927.0	0.00006	60198.73804	1995.0	0.00005
58375.62430	-1204.5	0.00019	59088.74683	47.0	0.00008	60160.27437	1927.5	0.00009	60199.02389	1995.5	0.00010
58375.90879	-1204.0	0.00004	59089.03181	47.5	0.00005	60160.55997	1928.0	0.00005	60199.30817	1996.0	0.00004
58376.19406	-1203.5	0.00264	59089.31654	48.0	0.00005	60160.84398	1928.5	0.00009	60199.59430	1996.5	0.00008
58376.47909	-1203.0	0.00014	59089.60100	48.5	0.00010	60161.12967	1929.0	0.00004	60199.87805	1997.0	0.00006
58376.76409	-1202.5	0.00013	59089.88607	49.0	0.00008	60161.41383	1929.5	0.00009	60200.16360	1997.5	0.00009
58377.04837	-1202.0	0.00010	59090.17046	49.5	0.00008	60161.69909	1930.0	0.00007	60200.44787	1998.0	0.00007
58377.61802	-1201.0	0.00004	59090.45626	50.0	0.00007	60162.26977	1931.0	0.00006	60200.73325	1998.5	0.00008
58377.90299	-1200.5	0.00026	59090.74131	50.5	0.00009	60162.55352	1931.5	0.00007	60201.01743	1999.0	0.00005
58378.18822	-1200.0	0.00021	59091.02573	51.0	0.00006	60162.83907	1932.0	0.00005	60201.30270	1999.5	0.00008
58378.47388	-1199.5	0.00006	59091.31199	51.5	0.00009	60163.12455	1932.5	0.00009	60201.87283	2000.5	0.00008
58378.75741	-1199.0	0.00018	59091.59603	52.0	0.00010	60163.40869	1933.0	0.00007	60202.15700	2001.0	0.00007
58379.04321	-1198.5	0.00044	59091.88104	52.5	0.00013	60163.69397	1933.5	0.00008	60202.44170	2001.5	0.00012
58379.32794	-1198.0	0.00013	59092.16592	53.0	0.00006	60163.97868	1934.0	0.00003	60202.72691	2002.0	0.00004
58379.61339	-1197.5	0.00020	59092.44995	53.5	0.00015	60164.54811	1935.0	0.00006	60203.01175	2002.5	0.00007
58379.89794	-1197.0	0.00005	59092.73559	54.0	0.00008	60164.83315	1935.5	0.00012	60203.29637	2003.0	0.00006
58380.18249	-1196.5	0.00030	59093.02059	54.5	0.00010	60165.68847	1937.0	0.00016	60203.58142	2003.5	0.00011
58380.46717	-1196.0	0.00014	59093.30530	55.0	0.00008	60165.97246	1937.5	0.00011	60203.86651	2004.0	0.00005
58380.75321	-1195.5	0.00061	59093.59059	55.5	0.00008	60166.25749	1938.0	0.00013	60204.15125	2004.5	0.00008
59061.96391	0.0	0.00004	59093.87482	56.0	0.00004	60167.96658	1941.0	0.00011	60204.43604	2005.0	0.00005
59062.24885	0.5	0.00012	59094.16049	56.5	0.00010	60168.25338	1941.5	0.00011	60204.72083	2005.5	0.00012
59062.53368	1.0	0.00005	59094.44458	57.0	0.00006	60168.53695	1942.0	0.00005	60205.00588	2006.0	0.00005
59062.81852	1.5	0.00009	59094.72981	57.5	0.00008	60168.82209	1942.5	0.00009	60205.29123	2006.5	0.00009
59063.10327	2.0	0.00005	59095.01455	58.0	0.00008	60169.10719	1943.0	0.00004	60205.57546	2007.0	0.00006
59063.38898	2.5	0.00009	59095.29898	58.5	0.00006	60169.39239	1943.5	0.00009	60205.85994	2007.5	0.00008
59063.67320	3.0	0.00005	59096.43927	60.5	0.00013	60169.67701	1944.0	0.00004	60206.14508	2008.0	0.00008
59063.95823	3.5	0.00008	59096.72412	61.0	0.00005	60169.96218	1944.5	0.00009	60206.43015	2008.5	0.00013
59064.24238	4.0	0.00004	59097.00893	61.5	0.00018	60170.24681	1945.0	0.00005	60206.71478	2009.0	0.00007
59064.52777	4.5	0.00010									

Table A.6. Eclipse times for TIC 323486857

BJD -2 400 000	Cycle no.	std. dev. (d)	BJD -2 400 000	Cycle no.	std. dev. (d)	BJD -2 400 000	Cycle no.	std. dev. (d)	BJD -2 400 000	Cycle no.	std. dev. (d)
58569.76629	0.0	0.00043	58611.31389	47.0	0.00030	59335.30793	866.0	0.00042	60056.64267	1682.0	0.00029
58570.20988	0.5	0.00031	58611.75668	47.5	0.00037	59335.74280	866.5	0.00071	60057.08554	1682.5	0.00023
58570.65159	1.0	0.00051	58612.19847	48.0	0.00033	59336.18785	867.0	0.00061	60057.52397	1683.0	0.00031
58571.09320	1.5	0.00072	58612.63979	48.5	0.00029	59336.63213	867.5	0.00056	60057.96929	1683.5	0.00035
58571.53535	2.0	0.00022	58613.08175	49.0	0.00029	59337.07349	868.0	0.00046	60058.40908	1684.0	0.00029
58571.97855	2.5	0.00027	58613.52515	49.5	0.00041	59337.51399	868.5	0.00074	60058.85300	1684.5	0.00030
58572.41999	3.0	0.00032	58613.96601	50.0	0.00043	59337.95543	869.0	0.00056	60059.29364	1685.0	0.00022
58572.86354	3.5	0.00069	58614.41042	50.5	0.00046	59338.40096	869.5	0.00050	60059.73704	1685.5	0.00033
58573.30288	4.0	0.00026	58614.84916	51.0	0.00023	59338.84369	870.0	0.00068	60060.17791	1686.0	0.00023
58573.74551	4.5	0.00052	58616.18135	52.5	0.00022	59340.16948	871.5	0.00046	60060.61934	1686.5	0.00035
58575.07036	6.0	0.00033	58616.62435	53.0	0.00031	59340.60799	872.0	0.00044	60061.06166	1687.0	0.00034
58575.51230	6.5	0.00024	58617.06071	53.5	0.00038	59341.05470	872.5	0.00045	60061.50254	1687.5	0.00033
58575.95563	7.0	0.00039	58617.50064	54.0	0.00022	59341.49356	873.0	0.00046	60061.94381	1688.0	0.00033
58576.39925	7.5	0.00036	58617.94355	54.5	0.00017	59341.93654	873.5	0.00055	60063.71521	1690.0	0.00034
58576.83874	8.0	0.00042	58618.38582	55.0	0.00040	59342.37567	874.0	0.00067	60064.15847	1690.5	0.00037
58577.28074	8.5	0.00012	58618.83083	55.5	0.00044	59342.82239	874.5	0.00041	60064.59739	1691.0	0.00030
58577.72402	9.0	0.00037	58619.27046	56.0	0.00021	59343.26177	875.0	0.00053	60065.04066	1691.5	0.00030
58578.16485	9.5	0.00026	58619.71444	56.5	0.00034	59343.70379	875.5	0.00071	60065.48196	1692.0	0.00029
58578.60739	10.0	0.00046	58620.15474	57.0	0.00056	59344.14506	876.0	0.00042	60065.92317	1692.5	0.00027
58579.04978	10.5	0.00045	58620.59589	57.5	0.00040	59344.59012	876.5	0.00054	60066.36728	1693.0	0.00030
58579.49038	11.0	0.00030	58621.03823	58.0	0.00018	59345.03023	877.0	0.00045	60066.80792	1693.5	0.00038
58579.93289	11.5	0.00048	58621.48190	58.5	0.00024	59345.47615	877.5	0.00066	60067.24872	1694.0	0.00028
58580.37447	12.0	0.00036	58621.92189	59.0	0.00022	59345.91006	878.0	0.00076	60067.69553	1694.5	0.00024
58580.82057	12.5	0.00034	58622.36610	59.5	0.00048	59347.68278	880.0	0.00051	60069.01844	1696.0	0.00058
58581.25860	13.0	0.00033	58622.80536	60.0	0.00021	59348.12482	880.5	0.00066	60069.46017	1696.5	0.00046
58581.70065	13.5	0.00011	58623.25098	60.5	0.00022	59348.56668	881.0	0.00067	60069.89970	1697.0	0.00037
58583.02629	15.0	0.00032	58623.68970	61.0	0.00019	59349.00738	881.5	0.00062	60070.34433	1697.5	0.00050
58583.46947	15.5	0.00064	59307.45870	834.5	0.00048	59349.44945	882.0	0.00046	60070.78644	1698.0	0.00052
58583.90988	16.0	0.00024	59307.90346	835.0	0.00030	59349.89660	882.5	0.00049	60071.23112	1698.5	0.00037
58584.35359	16.5	0.00033	59308.34274	835.5	0.00033	59350.33224	883.0	0.00062	60071.67084	1699.0	0.00061
58584.79381	17.0	0.00033	59308.78486	836.0	0.00031	59350.77254	883.5	0.00048	60072.10753	1699.5	0.00066
58585.23743	17.5	0.00030	59309.22788	836.5	0.00047	59351.21601	884.0	0.00048	60072.55328	1700.0	0.00048
58585.68021	18.0	0.00032	59309.66930	837.0	0.00037	59351.66064	884.5	0.00057	60072.99538	1700.5	0.00052
58586.12364	18.5	0.00031	59310.11184	837.5	0.00023	59352.09770	885.0	0.00052	60073.44014	1701.0	0.00043
58586.56482	19.0	0.00039	59310.55204	838.0	0.00030	59352.54232	885.5	0.00055	60073.88186	1701.5	0.00064
58587.00787	19.5	0.00027	59310.99457	838.5	0.00035	59352.98380	886.0	0.00055	60074.32231	1702.0	0.00066
58587.44784	20.0	0.00022	59311.43751	839.0	0.00025	59353.42594	886.5	0.00042	60074.76122	1702.5	0.00050
58587.89134	20.5	0.00022	59311.87970	839.5	0.00039	59353.87131	887.0	0.00059	60075.20774	1703.0	0.00046
58588.33155	21.0	0.00015	59312.32043	840.0	0.00022	59354.31209	887.5	0.00053	60075.65137	1703.5	0.00068
58588.77622	21.5	0.00014	59312.76598	840.5	0.00031	59354.75179	888.0	0.00047	60076.53155	1704.5	0.00061
58589.21430	22.0	0.00139	59313.20262	841.0	0.00037	59355.19564	888.5	0.00047	60076.97495	1705.0	0.00061
58589.65949	22.5	0.00025	59313.65069	841.5	0.00024	59355.63353	889.0	0.00043	60077.41750	1705.5	0.00052
58590.09857	23.0	0.00030	59314.08602	842.0	0.00032	59356.07916	889.5	0.00050	60077.86026	1706.0	0.00052
58590.54181	23.5	0.00017	59314.53014	842.5	0.00041	59356.51878	890.0	0.00062	60078.29890	1706.5	0.00051
58590.98400	24.0	0.00035	59314.97102	843.0	0.00031	59356.96604	890.5	0.00082	60078.74227	1707.0	0.00048
58591.42658	24.5	0.00036	59315.41203	843.5	0.00034	59357.40351	891.0	0.00055	60079.18897	1707.5	0.00049
58591.86852	25.0	0.00022	59315.85605	844.0	0.00026	59357.84515	891.5	0.00039	60079.62981	1708.0	0.00044
58592.31010	25.5	0.00038	59316.30190	844.5	0.00031	59358.28964	892.0	0.00051	60080.06855	1708.5	0.00063
58592.75126	26.0	0.00039	59316.74043	845.0	0.00026	59358.73201	892.5	0.00048	60080.50730	1709.0	0.00053
58593.19595	26.5	0.00026	59317.18404	845.5	0.00038	59359.16913	893.0	0.00052	60080.95305	1709.5	0.00051
58593.63629	27.0	0.00045	59317.62363	846.0	0.00031	59359.61948	893.5	0.00051	60081.39369	1710.0	0.00047
58594.07894	27.5	0.00024	59318.06535	846.5	0.00044	60041.16669	1664.5	0.00030	60081.83729	1710.5	0.00058
58594.52186	28.0	0.00039	59320.27523	849.0	0.00029	60041.61872	1665.0	0.00025	60082.27957	1711.0	0.00046
58597.17258	31.0	0.00026	59320.71976	849.5	0.00023	60042.94206	1666.5	0.00029	60082.72362	1711.5	0.00060
58597.61472	31.5	0.00038	59321.16077	850.0	0.00034	60043.38255	1667.0	0.00034	60083.16379	1712.0	0.00058
58598.05540	32.0	0.00032	59321.60364	850.5	0.00031	60043.82585	1667.5	0.00023	60084.49029	1713.5	0.00049
58598.49952	32.5	0.00033	59322.04407	851.0	0.00035	60044.26715	1668.0	0.00025	60084.93224	1714.0	0.00038
58598.94008	33.0	0.00027	59322.48491	851.5	0.00023	60044.70862	1668.5	0.00028	60085.37741	1714.5	0.00048
58599.38361	33.5	0.00029	59322.92837	852.0	0.00030	60045.14974	1669.0	0.00029	60085.81676	1715.0	0.00037
58599.82437	34.0	0.00023	59323.37305	852.5	0.00034	60045.59309	1669.5	0.00039	60086.25885	1715.5	0.00039
58600.26685	34.5	0.00036	59323.81164	853.0	0.00028	60046.03571	1670.0	0.00035	60086.69829	1716.0	0.00044
58600.70610	35.0	0.00037	59324.25592	853.5	0.00025	60046.47768	1670.5	0.00026	60087.14042	1716.5	0.00049
58601.15038	35.5	0.00036	59324.69728	854.0	0.00028	60046.91919	1671.0	0.00020	60087.58317	1717.0	0.00044
58601.59086	36.0	0.00032	59325.13993	854.5	0.00043	60047.36298	1671.5	0.00025	60088.02407	1717.5	0.00049
58602.03462	36.5	0.00023	59325.58062	855.0	0.00024	60047.80250	1672.0	0.00026	60088.46892	1718.0	0.00046
58602.47502	37.0	0.00022	59326.02314	855.5	0.00047	60048.68766	1673.0	0.00028	60088.90923	1718.5	0.00048
58602.91879	37.5	0.00026	59326.46614	856.0	0.00023	60049.12895	1673.5	0.00026	60089.35204	1719.0	0.00038

Table A.6. Eclipse times for TIC 323486857 (continued)

BJD −2 400 000	Cycle no.	std. dev. (<i>d</i>)	BJD −2 400 000	Cycle no.	std. dev. (<i>d</i>)	BJD −2 400 000	Cycle no.	std. dev. (<i>d</i>)	BJD −2 400 000	Cycle no.	std. dev. (<i>d</i>)
58603.35927	38.0	0.00027	59326.90804	856.5	0.00025	60049.57184	1674.0	0.00029	60089.79635	1719.5	0.00086
58603.80102	38.5	0.00023	59327.34780	857.0	0.00034	60050.01534	1674.5	0.00022	60090.23819	1720.0	0.00098
58604.24427	39.0	0.00032	59327.78911	857.5	0.00036	60050.45400	1675.0	0.00024	60090.67897	1720.5	0.00063
58604.68696	39.5	0.00034	59328.23375	858.0	0.00034	60050.90010	1675.5	0.00029	60091.11812	1721.0	0.00049
58605.12795	40.0	0.00024	59328.67518	858.5	0.00027	60051.33576	1676.0	0.00024	60091.55560	1721.5	0.00064
58605.56796	40.5	0.00028	59329.11724	859.0	0.00033	60051.78066	1676.5	0.00030	60091.99793	1722.0	0.00051
58606.01130	41.0	0.00028	59329.56032	859.5	0.00033	60052.22169	1677.0	0.00027	60092.44365	1722.5	0.00061
58606.45355	41.5	0.00027	59330.00054	860.0	0.00031	60052.66168	1677.5	0.00026	60092.88863	1723.0	0.00042
58606.89314	42.0	0.00024	59330.44647	860.5	0.00034	60053.10468	1678.0	0.00031	60093.32787	1723.5	0.00063
58607.33810	42.5	0.00029	59330.88656	861.0	0.00025	60053.54895	1678.5	0.00027	60093.76998	1724.0	0.00052
58607.77827	43.0	0.00036	59331.32648	861.5	0.00029	60053.99122	1679.0	0.00027	60094.21013	1724.5	0.00050
58608.22090	43.5	0.00030	59331.76958	862.0	0.00041	60054.43533	1679.5	0.00034	60094.65193	1725.0	0.00058
58608.66302	44.0	0.00039	59332.21264	862.5	0.00028	60054.87346	1680.0	0.00025	60095.09516	1725.5	0.00055
58609.10723	44.5	0.00030	59333.98326	864.5	0.00090	60055.30942	1680.5	0.00058	60095.53596	1726.0	0.00048
58609.54582	45.0	0.00071	59334.42102	865.0	0.00033	60055.75857	1681.0	0.00031	60095.98375	1726.5	0.00049
58610.88147	46.5	0.00087	59334.86242	865.5	0.00040	60056.20025	1681.5	0.00027	60096.42393	1727.0	0.00070

Table A.7. Eclipse times for TIC 650024463

BJD −2 400 000	Cycle no.	std. dev. (<i>d</i>)	BJD −2 400 000	Cycle no.	std. dev. (<i>d</i>)	BJD −2 400 000	Cycle no.	std. dev. (<i>d</i>)	BJD −2 400 000	Cycle no.	std. dev. (<i>d</i>)
58327.08816	−0.5	0.00110	58654.64552	45.0	0.00049	59079.24315	104.0	0.00037	60122.70738	249.0	0.00042
58330.79614	0.0	0.00050	58658.16613	45.5	0.00115	59082.83269	104.5	0.00108	60129.91097	250.0	0.00033
58334.27812	0.5	0.00069	58661.83767	46.0	0.00048	59086.43768	105.0	0.00050	60133.57915	250.5	0.00093
58337.98821	1.0	0.00030	58669.02564	47.0	0.00051	59367.04776	144.0	0.00040	60137.11216	251.0	0.00043
58341.46618	1.5	0.00114	58672.54609	47.5	0.00100	59370.68081	144.5	0.00100	60140.77733	251.5	0.00086
58345.17921	2.0	0.00042	58676.22071	48.0	0.00053	59374.25614	145.0	0.00042	60144.31914	252.0	0.00029
58348.65041	2.5	0.01546	58679.73200	48.5	0.00111	59377.89761	145.5	0.00084	60147.98837	252.5	0.00108
58352.36818	3.0	0.00053	59043.21409	99.0	0.00048	59381.45739	146.0	0.00036	60155.19765	253.5	0.00099
58625.84233	41.0	0.00112	59046.80730	99.5	0.00102	59385.08446	146.5	0.00079	60158.74801	254.0	0.00030
58629.36316	41.5	0.00144	59050.42746	100.0	0.00036	59388.67342	147.0	0.00037	60162.39658	254.5	0.00094
58633.05334	42.0	0.00067	59054.01795	100.5	0.00108	60101.12259	246.0	0.00029	60165.94101	255.0	0.00044
58636.57755	42.5	0.00082	59057.63048	101.0	0.00045	60104.77423	246.5	0.00074	60169.58876	255.5	0.00076
58643.78601	43.5	0.00103	59064.84274	102.0	0.00041	60108.31387	247.0	0.00037	60173.13221	256.0	0.00033
58647.45317	44.0	0.00055	59068.42848	102.5	0.00101	60111.95859	247.5	0.00251	60176.77814	256.5	0.00111
58650.97684	44.5	0.00119	59075.63588	103.5	0.00079	60115.50744	248.0	0.00028	60180.32145	257.0	0.00053

Appendix B: Radial velocities of TICs 287756035 and 321978218

In this appendix we list the RV data obtained for two tertiary components out of our seven triples (Tables B.1-B.2). All of these data were obtained with the CHIRON spectrometer on the SMARTS telescope.

Table B.1. Measured radial velocities of the tertiary component of TIC 287756035. The date is given as BJD − 2 400 000, while the RVs are in km s^{−1}.

Date	RV _B	Date	RV _B	Date	RV _B
59700.608356	7.628	59738.546993	21.727	60053.676004	3.070
59722.571059	16.556	59793.483242	24.726		

Table B.2. Measured radial velocities of the tertiary component of TIC 321978218. The date is given as BJD − 2 400 000, while the RVs are in km s^{−1}.

Date	RV _B	Date	RV _B	Date	RV _B
59197.534786	−49.069	59378.910596	−20.313	59828.655080	−51.324
59201.567894	−38.221	59383.923361	−3.060	59866.610970	38.891
59189.515319	−21.500	59384.912542	0.014	59872.611652	26.137
59195.592569	−49.890	59397.889185	33.266	59877.609567	−5.269
59371.888074	−45.392	59399.767719	37.061	59881.591328	−36.279
59373.907426	−38.801	59400.828602	38.036		